University of Stavanger

Faculty of Science and Technology

MASTER'S THESIS

Study program/Specialization:	Spring semester, 2017
MSc Petroleum Engineering/Drilling Engineering	**Open**
Writer: **Jan Vidar Eriksen**	…… (Writer's signature)

Faculty supervisor: **Mesfin Balayneh**

Thesis title:

Analysis of the de-rated Burst and Collapse Resistance of a Locally Worn Tubing by using the Finite Element Method and API models

Credits (ECTS): **30**

Key words: Local Wear Tubing Burst Collapse FEM API Models Von Mises	Pages: 153 + enclosure: 2 Stavanger, 15/06-2017 Date/year

This page intentionally left blank.

Master Thesis

Analysis of the de-rated Burst and Collapse Resistance of a Locally Worn Tubing by using the Finite Element Method and API models

Universitetet
i Stavanger

Jan Vidar Eriksen

University of Stavanger

June 15, 2017

This page intentionally left blank.

Abstract

A well integrity survey performed by the Petroleum Safety Authority showed that tubing related problems are a major issue on the Norwegian Continental Shelf [1]. Caliper log runs carried out by ConocoPhillips revealed that the production tubing in a bent section contained local scars with a wall thickness reduction up to 47% [2]. In order to ensure a sufficient well integrity, a accurate prediction of the de-rated tubing strength is important. Today, the most common methods to estimate the de-rated burst and collapse pressures of a damaged tubing are the API models, which assume a uniform wear. In this thesis the Finite Element Method have been applied in order to investigate if the API models also are applicable for a locally worn tubing.

Three different local wear shapes have been simulated, referred to as crescent, wedge and rectangular shaped. The results shows that as the wear depth increases up to 50%, the deviation between the FEM results and the API model for burst reaches up to 71%, 114% and 147%, respectively. The models for collapse showed a similar trend, but with a significantly lower deviation compared to the burst model.

According to the FEM results the API models can not be applied for a tubing with a local wear. The overall results proves the need to perform a FEM based analysis for a locally damaged tubular in order to ensure sufficient well integrity.

This page intentionally left blank.

Acknowledgements

This master thesis was written for the Department of Petroleum Engineering at the University in Stavanger (UiS).

I want to thank everyone that have helped me throughout the process of writing this thesis. Thanks to Theodor Ivesdal for helping me with setting up and installing the software Abaqus, and thanks to Ove Mikkelsen for giving me tips related to the software.

I would also like to thank my supervisor Mesfin Balayneh for presenting this interesting topic and for always being available. His excellent guidance and engagement have been very valuable during the writing process. Thank you very much!

This page intentionally left blank.

Table of Contents

Abstract ii

Acknowledgments iv

List of Figures xii

List of Tables xiv

Abbreviations xvi

Nomenclature xix

1 Introduction 1
- 1.1 Background and Research Motivation . . . 2
  - 1.1.1 Petroleum Safety Authority - Well Integrity Survey . . . 2
  - 1.1.2 ConocoPhillips - Tubing Investigations . . . 3
- 1.2 Problem Formulation . . . 5
- 1.3 Thesis Objective . . . 6

2 Literature Study 7
- 2.1 Prediction of Casing Wear . . . 7
- 2.2 Casing Strength After Wear . . . 9
- 2.3 Wear Depth . . . 11
  - 2.3.1 Wear by Drillpipe Tripping . . . 11
  - 2.3.2 Wear by Wireline . . . 12
- 2.4 Casing and Tubing Failure . . . 14
- 2.5 Corrosion . . . 15
  - 2.5.1 Localized Corrosion . . . 16

3 Theory 18
- 3.1 Thick Walled Cylinder . . . 18
  - 3.1.1 Radial Stress . . . 19
  - 3.1.2 Hoop Stress . . . 20
  - 3.1.3 Axial Stress . . . 20
- 3.2 Thin Walled Cylinder . . . 21
  - 3.2.1 Radial Stress . . . 21
  - 3.2.2 Hoop Stress . . . 22
  - 3.2.3 Axial Stress . . . 22
- 3.3 Bending Stress . . . 22

3.4 Tri-axial well design - Failure Criteria and Design Factor 23
3.5 Failure Criteria 24
3.5.1 Tresca Criterion 24
3.5.2 Von Mises Criterion 24
3.6 Design Factor 25
3.7 Burst theory 27
3.7.1 Burst Models - Thick-Walled Cylinder 28
3.7.2 Burst Models - Thin-Walled Cylinder 29
3.8 API Collapse Models 30
3.9 Fracture Mechanics 33
3.9.1 Energy Balance Approach 33
3.9.2 The Stress Intensity Approach 37

4 Finite Element Method **39**
4.1 Finite Element Method Steps 39
4.1.1 Idealization 39
4.1.2 Discretization 40
4.1.3 Error Sources and Approximation 40
4.1.4 The Finite Element Method 41
4.1.5 Element Nodes, Geometry and Degrees of Freedom 41
4.2 FEM Model Generation 42
4.2.1 Input Data 43
4.2.2 Geometry Building 43
4.2.3 Crescent Shaped Scar 44
4.2.4 Wedge Shaped Scar 44
4.2.5 Rectangular Scar 45
4.2.6 Meshing 46
4.2.7 Boundary Conditions 46
4.2.8 Loading 47
4.3 FEM Simulation Procedure 47

5 Results **49**
5.1 Burst Modeling: Single Scar 49
5.1.1 Uniform Wear Method - Investigation 50
5.1.2 Burst Scenario 52
5.1.3 Reference Model - 0% wear 52
5.1.4 Crescent Shaped Wear 53
5.1.5 Wedge Shaped Wear 58
5.1.6 Rectangular Shaped Wear 63

5.1.7 Comparing Wear Shapes 68
5.2 Collapse Modeling: Single Scar 69
5.2.1 Collapse Scenario 70
5.2.2 Reference Model - 0% wear 70
5.2.3 Crescent Shaped Wear 71
5.2.4 Wedge Shaped Wear 76
5.2.5 Rectangular Shaped Wear 81
5.2.6 Comparing Wear Shapes 86
5.3 Burst Modeling: Two Scars 87
5.3.1 Crescent Shaped Scars 87
5.3.2 Wedge Shaped Scars 91
5.3.3 Mix of Two Scar Shapes 95
5.3.4 Comparing The Two Scars Scenarios 99
5.4 Collapse Modeling: Two Scars 100
5.4.1 Crescent Shaped Scars 100
5.4.2 Wedge Shaped Scars 104
5.4.3 Mix of Two Scar Shapes 108
5.4.4 Comparing The Two-Scars Scenarios 112
5.5 The Effect of Temperature - Burst 113
5.5.1 Theoretical Stresses 114
5.5.2 Simulated Results 116
5.5.3 Reference Model - Pressure and Temperature Loadings 116
5.5.4 Reference Model - Only Pressure Loadings 118
5.5.5 Comparison Of The Loadings 119
5.5.6 Crescent Shaped Wear 120
5.5.7 Wedge Shaped Wear 121
5.5.8 Comparison of The Wear Shapes 122

6 Summary And Discussion **123**
6.1 Burst Analysis 123
6.2 Collapse Analysis 125

7 Conclusion **128**

A Appendix: Effect of Seed Size **131**

B Appendix: Effect Of Wear Width **132**

List of Figures

1 Category barrier element failure 3
2 Pulled tubing with a crescent shaped wear 3
3 Correlation of recorded damage to borehole profile 4
4 Comparison of the API burst strength and worn casing initial yield burst strength 10
5 Wear depth vs wear volume 12
6 Collapsed production- casing and tubing 15
7 Corrosion reactions 16
8 Pitting Corrosion 16
9 Different wear shapes 17
10 Locally corroded L80 13Cr tubing 17
11 Stresses in a thick walled cylinder 18
12 Illustration of the cross secton of a thick walled cylinder 19
13 Stress distribution - thick-walled cylinder 21
14 Three-dimensional design factors projected onto a two-dimensional plane 27
15 Hoop stress and internal pressure balance on a cylinder 28
16 Example of collapse pressure as a function of slenderness - L80 tubing 32
17 Idealization of unloaded region near crack flanks 34
18 Fracture energy balance 35
19 Fracture energy balance 37
20 Stresses near crack tip 37
21 The effect of angle on the different stresses related to fracture 38
22 Physical simulation process 40
23 Typical finite element geometries in 1D, 2D and 3D 41
24 Steps of generating the models in Abaqus 42
25 The geometry of a tubing with an crescent shaped wear 44
26 The geometry of a tubing with an wedge shaped wear 45
27 The geometry of a tubing with an rectangular shaped wear 45
28 Meshed model of a unworn tubing 46
29 Von Mises stress for a uniform wear and different local wears under a internal pressure of 3500 psi 50
30 Uniform Wear (left) vs Local Wedge Shaped Wear (right) 51
31 Unworn reference model with internal pressure of 9700 psi 52
32 Simulated model with 25% wear and a internal pressure of 4800 psi 53

33 Simulated model with 47% wear and a internal pressure of 3000 psi . 54
34 Internal pressure and the respective Von Mises Stress for different wear depths 55
35 Safe and failure zone for operating internal pressure 56
36 Barlow's model compared with the models based on simulation 57
37 Simulated model with 25% wear and a internal pressure of 4400 psi 58
38 Simulated model with 47% wear and a internal pressure of 2400 psi 59
39 Internal pressure and the respective Von Mises Stress for different wear depths 60
40 Safe and failure zone for operating internal pressure 61
41 Barlow's model compared with the models based on simulation . . . 62
42 Simulated model with 25% wear and a internal pressure of 3600 psi 63
43 Simulated model with 47% wear and a internal pressure of 2300 psi . 64
44 Internal pressure and the respective Von Mises Stress for different wear depths 65
45 Safe and failure zone for operating internal pressure 66
46 Barlow's model compared with the models based on simulation 67
47 Comparison of burst pressure limit for the different wear shapes . . 68
48 Simulated unworn reference model with a external pressure of 9000 psi 70
49 Simulated model with 25% wear depth and a external pressure of 4400 psi 71
50 Simulated model with 47% wear depth and a external pressure of 2800 psi 72
51 External pressure and the respective Von Mises Stress for different wear depths 73
52 Safe and failure zone for operating external pressure 74
53 Simulated based models compared with the theoretical collapse models for uniform thickness 75
54 Simulated model with 25% wear depth and a external pressure of 4000 psi 76
55 Simulated model with 47% wear depth and a external pressure of 2100 psi 77
56 External pressure and the respective Von Mises Stress for different wear depths 78
57 Safe and failure zone for operating external pressure 79

58 Simulated based models compared with the theoretical collapse models for uniform thickness 80
59 Simulated model with 25% wear depth and a external pressure of 3300 psi 81
60 Simulated model with 47% wear depth and a external pressure of 2100 psi 82
61 External pressure and the respective Von Mises Stress for different wear depths 83
62 Safe and failure zone for operating external pressure 84
63 Simulated based models compared with the theoretical collapse models for a uniform thickness 85
64 Comparison of collapse resistance limit for the different wear shapes 86
65 Simulated model with 25% wear and a internal pressure of 4600 psi 88
66 Simulated model with 47% wear and a internal pressure of 2700 psi 88
67 Internal pressure and the respective Von Mises Stress for different wear depths 89
68 Safe and failure zone for operating internal pressure 90
69 Simulated model with 25% two wear scars and a internal pressure of 4300 psi 91
70 Simulated model with 47% wear scars and a internal pressure of 2300 psi 92
71 Internal pressure and the respective Von Mises Stress for different wear depths 93
72 Safe and failure zone for operating internal pressure 94
73 Simulated model with 25% wear scars and a internal pressure of 4200 psi 95
74 Simulated model with 47% wear scars and a internal pressure of 2200 psi 96
75 Internal pressure and the respective Von Mises Stress for different wear depths 97
76 Safe and failure zone for operating internal pressure 98
77 Comparison of the different two-scars scenarios 99
78 Simulated model with two 25% wear scars and a external pressure of 4200 psi 100
79 Simulated model with two 47% wear scars and a external pressure of 2500 psi 101

80 External pressure and the respective Von Mises Stress for different wear depths 102
81 Safe and failure zone for operating external pressure 103
82 Simulated model with two 25% wear scars and a external pressure of 4000 psi 104
83 Simulated model with two 47% wear scars and a external pressure of 2000 psi 105
84 External pressure and the respective Von Mises Stress for different wear depths 106
85 Safe and failure zone for operating external pressure 107
86 Simulated model with two 25% wear scars and a external pressure of 3800 psi 108
87 Simulated model with two 47% wear scars and a external pressure of 1900 psi 109
88 Safe and failure zone for operating external pressure 110
89 Safe and failure zone for operating external pressure 111
90 Comparison of the generated models of the different two-scar scenarios 112
91 Temperature profiles in a well as a function of time 113
92 Stresses in a unworn thick-walled cylinder due to pressures 114
93 Stresses in a unworn thick-walled cylinder due to temperature changes 114
94 Von Mises Stress in a unworn thick-walled cylinder due to temperature and pressure - Burst 115
95 Reference model with a internal pressure of 6200 psi. ΔT is equal to 243°F 116
96 Simulated Von Mises stress across the wall of the tubing (plot from Abaqus) 117
97 Reference model with a internal pressure of 9800 psi. ΔT is set to 0 . 118
98 Simulated Von Mises stress across the wall of the tubing (plot from Abaqus) 119
99 Burst pressure as a function of wear depths 120
100 Burst pressure for different wear depths for the various loadings 121
101 Simulation based model for burst pressure for different wear depths under temperature and pressure loadings - Safety factor not included 122
102 Percent Deviation between Barlow's model and the simulation based models for the different single wear shapes 124

103 Percent Deviation between Barlow's model and the simulation based models for two scars 124
104 Percent Deviation between the Barlow's equation and the simulation based models when the effect of temperature is included 125
105 Percent Deviation between the theoretical collapse equations and the simulation based models for single scars 126
106 Percent Deviation between the theoretical collapse equations and the simulation based models for two scars 126
A.1 Comparison of the rectangular wear shape for different seeds 131
B.1 Different Local Wear Width 132

List of Tables

1 Survey Candidates 2
2 Wear Coefficients (C_{wt}) - Drill pipe Tripping Wear Tests 11
3 Wear Coefficients (C_{wt}) - Wireline Wear Tests 13
4 Collapse modes 31
5 Transitional collapse factors 31
6 Plastic collapse factors 32
7 Well Data 43
8 Coiled Tubing Specifications 43
9 Tubing Specifications and Material Properties 43
10 Wear positions details - Coiled Tubing 48
11 Burst Scenario Data 49
12 Internal Pressure and Von Mises Stress for model with 0% wear 53
13 Internal Pressure and Von Mises Stress for model with 25% wear 54
14 Internal Pressure and Von Mises Stress for model with 47% wear 54
15 Result from linear interpolation for burst 55
16 Data from the curves in figure 36 57
17 Internal Pressure and Von Mises Stress for model with 25% wear . . . 58
18 Internal Pressure and Von Mises Stress for model with 47% wear . . . 59
19 Result from linear interpolation for burst 60
20 Data from the curves in figure 41 62
21 Internal Pressure and Von Mises Stress for model with 25% wear . . . 63
22 Internal Pressure and Von Mises Stress for model with 47% wear 64
23 Result from linear interpolation for burst 65
24 Data from the curves in figure 44 67
25 Collapse Scenario Data 69
26 Simulated Collapse Pressures and Von Mises Stress for the unworn Reference Model 70
27 External Pressure and Von Mises Stress for model with 25% wear . . . 71
28 External Pressure and Von Mises Stress for model with 47% wear . . 72
29 Result from linear interpolation for collapse 73
30 Data from figure 53 75

31 External Pressure and Von Mises Stress for model with 25% wear . . 76
32 External Pressure and Von Mises Stress for model with 47% wear . . . 77
33 Result from linear interpolation for collapse 78
34 Data from figure 58 80
35 External Pressure and Von Mises Stress for model with 25% wear . . . 81
36 External Pressure and Von Mises Stress for model with 47% wear . . 82
37 Result from linear interpolation for collapse 83
38 Data from figure 63 85
39 Internal Pressure and Von Mises Stress for model with 25% wear 87
40 Internal Pressure and Von Mises Stress for model with 47% wear . . . 89
41 Result from linear interpolation for burst 90
42 Internal Pressure and Von Mises Stress for model with 25% wear 91
43 Internal Pressure and Von Mises Stress for model with 47% wear . . . 92
44 Result from linear interpolation for burst 94
45 Internal Pressure and Von Mises Stress for model with 25% wear . . . 95
46 Internal Pressure and Von Mises Stress for model with 47% wear . . . 96
47 Result from linear interpolation for burst 97
48 External Pressure and Von Mises Stress for model with 25% wear . . 100
49 External Pressure and Von Mises Stress for model with 47% wear . . . 101
50 Result from linear interpolation for burst 102
51 External Pressure and Von Mises Stress for model with 25% wear . . . 104
52 External Pressure and Von Mises Stress for model with 47% wear . . 105
53 Result from linear interpolation for burst 106
54 External Pressure and Von Mises Stress for model with 25% wear . . 108
55 External Pressure and Von Mises Stress for model with 47% wear . . 109
56 Result from linear interpolation for burst 110
57 Input used in the mathematical equations 115
58 Internal Pressure and Von Mises Stress for model with 0% wear 116
59 Internal Pressure and Von Mises Stress for model with 0% wear 118

Abbreviations

API	American Petroleum Institute
FEM	Finite Element Method
MD	Measured Depth
NCS	Norwegian Continental Shelf
PSA	Petroleum Safety Authority
TVD	True Vertical Depth

Nomenclature

α	Coefficient of thermal expansion
α_{ds}	Drill string curvature
β	Geometry factor
β_a	Height of crack
ϵ	Epsilon
ν	Poisson's ratio
$\sigma_\theta(\Delta T)$	Hoop stress due to temperature
σ_θ	Hoop stres (tangential stress)
$\sigma_a(\Delta T)$	Axial stress due to temperature
σ_a	Axial stress
σ_b	Bending stress
σ_r	Radial stress
$\sigma_r(\Delta T)$	Radial stress due to temperature
σ_y	Yield stress
σ_{ds}	Drill string tension
σ_h	Hoop stress
σ_{max}	Maximum principle stress
σ_{min}	Minimum principle stress

σ_{VME}	Von Mises stress
a	Crack length
a	inner radius
a_c	Critical crack length
b	Outer radius
C_{wt}	Tripping wear coefficient
C_{ww}	Wireline wear coefficient
D	Tool diameter
D_δ	Depth of wear point
d_o	Outer diameter
D_t	Total depth of well at time of interest
DF	Design factor
E	Youngs modulus
E_e	Wear efficiency
E_f	Fraction of drill pipe per joint that contacts wear point
F	Side force
G_c	Critical strain energy
H	Brinell hardness
K_f	Sliding friction factor

K_I	Stress intensity factor
L	Distance slip
N_t	Numbers of round trips per day
N_w	Number of wireline runs
P_a	Internal pressure
P_b	External pressure
P_e	Elastic collapse pressure
P_p	Plastic collapse pressure
P_t	Transitional collapse pressure
P_y	Yield collapse pressure
r	Any distance between a and b radius
r_i	Inner radius
r_o	Outer radius
S	Surface energy
T	Buoyed weight of drill string below wear point
t	Wall thickness
T_s	Max wireline tension on surface
U	Energy absorbed in wear
U^*	Strain energy per volume of stressed material

U_T	Total mechanical energy input
V	Volume of metal removed by wear
V_t	Volume worn by tripping
x, y, z	Dimensionless parameter
Y_p	Minimum yield strength

1 Introduction

The oil industry on the Norwegian Continental Shelf (NCS) has in the later years increased the focus on costs extensively. A significant volatility in the oil price and the demand for oil and gas, combined with a uncertain future oil price, have resulted in a challenging market. The cost level for existing wells and new fields is of crucial significance for the Norwegian Continental Shelf's ability to still be competitive in the oil and gas market. A study performed by the Petroleum Safety Authority in 2006 reported that barrier integrity problems associated with the production and injection tubing are issues of importance on the NCS [1]. Further investigations carried out by ConocoPhillips also revealed that the production tubing in some of their wells contained wears, which results in a reduced material strength. These observations are very important since insufficient well integrity may cause dangerous situations for personnel, equipment and environment, and thus, result in major expenses for the operators.

The NORSOK D-010 standard defines well integrity based on three solutions with the objective of reducing the risk of uncontrolled release of formation fluid during the life time of a well. The standard requires that there shall always be two barriers between a hydrocarbon zone and the surface to avoid accidents [3]. In a typical production well, the production tubing acts as a primary barrier element. During a well's lifetime, the tubing is exposed various loads such as high pressures, temperatures, chemicals, and mechanical loadings during intervention and production. Previous studies of casings and tubings gathered from real wells have shown that intervention and corrosion may cause local wears. This reduces the tubings ability to withstand the different loadings, and thus increase the risk of dangerous situations and extra costs. In this thesis a locally worn tubing under different loading scenarios will be simulated by the use of the Finite Element Method (FEM). This can give us a better understanding of how local wears affects the integrity of the tubing, and by implementing this knowledge help us to maintain sufficient well integrity during the well productivity period.

1.1 Background and Research Motivation

In the following sections the background and research motivation for writing this thesis is presented.

1.1.1 Petroleum Safety Authority - Well Integrity Survey

In the recent years, a number of wells with the potential of causing serious situations have been reported to the Petroleum Safety Authority (PSA). The reasons for this were typically high age, weakness in well design or unclear barrier understandment. As a consequence of these reports, the PSA performed in 2006 a well integrity survey based on audits and inputs from several operating companies. From a total of 2,682 developed wells on the NCS, 12 pre-selected offshore facilities (platform and sub-sea) and 406 production and injection wells were assessed in the project. The main scope of the survey was to identify how extensive the well integrity problems on the NCS are, and find the most common issues and challenges related to the subject [4]. The companies and facilities that took part in the survey is listed in table 1 below.

Table 1: Survey Candidates [1]

BP	Vallhall DP
ConocoPhillips	Ekofisk X and Eldfisk A
ExxonMobil	Jotun B
Hydro	Grane, Njord and Oseberg Øst
Shell	Draugen
Statoil	Statfjord C w/satellites (North and East), Veslefrikk and Åsgard
Talisman	Gyda

The results from the survey showed that 75 out of the 406 wells assessed (18%) had integrity problems, where 41 of the wells were producers and 34 of the wells were injectors. The majority of integrity problems, approximately 39%, were found within the tubing barrier. Figure 1 shows the number of wells with the respective well integrity problem.

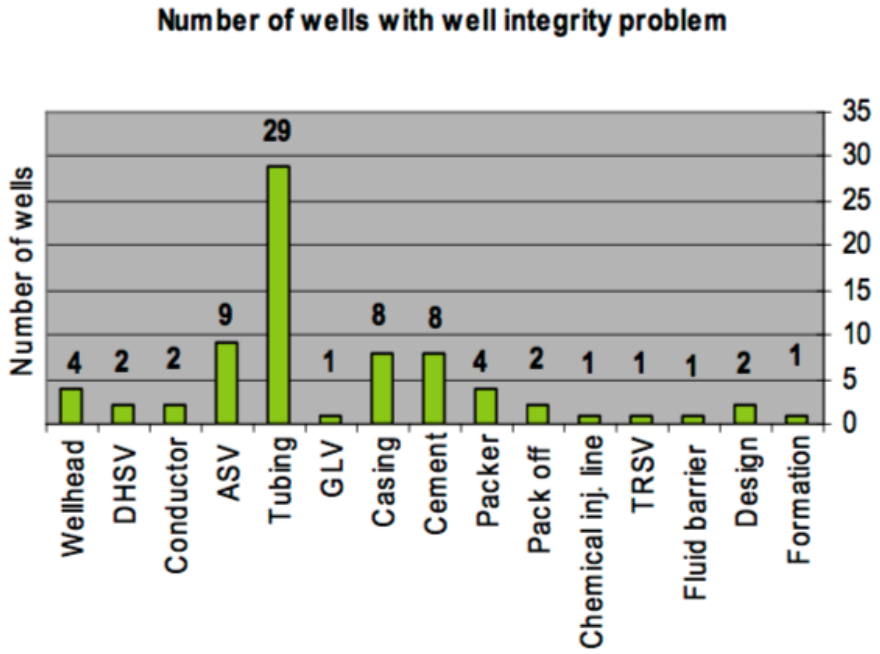

Figure 1: Category barrier element failure [4]

1.1.2 ConocoPhillips - Tubing Investigations

Previously examinations of a pulled tubing from a offshore well operated by ConocoPhillips revealed that the tubing in the well actually contained wears. The pulled tubing showed a crescent shaped wear that most likely was caused by multiple runs of coiled tubing that were performed during intervention [2]. Figure 2 shows the tubing and the groove wear caused by the intervention runs.

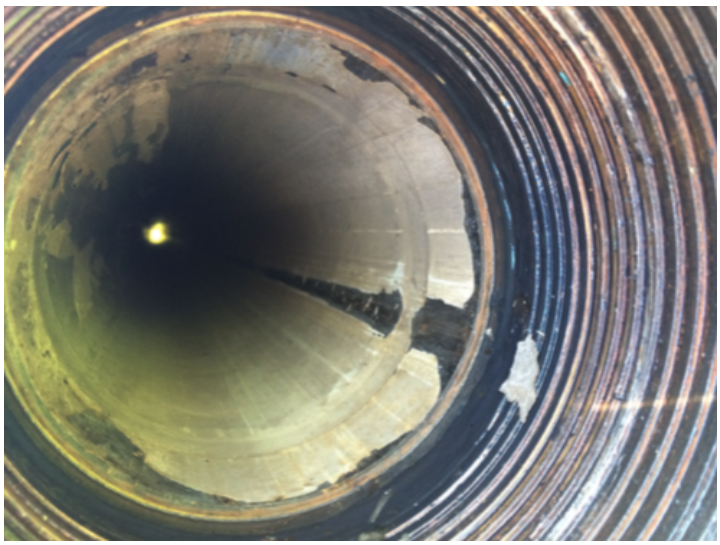

Figure 2: Pulled tubing with a crescent shaped wear [2]

ConocoPhillips also performed a investigation of an operative production well located at the Ekofisk Field in the southern part of the Norwegian Sea. Data from this well will later be presented and used during the simulations. The well has a maximum dogleg severity of 4 degrees per 100 ft at a depth of 2588 ft. measured depth. In the period from 2009-2010 a total of 16 runs of coiled tubing were performed inside the production tubing, where the majority of the runs were related to acid stimulation [2]. The target of the investigation was to determine the condition of the production tubing. This was done by using a multi-fingered caliper tool. The caliper tool measures the internal diameter of the tubing with the purpose of determine the condition of the tubing with respect to corrosion, erosion and mechanical damage. The tool identified multiple wears, where the majority were local wears with various pattern and depths. The most critical observation was a reduction of 47% of the wall thickness at a depth of 1626. ft [2]. Figure 3 shows the data from the caliper tool. The log indicates that the deviated part of the well is the most critical with respect to mechanical damage.

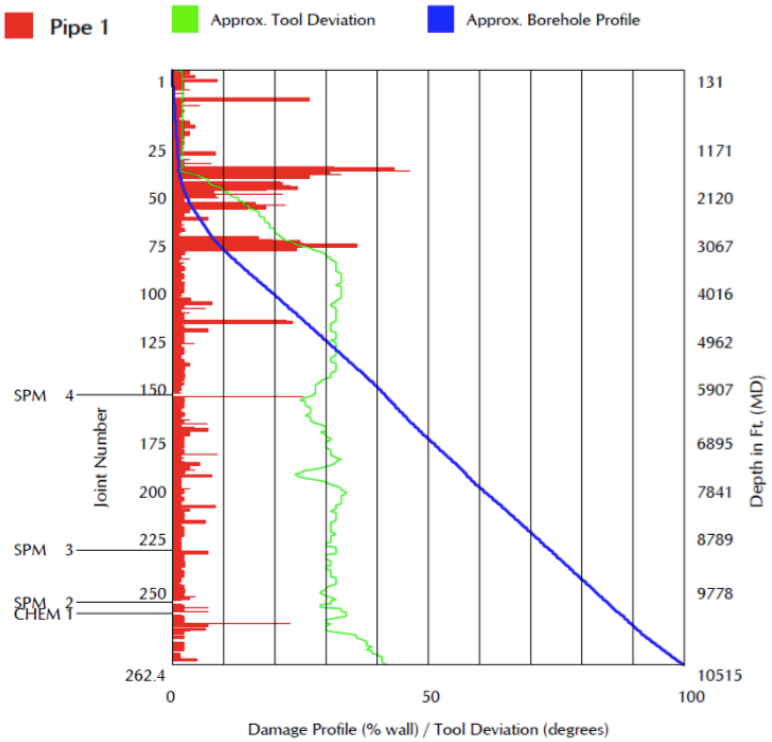

Figure 3: Correlation of recorded damage to borehole profile [2]

Therefore, based on the above observations, the simulations in this thesis considers a wall thickness reduction up to 50%.

1.2 Problem Formulation

This thesis will investigate how different shapes of local wears affects the tubings ability to maintain sufficient well integrity. Three different local wear shapes were simulated, referred to as crescent, wedge and rectangular shaped. There are several reasons for local wear to appear within the tubing, the main reasons in a offshore well are due to corrosion and mechanical damage. The most common form of corrosion in the oil and gas industry is pitting (local corrosion), which can create numerous of different local wear shapes in the material. Mechanical damage may be caused by intervention work such as wire-line or coiled tubing. As previously mentioned, a well is subjected to different loadings during it's lifetime. By simulating different scenarios with high differential pressures and temperatures the effect of various wear shapes will be studied. This is a area of importance since local wear of the tubing can decrease the burst and collapse resistance dramatically, and thus cause well integrity issues. The investigations performed by ConocoPhillips showed that the majority of the wears detected were local wears. This means that the reduction in the wall thickness around the circumference of the tubing is not uniform. However, when companies estimates the burst and collapse pressures for a worn casing or tubing they often use the API models, which assumes a uniform wear [5]. Thus, the applicability of the current API models for different local wear scars will also be investigated.

By the use of Finite Element Method the locally worn tubing is simulated. The results are then used to generate a model that estimates the de-rated burst and collapse pressure of the tubing. All simulated results presented in this thesis are based on real data gathered from the well operated by ConocoPhillips at the Ekofisk Field, and are therefore only valid under these specific conditions. The different simulated scenarios which are later presented are also inspired by this specific well.

This thesis addresses issues such as:

1. How does the shape of a local wear affect the burst and collapse strength of a tubing when compared to a uniform wear?

2. Which of the three local wear shapes are the most critical with respect to the burst and collapse strength reduction?

3. Investigate the applicability and limitations of the currently used API models for burst and collapse for a locally worn tubing.

4. How does a high differential temperature combined with high pressure affect the burst strength of a locally worn tubing?

1.3 Thesis Objective

The objective is to analyze how tubing wear caused by intervention, corrosion or erosion affects the material strength in regards to burst and collapse. The simulations performed in this thesis does not take into account the effect of bending. To answer the questions addressed earlier, the activities to be included in this thesis are:

1. Literature study of wear.

2. Review stress theory and different burst and collapse models.

3. Perform a numerical simulations by the use of Finite Element Method for different wear shapes and wear depth ranging from 0% to 50% under loadings such as high internal or external pressure and temperatures.

4. Generate new models for burst and collapse based on the simulated results and compare them to the frequently used API models.

2 Literature Study

Today API's Barlow's or Lame's thick walled cylinder equations are the most common method to calculate the burst pressure for cylindrical pipes. However, these equations are assuming a uniform wear, thus, they can not be used when a pipe is locally damaged. The Barlow's equation is derived based on a uniform wall reduction and the burst strength decreases linearly as the wall thickness reduces. The equation does no take into consideration that only a portion of the wall thickness has reduced. In addition, the Barlow's equation does not include the fact that the tangential stress (hoop stress) at locally worn point at the wall increases due to balance with the internal pressure that acts on the inner surface of the tubing. This is important since this increased hoop stress cause the tubing to change shape from circular to oval. Neither does the equation consider the ballooning or bending effects caused by the local damage [7].

To maintain the integrity of the well it is important to investigate how different local wear shapes affects the tubings capacity of withstand loadings. Since corrosion is a common problem within production and injection wells there is a possibility that various types of wear shapes appears. In the following section different studies and reviews performed on the subject are presented.

2.1 Prediction of Casing Wear

Previous studies of casing wear states that the rotation of the drill pipe causes the most of the wear. This conclusion was stated by Bradley and Fontenot after they examined casing sample's recovered from a oil field. Holm developed a wear efficiency model from a wear-coefficient concept. A wear efficiency model describes the relation between the energy dissipated in the wear process and the amount of the metal removed by wear. Holm stated that the product of side force and distance slid is proportional to the volume worn, and that the material hardness (H) is inversely proportional to the worn volume. Dawsen and White later modified the wear-coefficient model by substitute the side-force with friction force. This substitution was meant to give a clearer physical meaning to the force/distance

product in the model. They stated that the distance slid multiplied with the friction force is the mechanical energy dissipated in friction [8].

The wear coefficient is referred to as the wear efficiency (E_e) since it measures the efficiency of the wear process. The following equation 1 give one concept of wear efficiency.

$$E_e = \frac{U}{U_t} \tag{1}$$

Where U = energy absorbed in wear [Joule] and U_t = total mechanical energy input [Joule]

The equation above (eq. 1) can also be expressed in physical properties, the concept is then give as:

$$E_e = \frac{VH}{KFL} \tag{2}$$

Where E_e is the wear efficiency, V is the volume of metal removed by wear, H is the Brinell hardness, K is the sliding friction coefficient, F is the side force and L is the distance slid (representing the numbers of rotations multiplied with the tool joint circumference) [8].

To estimate casing wear down-hole, the linear wear model in combination with the laboratory measured data of wear efficiency can be used. The volume of metal worn is given by:

$$V = \frac{E_e F_f L}{H} \tag{3}$$

Where F_fL is the friction force times the distance slid created by the tool joint surface during rotation (energy dissipated in friction). $\frac{E_e}{H}$ is the proportionality con-

stant (wear efficiency divided by Brinell hardness), which is proportional to the volume of worn metal.

When predicting casing wear in a field, a measured or expected dogleg needs to be included. A simple equation for calculating the side force for a given dogleg is:

$$F = \sigma_d s \sin \alpha_d s \tag{4}$$

Where $\sigma_d s$ is the drill string tension [N] and $\alpha_d s$ is the curvature of the drill string [degrees] [8].

The equation above (4) is simplified as it does not take gravity into account. The drill string curvature is typically associated with a drill string length of 100 ft. This means that the calculated side force (F) in equation 4 gives the total side force for the entire length. In reality the side force is concentrated at a few tool joints, however, this can be ignored for two reasons. The first reason is that wear is a linear function of side force according to the wear-efficiency model. The correlation of the side force makes it possible to exclude questions of pressures and contact areas. The second reason is that there are several tool joints that moves along the casing resulting in a uniform wear within the dogleg section. There can however be variations in the measured wear within the dogleg interval due to presumably differences in the curvature locally. A alternative to equation 4 is the side-force charts in API RP-7G [8].

2.2 Casing Strength After Wear

How to estimate the burst strength reduction caused by a crescent shaped wear has been a important issue in the petroleum industry for years. Earlier studies has investigated the hoop stress and the deformation of a crescent-worn casing, and how this wear reduces the burst strength [9].

For an internal pressurized casing the hoop stress on the remaining wall section

will increase, compared to a unworn casing. This is to balance with the internal pressure that acts on the inner surface, due to the loss of hoop stress on the wall portion that is worn. In addition, in order to maintain a force-moment balance, a bending moment will be induced in the remaining wall of worn casing. This bending moment produces a bending hoop stress, which is a compressive hoop stress at outer diameter and a tensile hoop stress at the inner diameter. When the local bending is considered the maximum hoop stress was found higher for a crescent-worn casing, compared to a unworn casing. The initial yield burst strength for a crescent-worn casing, which is when the maximum hoop stress at the inner radius fiber of the worn portion of the wall reaches the yield strength of the material, was compared to the API burst strength. When including local bending the API burst limit was found to only give a safe prediction on the initial yield burst strength when the casing wear is low [9]. This is illustrated in figure 4.

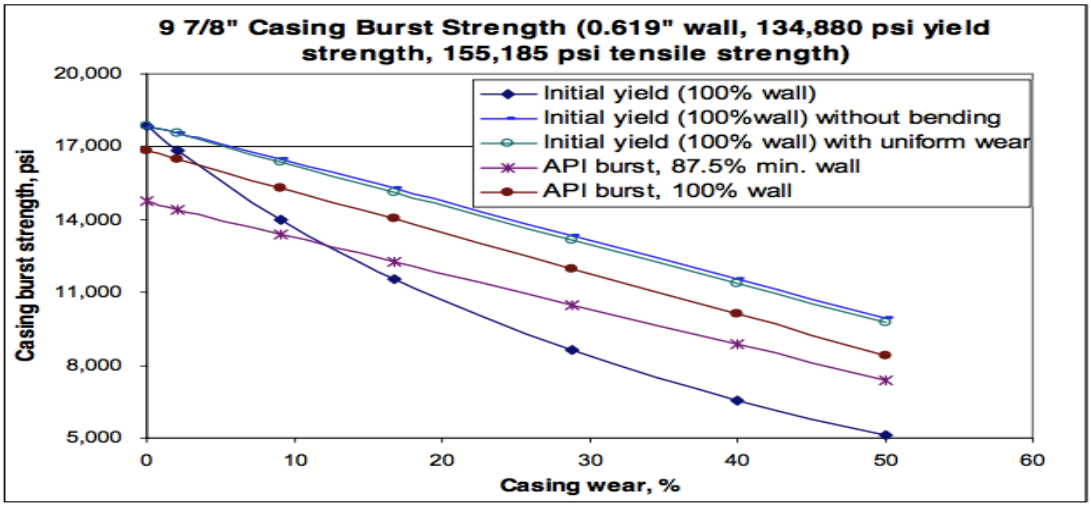

Figure 4: Comparison of the API burst strength and worn casing initial yield burst strength [9]

2.3 Wear Depth

By performing experimental studies, Fontenot and McEver developed several wear coefficients for wire-line and drill pipe tripping. The coefficients were gathered from wear tests and is a function of contact load, casing grade and type of mud. By selecting the appropriate wear coefficient it is possible to estimate the volume of worn metal from the different operations [10].

2.3.1 Wear by Drillpipe Tripping

The amount of casing wear as a results of tripping drill pipe can be estimated if the wear coefficients and hole conditions are known. The wear coefficients are determined based on multiple drill pipe tripping wear tests [10]. The values are given in table 2.

Table 2: Wear Coefficients (C_{wt}) - Drill pipe Tripping Wear Tests [10]

Type of Mud	Contact Load (lb/ft)	Wear Coefficient K-55	(C_{wt} (cu in./lb-ft)) P-110
Water	500	2.9×10^{-8}	2.6×10^{-8}
	1000	8.5×10^{-8}	4.2×10^{-8}
	2000	5.9×10^{-8}	3.7×10^{-8}
Unweighted water-base mud + 3 percent sand	500	7.9×10^{-8}	9.3×10^{-9}
	1000	2.9×10^{-8}	5.7×10^{-9}
	2000	4.4×10^{-8}	5.0×10^{-9}
Weighted water-base mud without drill solids	1000	1.4×10^{-9}	3.6×10^{-9}
	2000	0.7×10^{-9}	1.4×10^{-9}
Weighted water-base mud with 2 to 8 percent drill solids	1000	1.4×10^{-9}	$2.9\ 10^{-9}$
	2000	1.0×10^{-9}	0.7×10^{-9}
Weighted water-base mud with drill solids and 3 percent sand	500	3.6×10^{-9}	
	1000	1.4×10^{-9}	4.3×10^{-8}
	2000	0.7×10^{-9}	0.7×10^{-9}

The wear volume due to drill pipe tripping is calculated by the following equation:

$$V_t = 2C_{wt}TN_tE_f(D_t - D_\delta)\sin\left(\frac{\delta}{2}\right) \tag{5}$$

Where V_t is the volume worn caused by tripping, C_{wt} is the tripping wear coefficient (see table 2), T is the buoyed weight of drill string below wear points, N_t is the numbers of round trips per day, E_f is the fraction of drill pipe per joint that contacts wear point, D_t is the total depth of well at time of interest, D_δ is the depth of wear point and δ is the dog-leg severity. After the volume of wear is calculated the wear depth can be found by the use of figure 5.

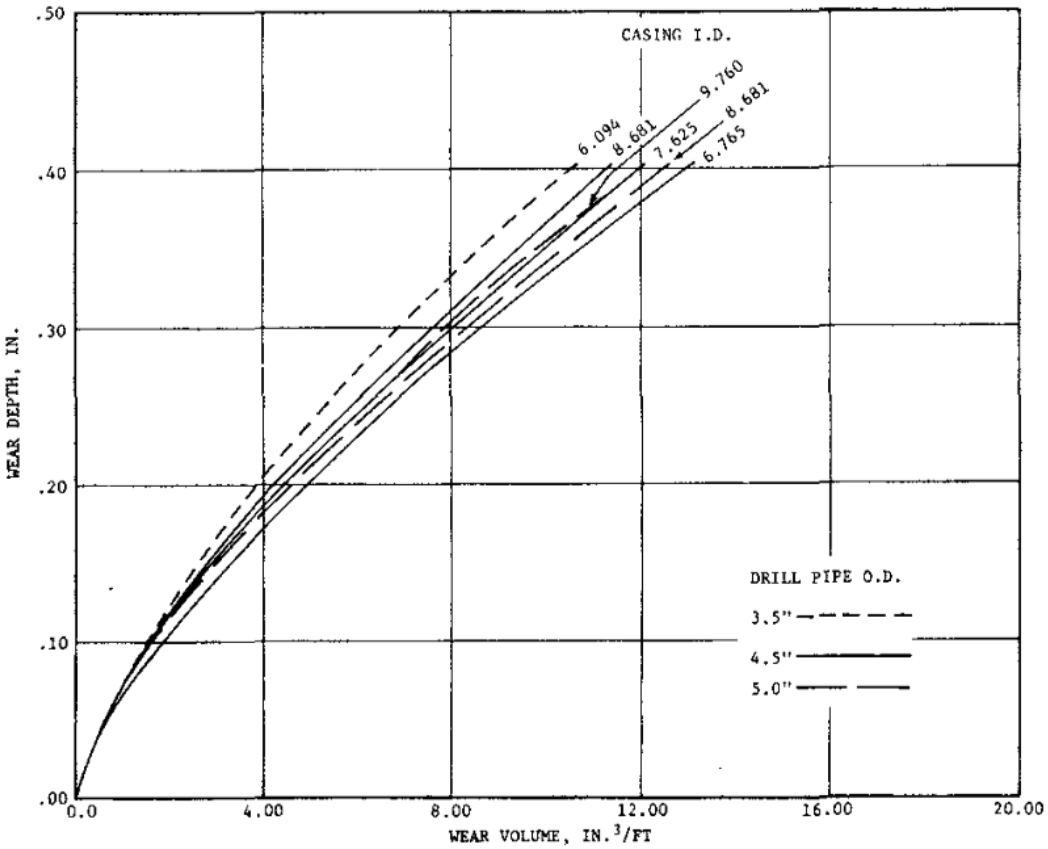

Figure 5: Wear depth vs wear volume [10]

2.3.2 Wear by Wireline

Fontenot and McEver [10] also determined wire-line wear coefficients from the wear tests result. The wear coefficients (C_{ww}) are a function of mud type, contact

load and casing grade and are presented in table 3.

Table 3: Wear Coefficients (C_{wt}) - Wireline Wear Tests [10]

Type of Mud	Contact Load (lb/ft)	Wear Coefficient (C_{ww} (cu in./lb-ft)) K-55	P-110
Water	9.8	1.1 x 10^{-8}	1.2 x 10^{-8}
	19.6	2.0 x 10^{-8}	0.8 x 10^{-8}
Unweighted water-base mud + 3 percent sand	4.9	15 x 10^{-8}	11.0 x 10^{-8}
	9.8	8.6 x 10^{-8}	8.0 x 10^{-8}
	19.6	7.1 x 10^{-8}	7.2 x 10^{-8}
Weighted water-base mud without drill solids	9.8	3.9 x 10^{-8}	3.9 x 10^{-8}
	19.6	1.9 x 10^{-8}	2.2 x 10^{-8}
Weighted water-base mud with 2 to 8 percent drill solids	9.8	5.2 x 10^{-8}	3.5 10^{-8}
	19.6	2.1 x 10^{-8}	2.2 x 10^{-8}
Weighted water-base mud with 8 percent drill solids + 3 percent sand	9.8	12.0 x 10^{-8}	13.0 x 10^{-8}
	19.6	5.2 x 10^{-8}	4.3 x 10^{-8}
Weighted water-base mud without drill solids + 3 percent sand	19.6	6.1 x 10^{-8}	5.9 x 10^{-8}

The wear volume due to wire-line is calculated by the following equation:

The wear volume due to drill pipe tripping is calculated by the following equation:

$$V_w = 2C_{ww}T_sN_w\left(\frac{D_t - D_\delta}{D_t}\right)\sin\left(\frac{\delta}{2}\right) \tag{6}$$

Where $C_w w$ is the wear coefficient, T_s is the maximum wire-line tension at the surface, N_w is the number of wire-line runs, D_t is the total depth of well at time of interest and D_δ is the wear point depth.

Fontenot and McEver used a equation from the "Handbook of Chemistry and Physics" and the calculated volume to determine the wear depth. This equation

was derived from the formula for the area of a circular segment [10]:

$$V_{Wireline}\left(\frac{in^3}{ft}\right) = \frac{\pi D^2}{8} - \left[\left(\frac{D}{2} - D_w\right)\sqrt{D_w(D-D_w)} + \frac{D^4}{4}\sin^{-1}\left(1 - \frac{D_w}{D}\right)\right] \quad (7)$$

Where D is the wire-line or tool diameter and D_w is the depth of wear.

2.4 Casing and Tubing Failure

For the last decades thousands of wells have been drilled and completed in the North Sea, even so, there are still cases where problems occurs. During the installation of a well with a tie back solution a company experienced problems with maintaining the well pressure, indicating a leak in the system. The location of the leak could either be in the PBR, in a casing connection or within the surface equipment. After the surface equipment was carefully checked and eliminated, the well situation was accepted and the well was set on production [11].

At a later stage during production the production casing and tubing collapsed at a depth of approximately 700 m. The casing and tubing were pulled and replaced, and the well was set back on production. The cause of the failure was due to a leakage, resulting in a major pressure built up in the annulus. Additional thermal effects contributed to increase the pressure built up until it exceeded the collapse resistance. Investigations showed that the failed casing actually contained one length of a weaker material, which had a 30% lower collapse rating. No records could explain why this weaker casing length was installed in the string. The consequences were high cost related to the replacement of the production casing and production tubing, cost due to the loss of production, improved test and control procedures [11]. This case shows that tubing and casing integrity is a important area of interest, and thus it has been a great motivation when working with the subject in this thesis.

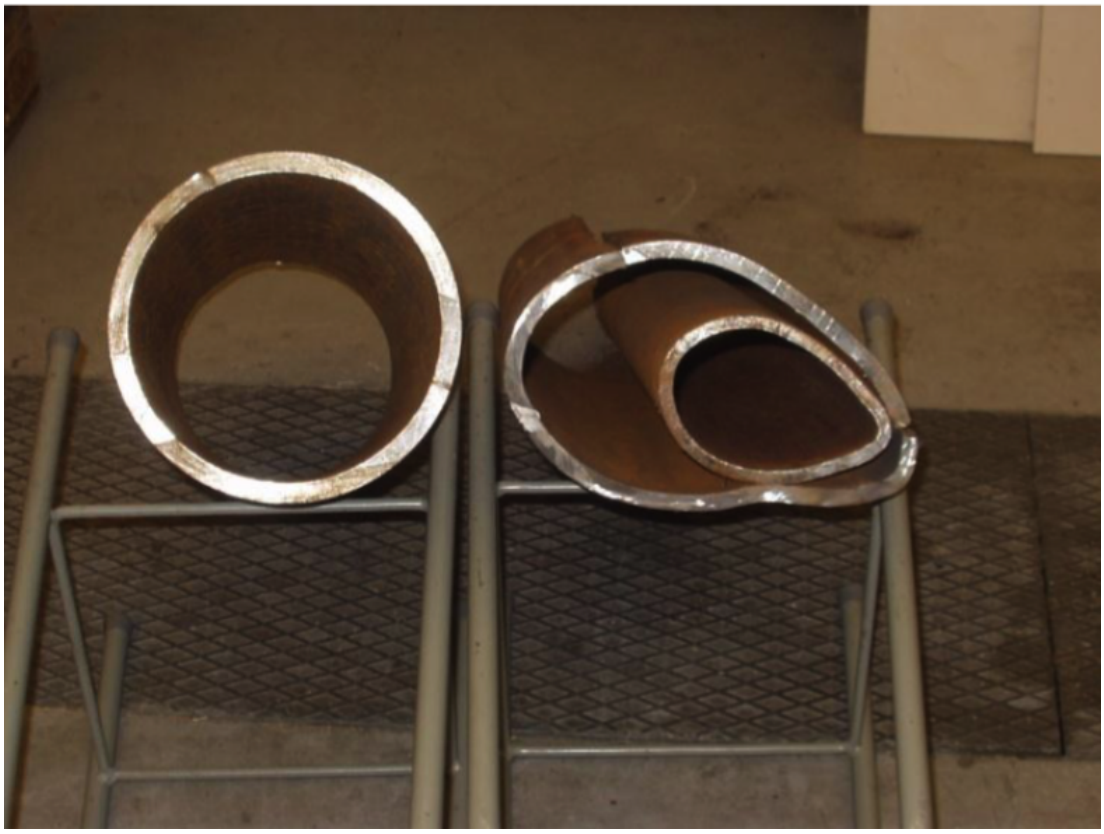

Figure 6: Collapsed production- casing and tubing [11]

2.5 Corrosion

Corrosion is a common problem encountered in the petroleum industry causing significant economic losses as well as problem in regards to safety and resource protection. Corrosion is a natural occurring process defined as the deterioration of a material as a result of chemical reactions between the surrounding environment and the material. Down-hole corrosion is an electrochemical reaction requiring the presence of [5]:

- Anode
- Cathode
- Electrolyte
- Electrucal Current

Corrosion consists of two half-cell reactions, a anodic and a cathodic. The anodic

reaction releases electrons while the cathodic reaction consumes the electrons, as illustrated in figure 7.

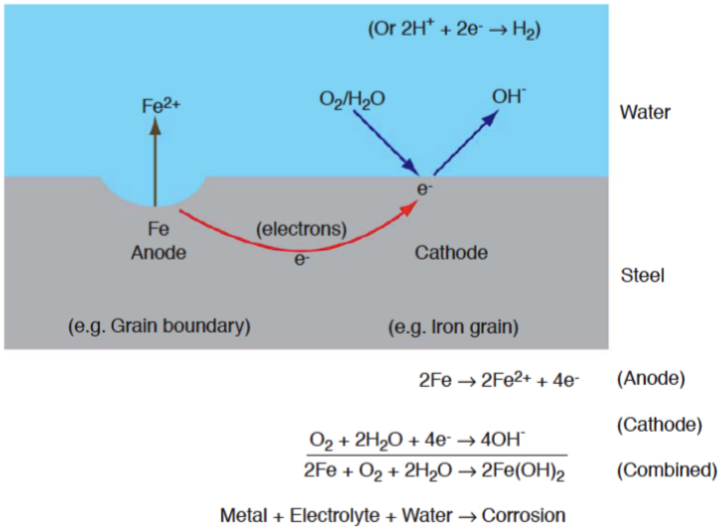

Figure 7: Corrosion reactions [5]

2.5.1 Localized Corrosion

Localized corrosion, also known as pitting corrosion, is one of the most destructive forms of corrosion. Pitting corrosion is a randomly occurring, highly localized form of attack on a metal surface. Typically for the pitting corrosion is that the depth of penetration is much larger than the diameter of the area affected. Local corrosion occurs when materials protective film or coating has been wore down, and is often observed in CO_2 and H_2S environment in the petroleum industry. Pitting is divided into two groups with several shapes as illustrated in figure8 [5].

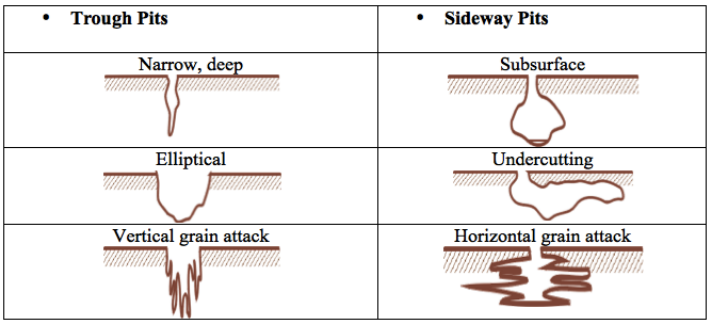

Figure 8: Pitting Corrosion [5]

Pitting corrosion can cause different shapes of wear on the pipe, such as; crescent-shaped, wedge-shaped and rectangular-shaped as illustrated in figure 9. These types of wears will affect the maximum pressure that a cylindrical pipe can sustain in regards to burst and collapse significantly. The wear types considered in the analysis in this thesis are inspired from the pitting corrosion types illustrated in figure 8. For instance, the narrow deep type looks like a wedge shaped wear, and the elliptical have a shape similar to a rectangle. These wears will be compared to each other in order to investigate how the different wears affects the maximum pressure a pipe can be subjected to before yielding occurs, and determine which type of wear is the most critical. Figure 10 shows a L80 13Cr tubing that has corroded locally.

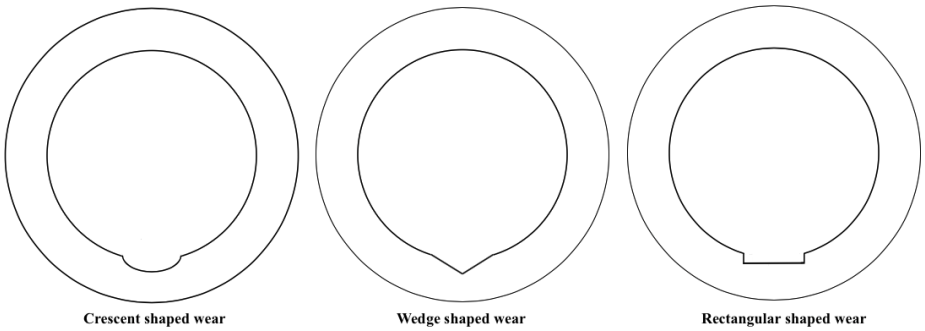

Figure 9: Different wear shapes

Figure 10: Locally corroded L80 13Cr tubing [5]

3 Theory

This chapter serve to present the theory of stress and failure criteria related to circular cylinders. During drilling, completion and production various types of metal cylindrical casings and tubing are installed. Under these operations the cylinders are exposed to various loads such as pressures, temperatures and bending which all generates stresses in the cylinders. Thus, in order to ensure full well integrity throughout the hole lifetime of the well it is important to perform stress analysis to evaluate the different scenarios in regards to burst, collapse, tensile and buckling that the casings and tubing experiences.

In general circular cylinders are classified into two categories:

1. Thick Walled Cylinder
2. Thin Walled Cylinder

3.1 Thick Walled Cylinder

A cylinder is defined as thick walled if the following condition applies, where t is the wall thickness and r_i is the inner radius of the cylinder [12]:

$$t > \frac{1}{10} r_i \tag{8}$$

Figure 11 illustrates a thick walled cylinder subjected to uniform pressure. The pressure generates stresses across the thickness of the cylinder along the radial, axial and circumferential direction.

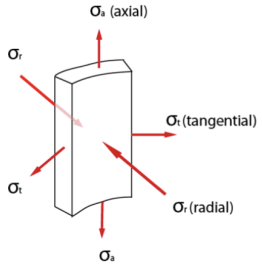

Figure 11: Stresses in a thick walled cylinder [5]

where,

- σ_r is defined as the radial stress across the wall thickness
- σ_θ is defined as the tangential (hoop stress) in the circular direction
- σ_a is defined as the axial stress along the axial direction

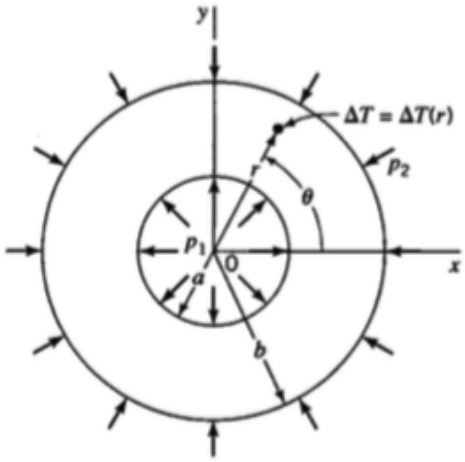

Figure 12: Illustration of the cross secton of a thick walled cylinder [12]

To ensure a safe operation these stresses needs to be determined. Combining the stresses generated by pressure and temperature the stresses is given by the following equations [12]:

3.1.1 Radial Stress

The radial stress is always in compression and varies from $-p_a$ at the inner radius to $-p_b$ at the outer radius.

$$\sigma_r = \frac{p_a a^2 - p_b b^2}{b^2 - a^2} - \frac{a^2 b^2}{(b^2 - a^2) r^2}(p_a - p_b) + \sigma_r(\Delta T) \tag{9}$$

where,

$$\sigma_r(\Delta T) = \frac{\alpha E \Delta T}{2(1-\nu) l n(\frac{b}{a})}\left[-l n(\frac{b}{r}) + \frac{a^2(b^2 - r^2)}{r^2(b^2 - a^2)} l n(\frac{b}{a})\right] \tag{10}$$

and p_a is the internal pressure, p_b is the external pressure, a is the inner radius of

the cylinder, b is the outer radius of the cylinder, r is any radial distance between radius a and radius b, $\sigma_r(\Delta T)$ is the radial stress due to temperature, E is the young modulus of the material, α is the coefficient of thermal expansion, ν is the Poisson's ratio and ΔT is the change in temperature from a reference state.

3.1.2 Hoop Stress

The hoop stress, also referred to as the tangential stress, is given by:

$$\sigma_\theta = \frac{p_a a^2 + p_b b^2}{b^2 - a^2} - \frac{a^2 b^2}{(b^2 - a^2) r^2}(p_a - p_b) + \sigma_\theta(\Delta T) \tag{11}$$

where $\sigma_\theta(\Delta T)$ is the tangential stress due to temperature and given as:

$$\sigma_\theta(\Delta T) = \frac{\alpha E \Delta T}{2(1-\nu) ln(\frac{b}{a})}\left[1 - ln(\frac{b}{r}) - \frac{a^2(b^2 - r^2)}{r^2(b^2 - a^2)} ln(\frac{b}{a})\right] \tag{12}$$

3.1.3 Axial Stress

The magnitude of the axial stress is dependent on whether the cylinder is open or closed. For open cylinders the axial stress is equal to zero. For closed cylinders the axial stress is given by:

$$\sigma_a = \frac{p_a a^2 + p_b b^2}{b^2 - a^2} + \sigma_a(\Delta T) \tag{13}$$

where $\sigma_a(\Delta T)$ is the is the axial stress due to temperature, and is given as $\sigma_r(\Delta T) + \sigma_\theta(\Delta T)$[12]

Note that for $\Delta T = 0$, $\sigma(\Delta T)$ becomes zero for all cases.

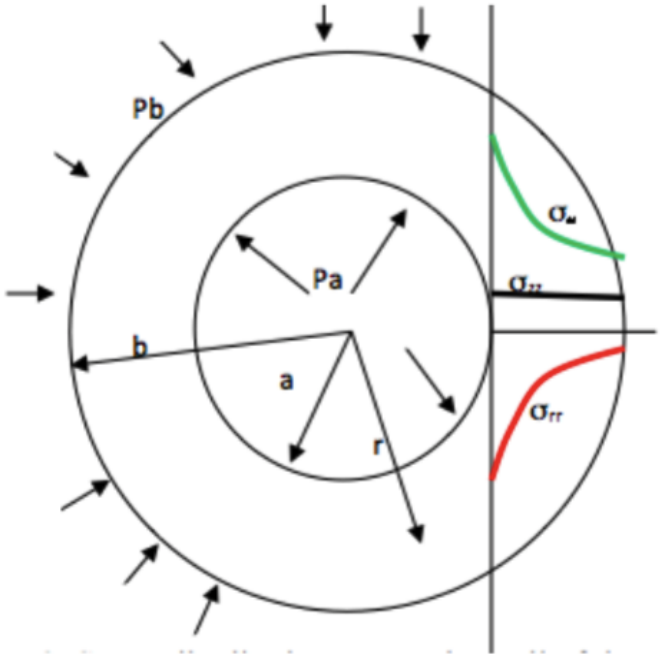

Figure 13: Stress distribution - thick-walled cylinder [12]

3.2 Thin Walled Cylinder

A cylinder is defined as thin walled if the following condition applies [12]:

$$t < \frac{1}{10} r_i \tag{14}$$

For the thin walled cylinder the hoop stress is equally distributed across the wall, and the radial stress varies from 0 at the outer radius to $-p$ at the inner radius. The axial stress is only present for closed-end cylinders. The equation for a thin walled cylinder is given as [13]:

3.2.1 Radial Stress

At inner radius:

$$\sigma_r = -p \tag{15}$$

At outer radius:

$$\sigma_r = 0 \tag{16}$$

3.2.2 Hoop Stress

$$\sigma_\theta = \frac{p\,r}{t} \tag{17}$$

3.2.3 Axial Stress

Open-end:

$$\sigma_a = 0 \tag{18}$$

Closed-end:

$$\sigma_a = \frac{p\,r}{2t} \tag{19}$$

3.3 Bending Stress

Bending stress (σ_b) may occur when drilling doglegs and when the pipe is buckling. To calculate the bending stresses beam theory is applied. The bending stresses is greatest at the outside of the pipe and is calculated from the following equation [5]:

$$\sigma_b = \pm\frac{E\,D}{2R} \tag{20}$$

where

- D is the outside diameter of the pipe
- R is the radius of the bend
- E is the young modulus

The positive sign represent tensile stresses on the outside of the bend, while the negative represents compressive stresses on the inside of the bend.

The bend radius can be calculated from the angle, α, or from the dogleg severity (DLS), normally given i degrees per 100 feet. By changing the diameter in Eq.20 to a value between outside and inside the bending stresses can be calculated at any point in the pipe. The bending stress caused by doglegs acts locally, thus bending the pipe in one location only raise stresses at that specific point and is not affecting stresses in other locations of the pipe. However, the bending stresses are added to the axial stresses, and since it can be positive and negative the total axial stresses may increase or decrease. The maximum and minimum axial stress when including bending can be calculated by:

Maximum axial stress

$$\sigma_b = \sigma_a + \sigma_b \tag{21}$$

Minimum axial stress

$$\sigma_b = \sigma_a - \sigma_b \tag{22}$$

3.4 Tri-axial well design - Failure Criteria and Design Factor

There are currently several models and techniques for estimating collapse and burst pressures of pipes used in drilling, completion and intervention. The most common for calculating burst equations throughout the years is the uni-axial Barlow's equation. The Barlow's equation has been a favorite due to its simplicity, however the equation has several shortcomings [14]. One of the shortcomings when deriving the formula is that it assumes a thin-walled pipe with no external pressure. Further, the equation neglects the axial loads effects. This works well for pipes such as casing with no axial load, but is not accurate for tubing or drill pipe. However, when it comes to pipes with no axial loads and a large diameter-to-thickness ratio the equation is fairly accurate[15].

3.5 Failure Criteria

3.5.1 Tresca Criterion

The maximum shear-stress criterion, also known as Tresca criterion, is based on the maximum and minimum principal stress. The criteria does not include the intermediate principle stress. For ductile metals the criteria exhibits good agreement with experimental results[12]. The criteria is defined as the following:

$$\sigma_y = \sigma_{max} - \sigma_{min} \tag{23}$$

where,

- σ_{max} = maximum principle stress
- σ_{min} = minimum principle stress
- σ_y = yield stress

3.5.2 Von Mises Criterion

The distortional strain energy density criterion, also known as Von Mises, is a criterion used for predicting the yielding of materials under combined stresses. This criterion includes the intermediate stress, and the initial yield stress is based the three principle stresses, axial stress, radial stress and hoop stress, and the shear stress (τ) caused by torque[12]. The criteria reads:

$$\sigma_{VME} = \sqrt{\frac{1}{2}\{(\sigma_\theta - \sigma_r)^2 + (\sigma_r - \sigma_a)^2 + (\sigma_a - \sigma_\theta)^2\} + 3\tau^2} \tag{24}$$

3.6 Design Factor

Design factors (DF) are considerations that must be met to ensure a safe operation. During installation and intervention the casings and tubing is subjected to various loads. Axial loads and bending produces tensile and compressive axial stresses in the pipes, while the external and internal pressure induces hoop and radial stresses. In addition, if torque is applied the pipes may experience shear stresses [15].

To predict the yield strength of well pipes simple uni-axial tension tests is performed experimentally. In this case, both σ_r (radial stress) and σ_h (hoop stress) are set to zero. The Von Mises equivalent stress for this case is given as [15]:

$$\sigma_{VME} = \sigma_y \tag{25}$$

According to Aasen and Aadnoy [15] the design factor (DF) is defined as the "ratio of the allowable stress to the working stress":

$$\text{DF} = \frac{\sigma_y}{\sigma_{VME}} \tag{26}$$

where the allowable stress is the yield strength of the pipe and the applied stress is the Von Mises equivalent stress. An increased design factor value means a higher failure margin, while a DF=1 is the theoretical failure point [15]

$$\text{DF} = \frac{\sqrt{2}\sigma_y}{\sqrt{(\sigma_a - \sigma_r)^2 + (\sigma_a - \sigma_h)^2 + (\sigma_r - \sigma_h)^2}} \tag{27}$$

By using dimensional analysis Aasen and Aadnoy [15] developed a simplified solution of the tri-axial design. In the derivation the effect of torque, temperature and bending was neglected, and the Lamè solution for radial and hoop stresses in a thick walled cylinder was used. During investigations of the equations is was found that both collapse and burst failures initiates at the inner surface of the tubular.

The maximum Von Mises stress is obtained at the inner surface of the pipe. By letting $r = r_i$, the equation for hoop (Eq. 11) and radial stress (Eq.9) (for thick

walled cylinder) on the inside wall can be written as:

$$\sigma_r = -p_i \tag{28}$$

$$\sigma_\theta = \beta(p_i - p_o) - p_i \tag{29}$$

where β is a geometry factor given as:

$$\beta = \frac{2r_o^2}{r_o^2 - r_i^2} = \frac{(d_o/t)^2}{2(d_o/t - 1)} \tag{30}$$

If bending is included, the axial stress is calculated as:

$$\sigma_a = \frac{F_a}{As} + \sigma_b = \sigma_a + \sigma_b \tag{31}$$

By performing a dimensional analysis the dimensionless variables were obtained:

$$x = (P_i + \sigma_a)\sigma_y \tag{32}$$

$$y = \beta(P_i - P_o)\sigma_y \tag{33}$$

By inserting x and y into Eq. 27 the design factor can be written as:

$$\mathrm{z} = \mathrm{DF} = \frac{1}{\sqrt{x^2 - xy + y^2}} = \frac{\sigma_y}{\sigma_{VME}} \tag{34}$$

The equation above represents an exact solution of burst and collapse calculations and describes a surface that represents the loads caused by axial stress, outside and inside pressure in relation to the yield strength.

Solving Eq. 34 for y, one obtains [15]:

$$y = \frac{x}{2}\sqrt{\frac{1}{\mathrm{SF}^2} - \frac{3}{4}x^2} \tag{35}$$

The plus sign is representing tensile force for burst, while the negative sign represents compressive forces for collapse. Figure 14 shows examples of different three-dimensional design factors projected onto a two-dimensional plane [15].

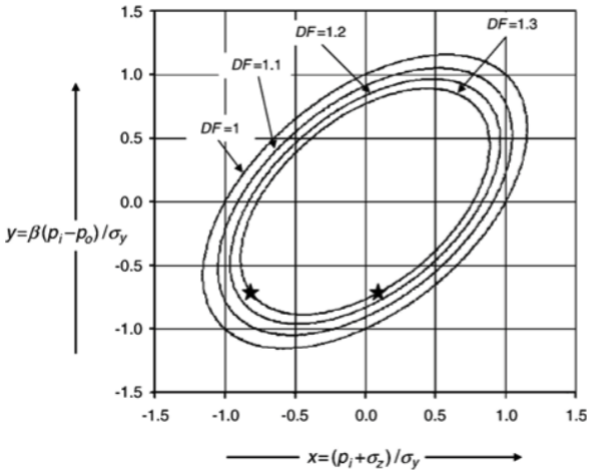

Figure 14: Three-dimensional design factors projected onto a two-dimensional plane [15]

3.7 Burst theory

Unworn cylindrical pipes that are subjected to internal or external pressures induces hoop stresses in the wall as shown in figure 15. The hoop stress is a tensile stress and it is highest at the inner diameter and decreasing towards the outer diameter. The higher internal pressures (p_i) the higher the tensile hoop stress (σ_θ), until it reaches the yield strength of the material. The hoop stress is balancing the internal and external pressures acting on the inner and outer surfaces [9].

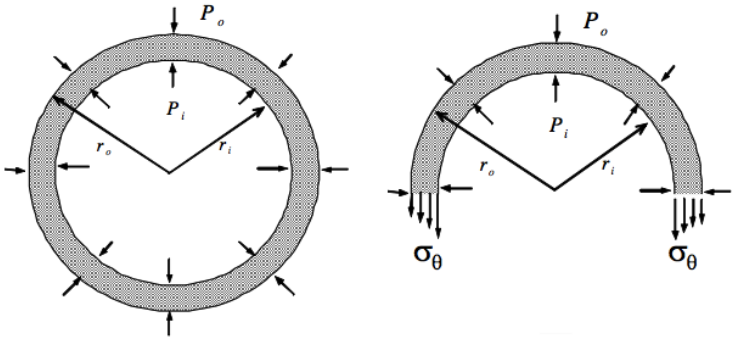

Figure 15: Hoop stress and internal pressure balance on a cylinder [9]

3.7.1 Burst Models - Thick-Walled Cylinder

Consider a case with zero external pressure (p_e), zero temperature difference and zero axial stress (σ_a). The principle stresses in equations (2), (4), (6) can be written as:

$$\sigma_r = \frac{p_a a^2}{b^2 - a^2} - \frac{a^2 b^2}{(b^2 - a^2) r^2}(p_a) \tag{36}$$

$$\sigma_\theta = \frac{p_a a^2}{b^2 - a^2} + \frac{a^2 b^2}{(b^2 - a^2) r^2}(p_a) \tag{37}$$

$$\sigma_a = \frac{p_a a^2}{b^2 - a^2} = 0 \tag{38}$$

Burst model based on tresca failure criteria:
Inserting equation (36), (37) and (38) into the trescra failure criteria (Eq.23) for $r = a$ and solving for P = P_y one can obtain the pressure that causes the yielding of

the inner wall of thick-walled cylinders:

$$P_y = \frac{\sigma_y}{2}\left(1-\frac{a^2}{b^2}\right) \tag{39}$$

Burst model based on Von Mises failure criteria:
Inserting (36), (37) and (38) into the Von Mises failure criteria (Eq. 24) and letting $r = a$, and solving for P = P_y the pressure that causes the yielding of the inner wall of the cylinders can be written as:

$$P_y = \frac{\sigma_y\left(1-\frac{a^2}{b^2}\right)}{\sqrt{\frac{a^4}{b^4}+3}} \tag{40}$$

3.7.2 Burst Models - Thin-Walled Cylinder

For a Thin-walled cylinder the principle stresses are given as[12]:

Hoop stress:

$$\sigma_\theta = \frac{Pr}{t} \tag{41}$$

Axial stress:

$$\sigma_\theta = \frac{Pr}{2t} \tag{42}$$

Radial stress:

$$\sigma_r = 0 \tag{43}$$

Burst model based on Tresca failure criteria:
By using the Tresca failure (Eq. 23) criteria and solving for the pressure that causes

the yielding of the inner pipe wall $P = P_y$ one obtain:

$$P\,y = \frac{\sigma_y\, t}{r_o} \tag{44}$$

Equation 44 is the Barlow's equation. The API burst rating (API Bulletin 5C3, 1999) for a thin-walled cylinder is based on the Barlow's equation. The API adds a tolerance factor of 87,5% assuming that 12,5% of the pipe wall thickness may have been removed by corrosion or wear effects[5]. Including this factor into equation 44 gives:

$$P_y = 0,875\frac{\sigma_y\, t}{r_o} \tag{45}$$

Burst model based on Von Mises failure criteria:
Inserting the principle stresses into the Von Mises failure criteria (Eq. 24) and solving for $P = P_y$ one obtain:

$$P_y = \frac{2\sigma_y\, t}{\sqrt{3}r} \tag{46}$$

3.8 API Collapse Models

The following API collapse models have been developed based on 2466 experimental data [5]. The collapse rating of a tubing is a more complex problem than burst as it is dependent on several properties of the pipe such as diameter, thickness and pipe ovality. The API Bulleting 5C3 (1999) defines four collapse modes: elastic, transitional, plastic and yield strength In order to select the appropriate collapse mode the ratio between the outside diameter and thickness (also known as the slenderness ratio) is determined. After the slenderness ratio (D/t) is determined table 4 is used to find the representative collapse mode for the steel grade. For each

collapse mode there is an associated empirical formula [5]:

Table 4: Collapse modes [5]

Grade (ksi)	Elastic (D/t)	Transitional (D/t)	Plastic (D/t)	Yield (D/t)
40	>42.64	27.01-42.64	16.40-27.01	<16.40
55	>37.21	25.01-37.21	14.81-25.01	<14.81
80	>31.02	22.47-31.02	13.38-22.47	<13.38
90	>29.18	21.69-29.18	13.01-21.69	<13.01
95	>28.36	21.33-28.36	12.85-21.33	<12.85
110	>26.22	20.41-26.22	12.44-20.41	<12.44
125	>24.46	19.63-24.46	12.11-19.63	<12.11
140	>22.98	18.97-22.98	11.84-18.97	<11.84
155	>21.70	18.37-21.70	11.59-18.37	<11.59

Elastic collapse

$$P_e = \frac{46.9510^6}{(D/t)[(D/t)-1]^2} \tag{47}$$

Transitional collapse

$$P_t = Y_p\left[\frac{F}{D/t} - G\right] \tag{48}$$

where the values for F and G can be found in table 5

Table 5: Transitional collapse factors [5]

Grade (ksi)	F	G
40	2.63	0.0325
55	1.989	0.036
80	1.998	0.0434
90	2.017	0.0466
95	2.029	0.0482
110	2.053	0.0515
125	2.106	0.0582
140	2.146	0.0632
155	2.188	0.0683

Plastic collapse

$$P_p = Y_p\left[\frac{A}{D/t} - B\right] - C \tag{49}$$

where the values for A,B and C can be found in table6

Table 6: Plastic collapse factors [5]

Grade (ksi)	A	B	C
40	2.95	0.0465	754
55	2.991	0.0541	1206
80	3.071	0.0667	1955
90	3.106	0.0718	2254
95	3.124	0.0743	2404
110	3.181	0.0819	2852
125	3.239	0.0895	3301
140	3.297	0.0971	3751
155	3.356	0.1047	4204

Yield collapse

$$P_y = 2Y_p\left[\frac{(D/t)-1}{(D/t)^2}\right] \tag{50}$$

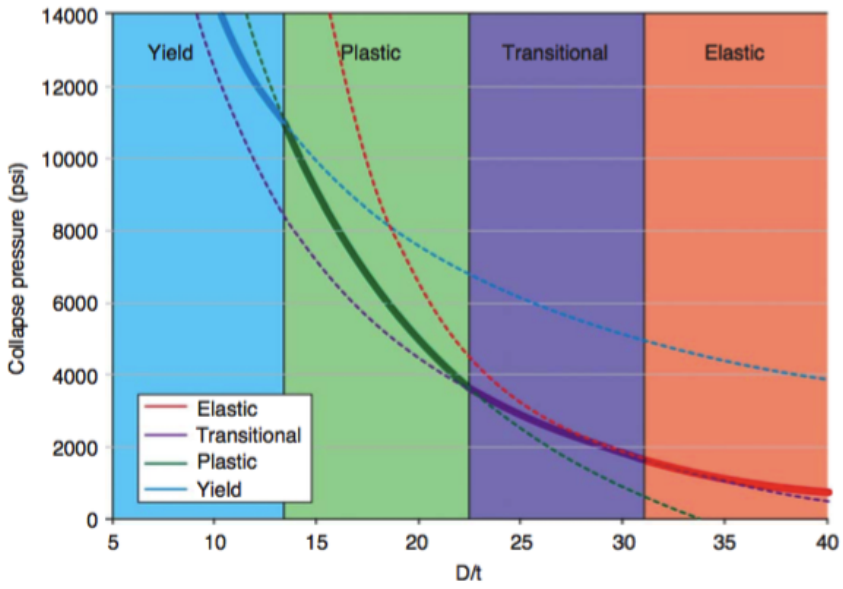

Figure 16: Example of collapse pressure as a function of slenderness - L80 tubing [5]

3.9 Fracture Mechanics

Failures due to fracture of materials is an important issue when it comes to human safety, environment and economics. The most common reasons for fracture failures are uncertainties in loadings, inadequate design, and deficiencies in maintenance or construction. Thus, the design against fractures is a very important area of research. When a fracture in an material occur the local stresses can be modified to such an extent that the elastic stress analysis performed by the designer is not sufficient enough. When a fracture reaches an certain critical length it can propagate through the structure. This can happen even though the stress is less than the stress that would normally cause the material to yield [16].

3.9.1 Energy Balance Approach

A.A Griffith (1893-1963) is one of the pioneers in the studies of fracture mechanics, especially known for employing one of the most famous energy-balance approach within material science. The strain energy per volume of stressed material (U*) is given by [16]:

$$U^* = \frac{1}{V}\int f\,dx = \int \frac{f}{A}\frac{dx}{L} = \int \sigma\,d\epsilon \tag{51}$$

For a linear material ($\sigma = E\epsilon$), the strain energy per volume is:

$$U^* = \frac{E\epsilon^2}{2} = \frac{\sigma^2}{2E} \tag{52}$$

As a crack grows into a solid to a depth a, a region of the material adjacent to the free surfaces is unloaded and the strain energy is released. Griffith computed the amount of this released strain energy. The energy release is visualized in figure 17. Figure 17 illustrates two triangular regions near the crack flanks, with a height β_a

and width a, that is unloaded, while the rest of the material feels the full stress σ [16]

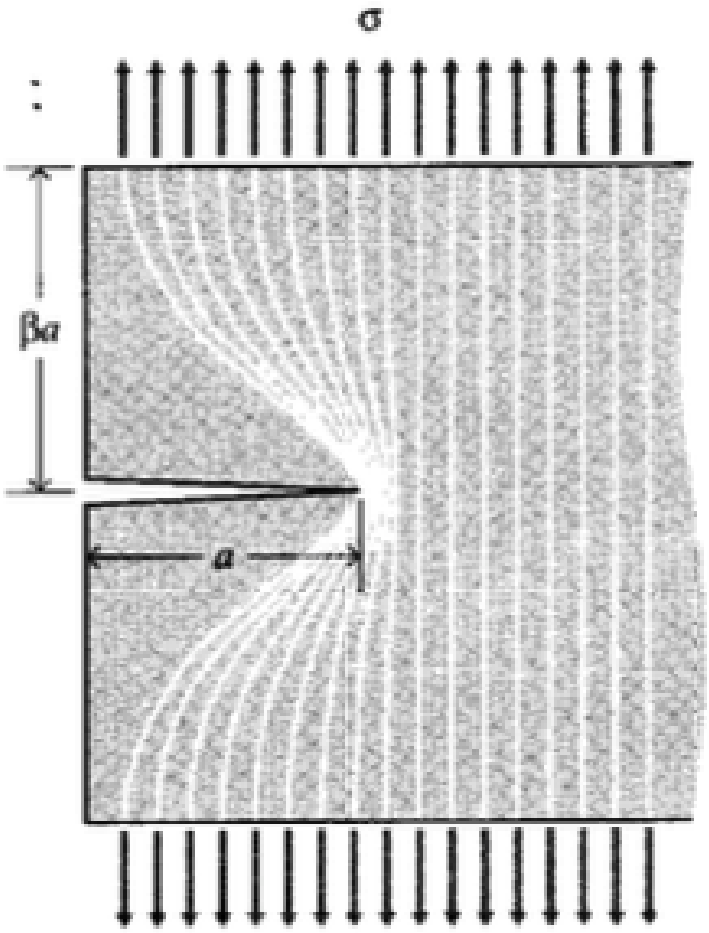

Figure 17: Idealization of unloaded region near crack flanks [16]

For plain stress loading $\beta = \pi$ and the total strain energy, U, released is given as:

$$U = -\frac{\sigma^2}{2E}\pi a^2 \tag{53}$$

The dimension normal to the $x-y$ plane is taken to be unity, thus, U is the strain energy released per unit thickness of the material. This strain energy is liberated by crack growth. During crack growth, bond is broken, and the bond energy is absorbed by the material. The surface energy S, for a crack with length a is given

as:

$$S = 2\gamma a \tag{54}$$

where factor 2 is included due to the two new free surfaces and γ is the surface energy (Joules/meter^2).

The total energy related to the forming of the crack is the sum of the strain energy liberated by allowing the regions near the crack flanks to become unloaded, which is a negative value, plus the positive value of the energy absorbed due to the new surfaces, as shown in figure 18 below [16].

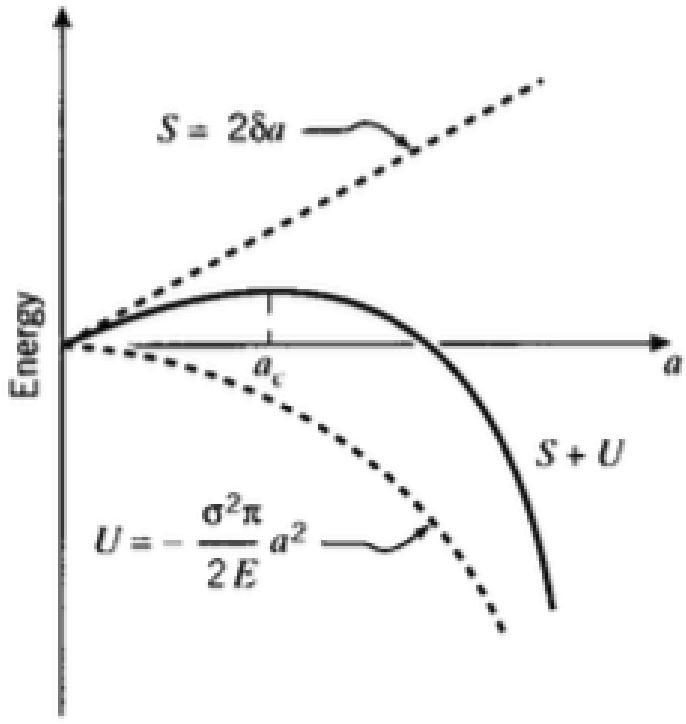

Figure 18: Fracture energy balance [16]

As the length of the crack grows (a increases), the strain energy eventually dominates the surface energy. Up to a_c (critical crack length) the crack only grows if the stress increases. Beyond the critical length of the crack, a_c, the system lowers the energy by increasing the crack further, here the crack growth is spontaneous [16].

The value of a_c (critical crack length) can be found by derivating the total energy $S+U$ and setting it to zero:

$$\frac{\partial(S+U)}{\partial a} = 2\gamma - \frac{\sigma^2}{E}\pi a = 0 \tag{55}$$

Solving 55 for σ gives:

$$\sigma = \sqrt{\frac{2E\gamma}{\pi a}} \tag{56}$$

However, equation 56 by Griffith is only valid for brittle materials, such as glass rods. For more ductile materials, Irwin and Orowan suggested that the majority of the released strain energy was absorbed by energy dissipation due to plastic flow in the material near the tip of the crack, and not by creating new surfaces. Thus, the Griffith equation was rewritten in the form [16]:

$$\sigma = \sqrt{\frac{EG_c}{\pi a}} \tag{57}$$

The rewritten Griffith equation above describes the relation between three important aspects related to the fracture process, the stress level, σ, the material, with its associated critical strain energy release, G_c, and the size of the fracture, a. During design situations the value of a may be based on a the smallest cracks that is easily detected. For a given material with a known G_c, E (youngs modulus) and a the stress level could be determined by the use of equation 57. To avoid fracturing the structure should therefore be sized to keep the stress level below this critical value.

3.9.2 The Stress Intensity Approach

The energy-balance gives a great understanding of the fracture process, however in engineering practice an alternative method that focus on the stress state near the tip of a sharp crack has been proven more useful. In figure 19 three types of cracks are illustrated. In this thesis we will focus on fracture mode I, known as the normal-opening mode [16]. The dots in the equations below indicates second and higher order terms. For distances less than 0.1 x length of the crack, the second order and higher in the equations is neglected. Figure 20 illustrates the stress state near a tip of a crack in a coordinate-system.

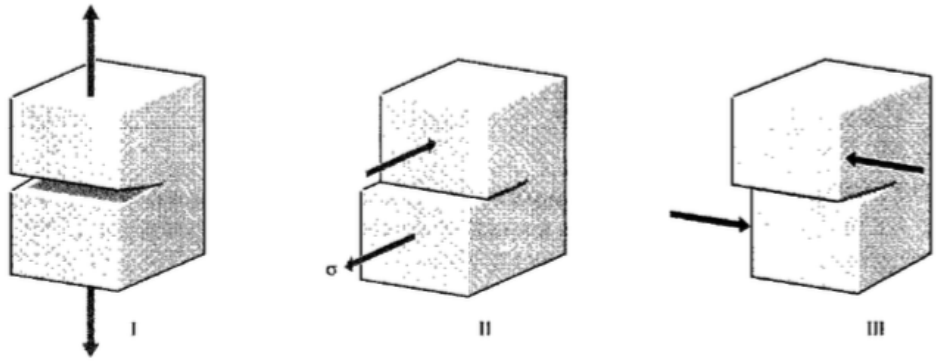

Figure 19: Fracture energy balance [16]

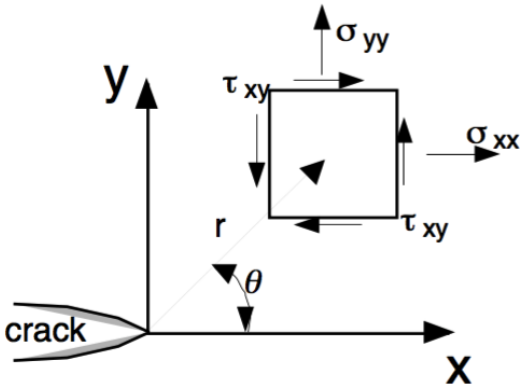

Figure 20: Stresses near crack tip [17]

The normal opening-mode stresses given written as:

$$\sigma_x = \frac{K_I}{\sqrt{2\pi r}} cos\frac{\theta}{2}\left(1 - sin\frac{\theta}{2}sin\frac{3\theta}{2}\right) + ... \tag{58}$$

$$\sigma_y = \frac{K_I}{\sqrt{2\pi r}} cos\frac{\theta}{2}\left(1 + sin\frac{\theta}{2}sin\frac{3\theta}{2}\right) + ... \tag{59}$$

$$\tau_{xy} = \frac{K_I}{\sqrt{2\pi r}} cos\frac{\theta}{2}cos\frac{3\theta}{2}sin\frac{\theta}{2} + ... \tag{60}$$

Where r is the distance from the crack tip a the stress field, K_I is the stress intensity factor, and θ is the angle from the tip to the stress field (see figure 20) [16]. Figure 21 shows how different angles (from $-180°$ to $+180°$ degrees) affects the different stresses.

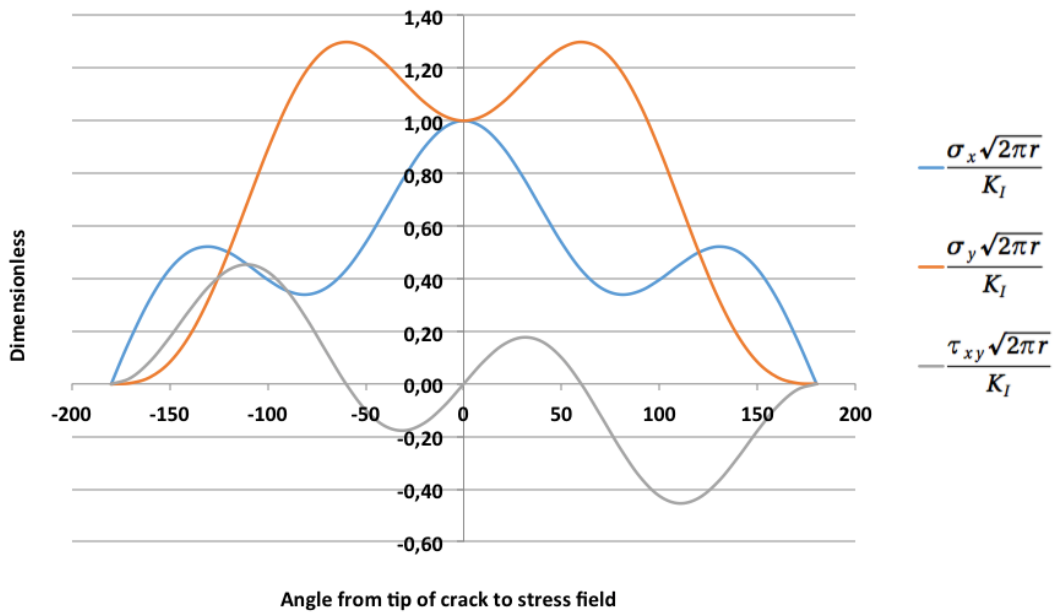

Figure 21: The effect of angle on the different stresses related to fracture

4 Finite Element Method

The Finite Element Method (FEM) is a numerical method used for solving problems of engineering and mathematical physics. The most common areas within engineering and mathematics physics where FEM is used to solve difficulties are structural analysis, transfer of heat, electromagnetic potential, fluid flow and transportation of mass. Problems that includes complicated geometries, material properties and loadings generally makes it difficult to obtain an analytical mathematical solution. The finite element method subdivides a large problem into smaller units or bodies that are called finite elements in a system of algebraic equations. While analytical solutions solves the problem for the whole body in one operation, the finite element method gives a solution of the entire body by formulating the equations for each finite element and combine them [18]. In this thesis the software Abaqus has been used.

4.1 Finite Element Method Steps

This section presents the steps that are included in a FEM formulation and solution. There are three key simulation steps: idealization, discretization and solution, all steps are a source of error.

4.1.1 Idealization

Mathematical modeling, also known as idealization, is the process where a mathematical model of the system has been obtained based on a physical system. A model, in this case, is defined as "a symbolic device built to simulate and predict aspects of behavior of a system".

The process is called idealization because a mathematical model only abstract aspects of interest from a physical system, and not the whole system. The results from the analytical or numerical produced by the mathematical model are physically re-interpreted only for those aspects. However, engineering systems ten to be very

complex and in order to simulate a system it is necessary to reduce the complexity. This can be done by filtering out physical details that are not relevant for the design and analysis process.

The physical simulation process is illustrated in figure 22.

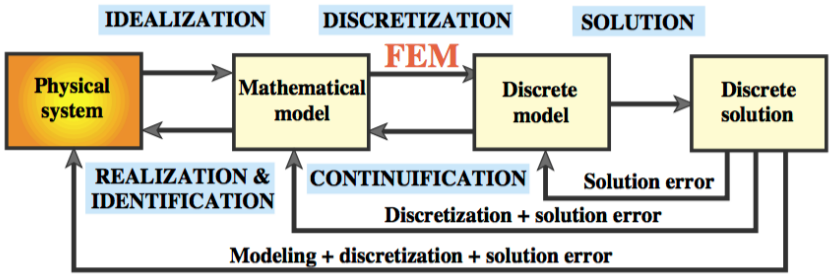

Figure 22: Physical simulation process [19]

4.1.2 Discretization

Mathematical modeling is a simplification of the reality. However, models of physical systems can very be difficult to solve. The models often includes coupled partial differential equations in time and space subjected to boundary and interface conditions with a infinite number of degrees of freedom.

In order to make a numerical simulation practical it is necessary to perform a discretization. A discretization involve reducing the number of degrees to a finite number and the product of the discretization process is a discrete model [19].

4.1.3 Error Sources and Approximation

All steps are a source of errors. Figure 22 above shows each simulation step and the source of error it introduces. The modeling errors are not very important, however, there is a need for access to and comparison with experimental results to achieve model validation.

Another important error is the discretization error. The computed solution of the discrete model is only a approximation to the mathematical model. A quantitative

measurement of the disagreement between the discrete model and mathematical model is called the discretization error [19].

4.1.4 The Finite Element Method

The finite element method is the most frequently used technique concerning discretization within structural mechanics. The FEM is interpreted from a mathematical or physical viewpoint. The concept of the physical FEM is the subdivision of the mathematical model into components of simple geometry referred to as infinite elements. The finite number of degrees of freedom expresses the response of each element, characterized as the value of a function at a set of nodal points. The discrete model the connected finite elements creates is model that the mathematical model is approximated from [19].

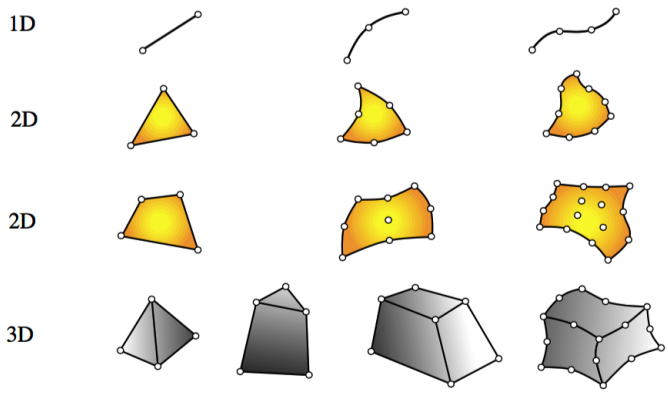

Figure 23: Typical finite element geometries in 1D, 2D and 3D [19]

4.1.5 Element Nodes, Geometry and Degrees of Freedom

All elements consists of a set of nodal points. These nodal points defines the element geometry (geometric nodal points) and serve as a home for degrees of freedom (connection nodal points). Usually the elements has nodal points located either at the corners or end points. For elements of higher order the nodal points can also be placed on sides or faces.

The placement of the geometric nodal points defines the element geometry. Usually the elements have simple geometries, in one-dimension the elements are ei-

ther straight lines or curved segments, while in two dimensions they are either triangular or quadrilateral shape. The elements in three dimension are normally tetrahedral, pentahedra and hexahedra.

The state of the element is specified by the element degrees of freedom, also referred to as DOF. The DOFs connects the elements that is close to each other and is defined as "the values (and possible derivatives) of a primary field variable at connector node points" [19].

4.2 FEM Model Generation

All models used in this thesis have been created from scratch. In order to create a model there are several processing steps that needs to be performed. The first steps are to build the geometry, in this case the cylindrical tubing, and the meshes. Then material properties are added, together with loads, problem type and boundary conditions, if there are any. The models are generated by the following steps:

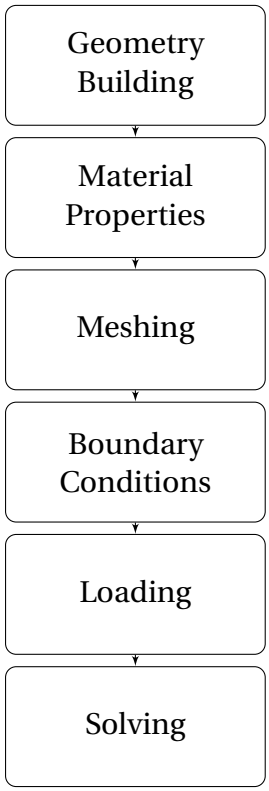

Figure 24: Steps of generating the models in Abaqus

4.2.1 Input Data

All simulations in this thesis is based on following input data collected from the well at the Ekofisk Field [2].

Table 7: Well Data [2]

Well Input Data	
Completion fluid density	8,6 ppg
DLS @ max penetration	2,9 deg.
TVD @ max penetration	1626 ft.

Table 8: Coiled Tubing Specifications [2]

Coiled Tubing Specifications	
OD	2,875 in.
r_o	1,4375 in.

Table 9: Tubing Specifications and Material Properties [2]

Production Tubing Specifications - L80 13Cr	
Outside diameter, d_o	5.500 in
Inside diameter, d_i	4.892 in
Wall thickness, t	0.304 in
Yield Strength	80000 psi
Density	0.284 lb/in^3
E-modulus	30×10^6 psi
Poisson's ratio	0.2

4.2.2 Geometry Building

The models built in this thesis were created based on the tubing dimensions used in the well in the Ekofisk Field (see table 9 for details). In order to analyse and compare the effect the different wear shapes have on the tubing several models were build. To simplify the models as much as possible, the crescent wear scar is assumed to have the dimensions of the coiled tubing (see table 8 for details). For the wedge shaped scar and rectangular scar a constant width of 1 inch was assumed since there are no actual data related to these types of wears. The wear shape geometry

is also assumed to be symmetrical. The wedge shaped scar and rectangular scar is assumed to be present due to local corrosion (pitting).

All models were built manually in a X-Y-Z coordinate system. The coordinates is entered relative to the origin at (0,0). For each indentation depth a new model was built. First the cross section of the models is built in a X-Y coordinate system, the length of the tubing is added later. The center of the tubing is at the origin, thus the outer and inner radius is are inserted with respect to this point.

4.2.3 Crescent Shaped Scar

Figure 25 illustrates the geometry of the crescent scar model. The wear depths determines the position of the coiled tubing center and outer radius.

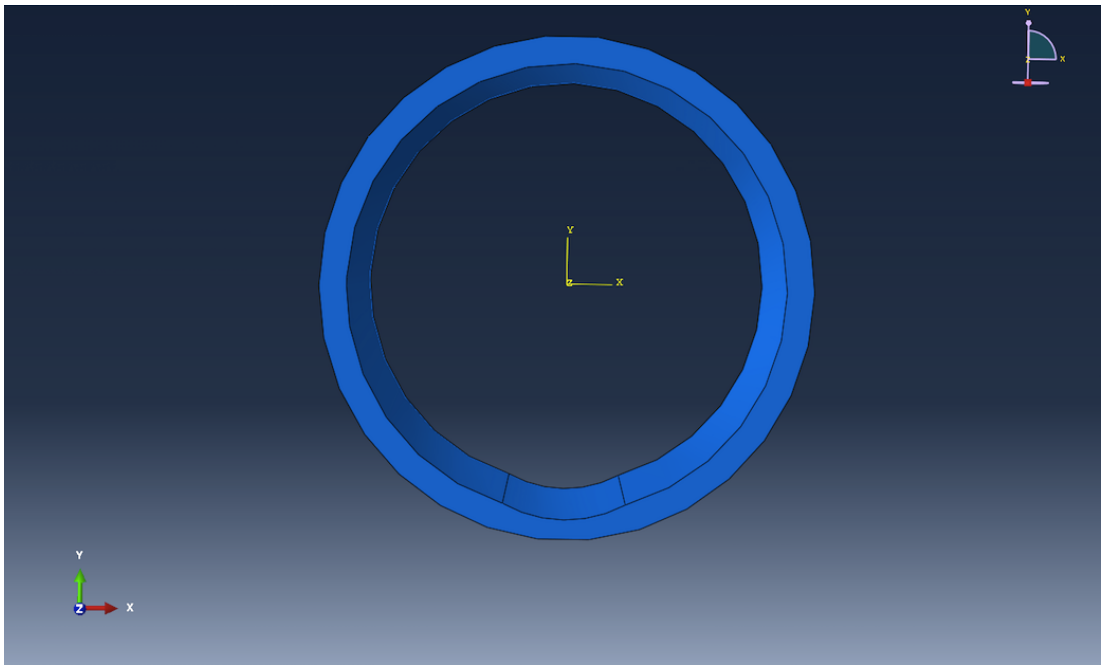

Figure 25: The geometry of a tubing with an crescent shaped wear

4.2.4 Wedge Shaped Scar

For the geometry of the wedge shaped wear, the same indentation depths as for the crescent wear where used. However, the width of the wedge shaped wear is held constant at 1 inch, thus, only the wear depths varies.

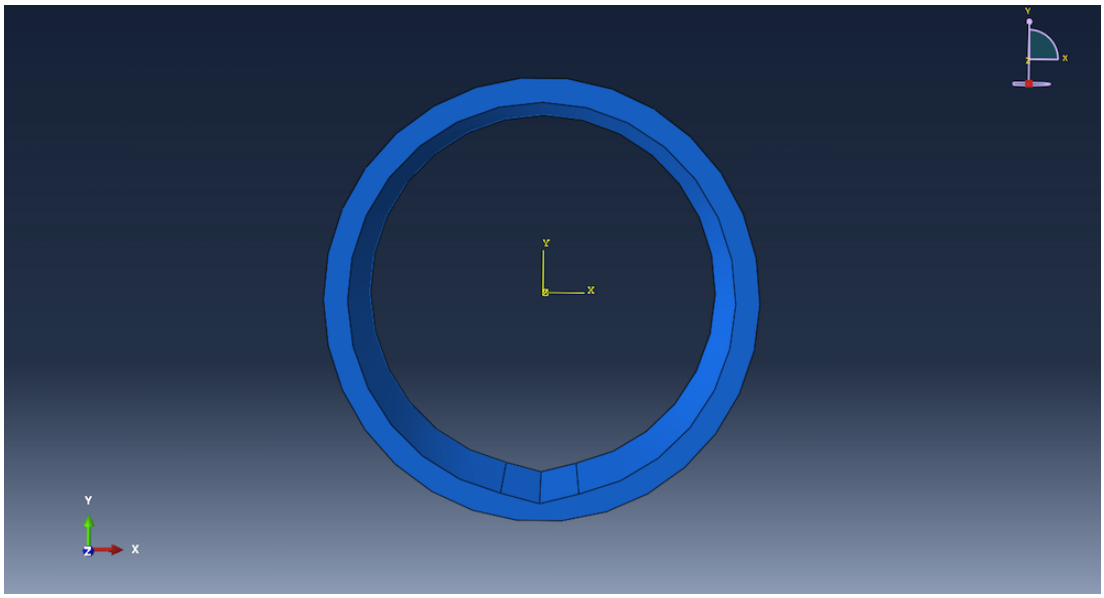

Figure 26: The geometry of a tubing with an wedge shaped wear

4.2.5 Rectangular Scar

Similar to the wedge shaped wear, the width of the rectangular scar is held constant at 1 inch and only the wear depths varies.

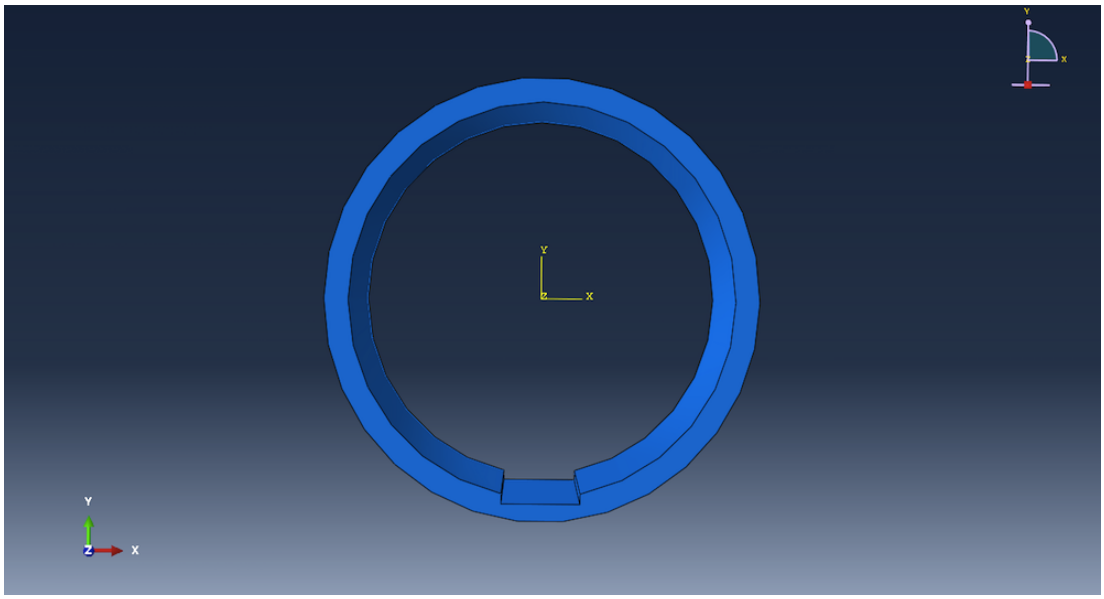

Figure 27: The geometry of a tubing with an rectangular shaped wear

4.2.6 Meshing

Meshing is the process of discretizie the geometry into small pieces often referred to as cells or elements. The meshing process involves creating the coarsest elements that can be used to cover the dominating physical behavior of the system. In areas suck as cracks and corner, the stress is highly concentrated. This are important areas of interests and should have meshes that is fine, and not course [20].

In this thesis a bilinar Q8 element with a degree of freedom of 8 has been used for meshing the models. Since corners and crack are present during the simulations in this theses, a seed size equal to 0.1 has been used. For the 2D model a seed size of 0.075 was selected to get the best possible results.

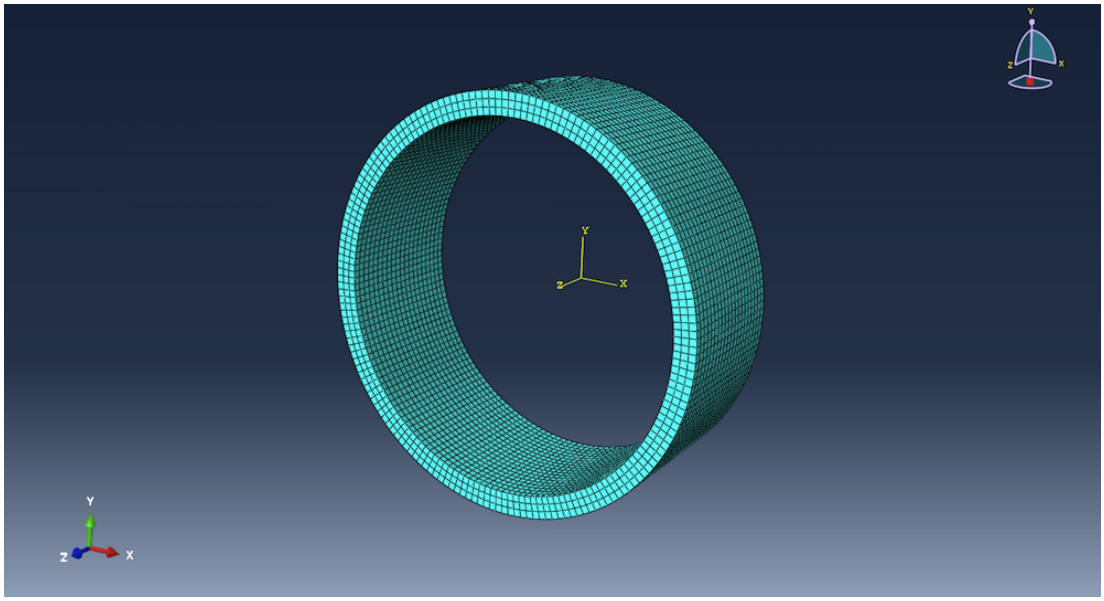

Figure 28: Meshed model of a unworn tubing

4.2.7 Boundary Conditions

The boundary conditions during the simulations are set to open ends since we only simulate a cross section of the tubing.

4.2.8 Loading

Both pressure and temperature are added as loadings. The pressure loadings are varied in order to find a trend line. Internal loadings is due to the fluids inside the tubing, while external loadings is due to the fluids in the annulus of the tubing.

4.3 FEM Simulation Procedure

In this thesis the FEM simulations are based on input data from a real well where all the data are provided by ConocoPhillips. The purpose of these simulations is to study the effect the different wear shapes and wear depth have on the burst and collapse strength of the tubing under various scenarios. The target was to evaluate which wear shape that is the most critical in regards to burst and collapse, and to check if the standard models that assumes a uniform wear are valid for the different local wears. Three types of wear shapes are considered in the simulations. They are referred to as crescent shaped wear, wedge shaped wear and rectangular shaped wear. As previously mentioned, the crescent shaped wear can be caused by coiled tubing intervention or corrosion, while the other two types of wear is assumed caused by pitting corrosion since there are no actual data for these types of wears. However, since there is a theoretical possibility that these types of wears occurs due to local corrosion, it is interesting to include these types of wears in the simulations. The effect of temperature is also included at a lated stage.

All scenarios have a reference model. The first step was to simulate the unworn reference model to determine the maximum internal and external pressure the tubing could withstand before reaching the yield stress limit of 80000 psi. Then the models were simulated with different wear depths from 5% up to 50%, with a five percent increase for each model. For each wear percent there were performed multiple simulations to find where the Von Mises stress exceeded the yield stress. In addition, in order to create a slope, there were performed simulations where the Von Mises stress was below the yield stress and above the yield stress. Wear percent (wear %) is the wear depth (indentation depth) caused by the coiled tubing or corrosion relative to the wall thickness of the tubing. The eccentricity is the

coiled tubing center relative to the tubing center.

Table 10: Wear positions details - Coiled Tubing

Wear %	Wear depth [in]	Eccentricity [in]	Indentation depth [in]
0	0.0000	1.0085	2.4460
5	0.0152	1.0237	2.4612
10	0.0304	1.0389	2.4764
15	0.0456	1.0541	2.4916
20	0.0608	1.0693	2.5068
25	0.0760	1.0845	2.5220
30	0.0912	1.0997	2.5372
35	0.1064	1.1149	2.5524
40	0.1216	1.1301	2.5676
45	0.1368	1.1453	2.5828
47	0.1428	1.1514	2.5889
50	0.1520	1.1605	2.5980

5 Results

This chapter presents the simulated results obtained from burst and collapse modeling. Various scenarios were designed and the FEM results are compared with the API models.

5.1 Burst Modeling: Single Scar

A well experiences various types of loadings during it's lifetime. During this productivity period the production tubing is exposed to different events which can cause wears, such as intervention, corrosion or erosion. To ensure a sufficient well integrity it is therefore important to determine how much load the tubing can withstand before the material yields. As previously mentioned, the Barlow's equation is used as a company standard for calculating burst pressure. In the upcoming sections the applicability of the Barlow's equation for local wear is investigated. A simulation based model will be introduced for each wear shape and compared to the Barlow's method. The effect of temperature will also be included at a later stage.

Table 11: Burst Scenario Data

Burst Scenario	
Well fluid gradient	0,3 psi/ft
Completion fluid gradient	8,6 ppg
Depth of maximum wear (47%)	1626 ft. TVD
Tubing material	L80
Yield Strength	80000 psi

Events that can cause internal loads can be exerted by fluids produced from the reservoir, injected fluids during intervention operations such as acid stimulation, bull-heading, or pressure build ups caused by reservoir fluids during shut in. The following burst simulations are inspired by these scenarios. Based on the data gathered from the Ekofisk Field (table 11) a external pressure caused by the completion

fluid at 1626 ft. TVD (depth of maximum wear) was calculated:

$$P_{ext} = 8,6ppg \times 0,052 \times 1626ft = 727psi \tag{61}$$

The external pressure of 727 psi is kept constant during all burst scenarios.

5.1.1 Uniform Wear Method - Investigation

As previously mentioned, the API burst and collapse models that are used today assumes that the tube is uniform. For a damaged tubing, the current practice used to calculate the de-rated burst and collapse resistance is by uniformly removing the worn out part. The question is how reliable is?

In order to investigate if the uniform wear method (which is a assumption in the Barlow's equation) is applicable for local wears, a test model with a uniform wear was compared to several models with different local scars. The Barlow's formula is assuming a uniform wear reduction of the entire internal circumference, while for a local wear only a small portion of the inner wall is reduced. The tri-axial stresses in the tubing wall for different local wears and a uniform wear were studied.

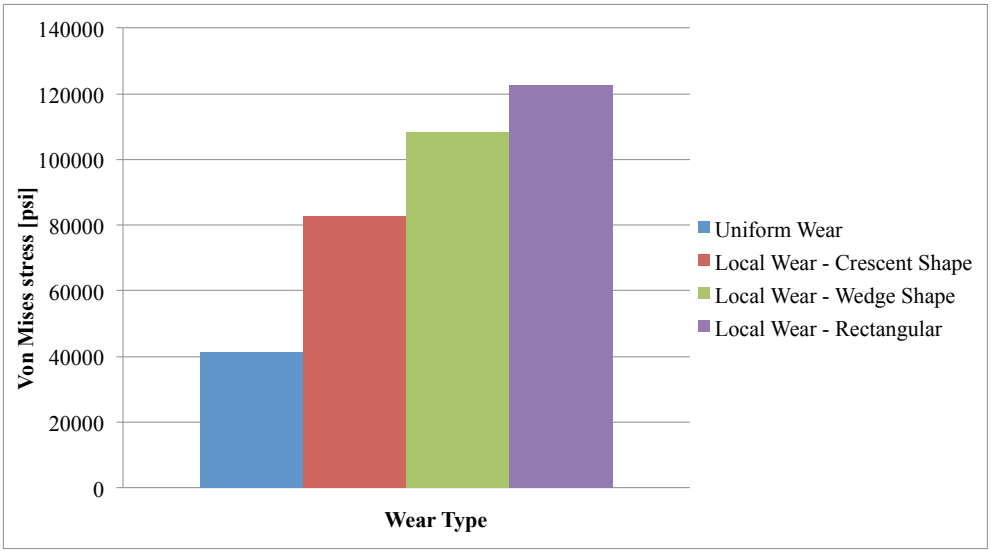

Figure 29: Von Mises stress for a uniform wear and different local wears under a internal pressure of 3500 psi

Figure 29 shows the Von Mises stresses for the different local wears and the uniform wear. The models used during the simulations had a wear depth of 40%, and for all cases the same internal pressure psi was applied. With a internal pressure of 3500 psi the model with a local rectangular shaped wear showed a Von Mises stress of 122700 psi. The local wedge shaped wear and crescent shaped wear showed a Von Mises stress of 108500 psi and 82590 psi, respectively. For the model where the Barlow's method is used (minimum wall thickness for the entire circumference), the Von Mises stress is found to be only 41220 psi. According to these simulations the locally worn tubing shows a significant higher Von Mises stress than the tubing with a uniform wear.

In figure 30, two of the simulated models are illustrated. The model to the left in the figure shows the uniform wear model, while the model to the right shows the model with a local wedge shaped wear (40% wear depth). For the uniform wear model the stress distribution is equal around the inner wall, while for the local wear model the stress is concentrated within the scar area. Based on this observations it is reasonable to state that the Barlow's equation can not be used to predict the burst pressure if the tubing is locally worn.

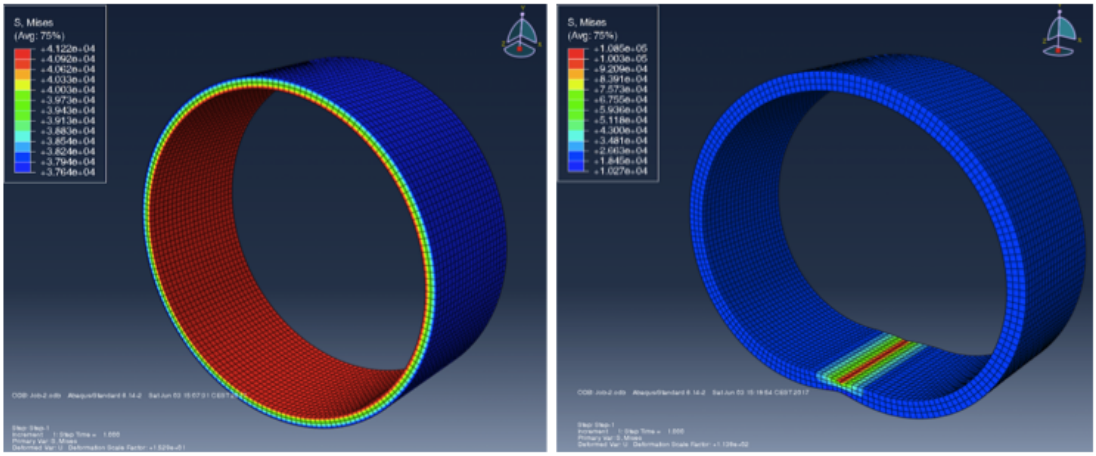

Figure 30: Uniform Wear (left) vs Local Wedge Shaped Wear (right)

5.1.2 Burst Scenario

The following sections presents the simulated results of the different types of wear shapes and how they affect the internal pressure that the tubing can withstand before the material yields. The different wear shapes will first be introduced separately, then compared to each other.

5.1.3 Reference Model - 0% wear

All the simulated wear shapes have the same reference model. Figure 31 shows that with a internal pressure of 9700 psi the Von Mises Stress is equal to 80530 psi. Safety factor is not included. For the 0 % reference model the tubing material reaches the yield limit when the internal pressure is between 9600-9700 psi, as shown in figure 12. The bold text in table 12 gives the maximum internal pressure the material can withstand before yielding, calculated by interpolation.

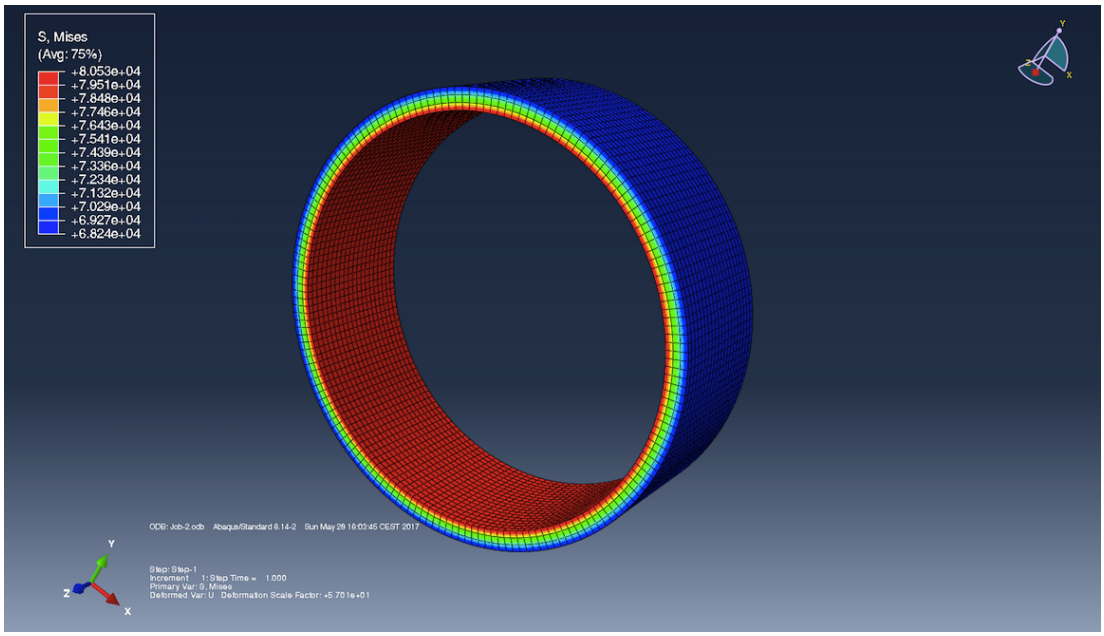

Figure 31: Unworn reference model with internal pressure of 9700 psi

Table 12: Internal Pressure and Von Mises Stress for model with 0% wear

Internal Pressure [psi]	Von Mises Stress [psi]
9800	81430
9700	80530
9641	**80000**
9600	79630

5.1.4 Crescent Shaped Wear

The next sections presents the simulated burst results for a single crescent shaped wear.

5.1.4.1 Crescent Shaped Wear - 25% Wear Model

For a crescent shaped wear of 25%, the tubing started to yield to an internal pressure of 4718 psi. This is a reduction of 51% compared to the reference model with no wear. Figure 32 shows the tubing under an internal loading of 4800 psi. Table 13 shows the simulated data for this model.

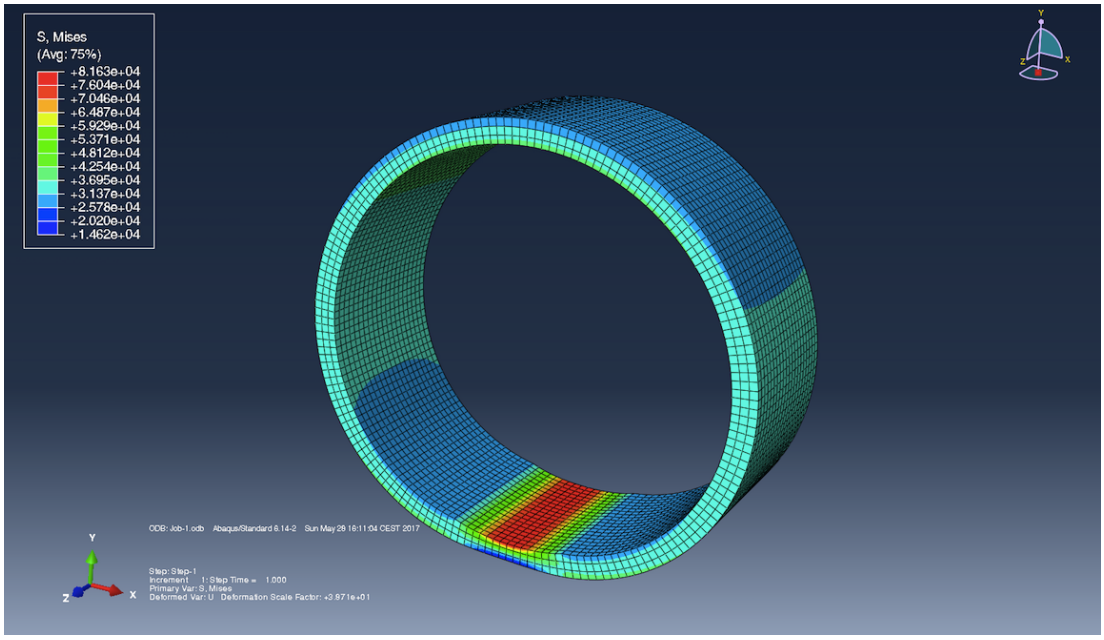

Figure 32: Simulated model with 25% wear and a internal pressure of 4800 psi

Table 13: Internal Pressure and Von Mises Stress for model with 25% wear

Internal Pressure [psi]	Von Mises Stress [psi]
4800	81630
4718	**80000**
4700	79620
4600	77600

5.1.4.2 Crescent Shaped Wear - 47% Wear Model

For a crescent shaped wear of 47%, which was the maximum wear scar that the multi-fingered caliper log recorded, the pressure to onset the yielding of the tubing material was calculated to be 2988 psi. This is a reduction of approximately 69 % when compared to the reference model with no wear. Table 14 shows the simulated data for this model.

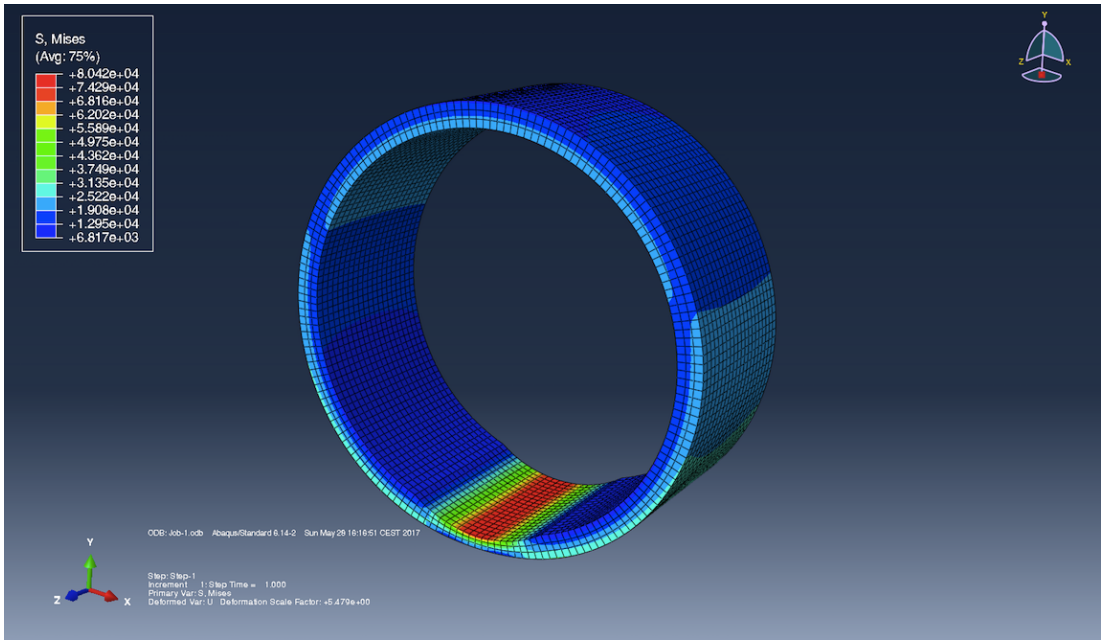

Figure 33: Simulated model with 47% wear and a internal pressure of 3000 psi

Table 14: Internal Pressure and Von Mises Stress for model with 47% wear

Internal Pressure [psi]	Von Mises Stress [psi]
3000	80420
2988	**80000**
2900	76870
2800	73320

5.1.4.3 Crescent Shaped Wear - Final Results - Burst

Figure 34 illustrates the linear slopes of different internal pressures for different wear depths. When the wear depth increases, the internal pressure that cause yielding of the material decreases, as expected. Table 15 shows the maximum pressure before the material yields for different wear depths. To find the respective internal pressure that generates a Von Mises stress equal to the yield stress limit (80000 psi), linear interpolation has been implemented.

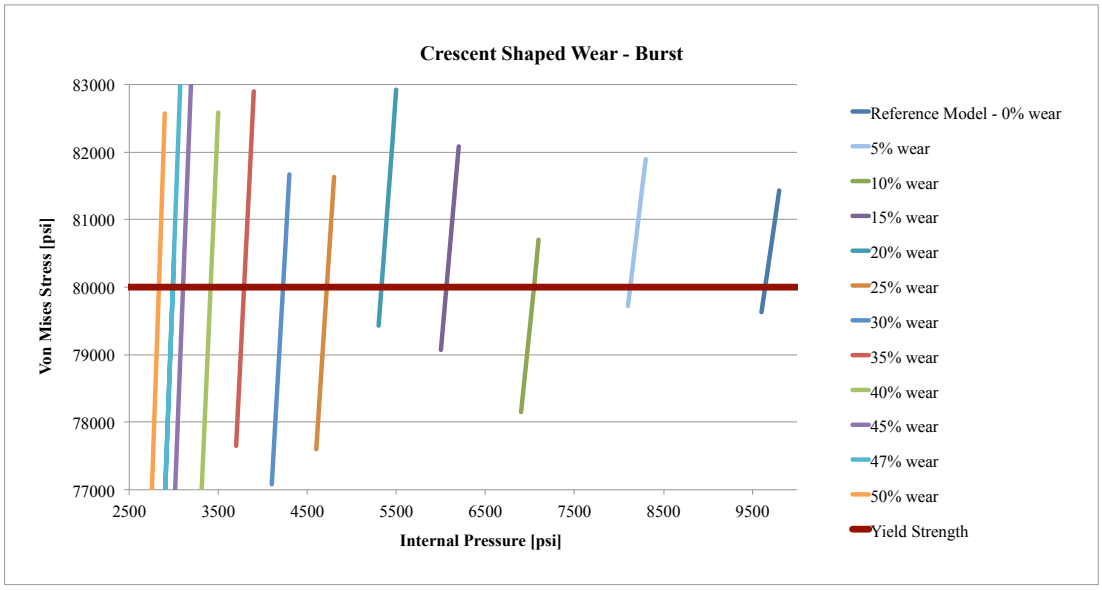

Figure 34: Internal pressure and the respective Von Mises Stress for different wear depths

Table 15: Result from linear interpolation for burst

Burst Pressure [psi]	Wear %
9641	0
8125	5
7045	10
6061	15
5333	20
4718	25
4227	30
3789	35
3414	40
3104	45
2988	47
2832	50

Figure 35 shows the safe and failure zones for the operating internal pressure. The area above the curve represents the failure zone (yielding) and the area under the curve represents the safe operational zone. Figure 35 also shows a generated simulation based model for the burst pressure.

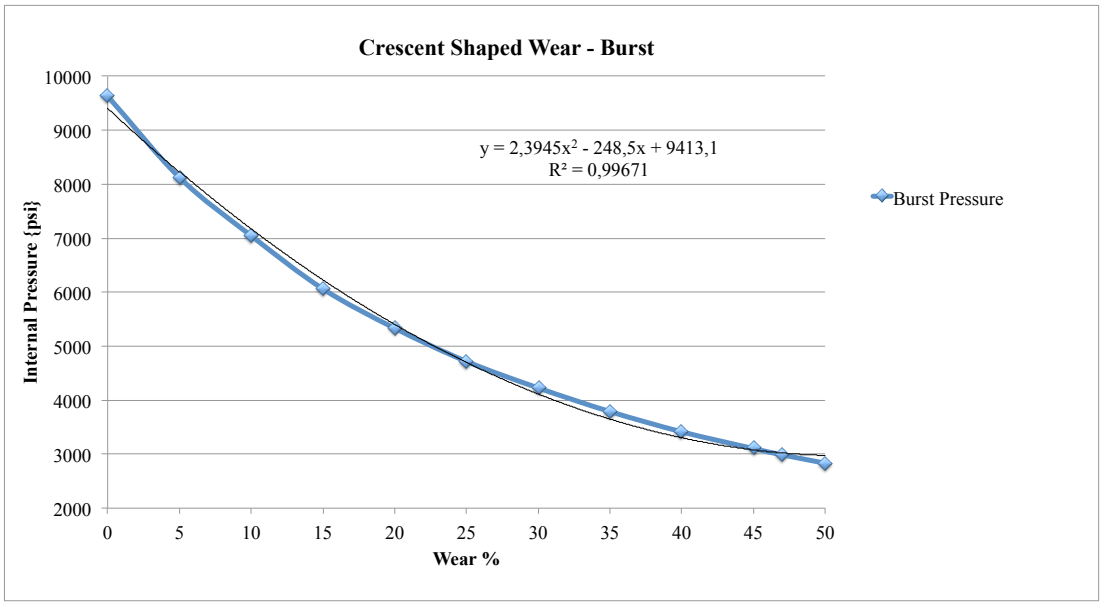

Figure 35: Safe and failure zone for operating internal pressure

Simulated model for burst pressure:

$$P_{int} = 2,3945 \times WEAR\%^2 - 248,5 \times WEAR\% + 9413,1 \tag{62}$$

The value of the coefficient of determination, $R^2 = 0,99671$ indicates that the simulated data fits the statistical model. In order to match the Barlow's model for burst pressure for an unworn tubing a design factor of approximately 0,82 was applied to the model based on the simulations. The models are illustrated in figure 36.

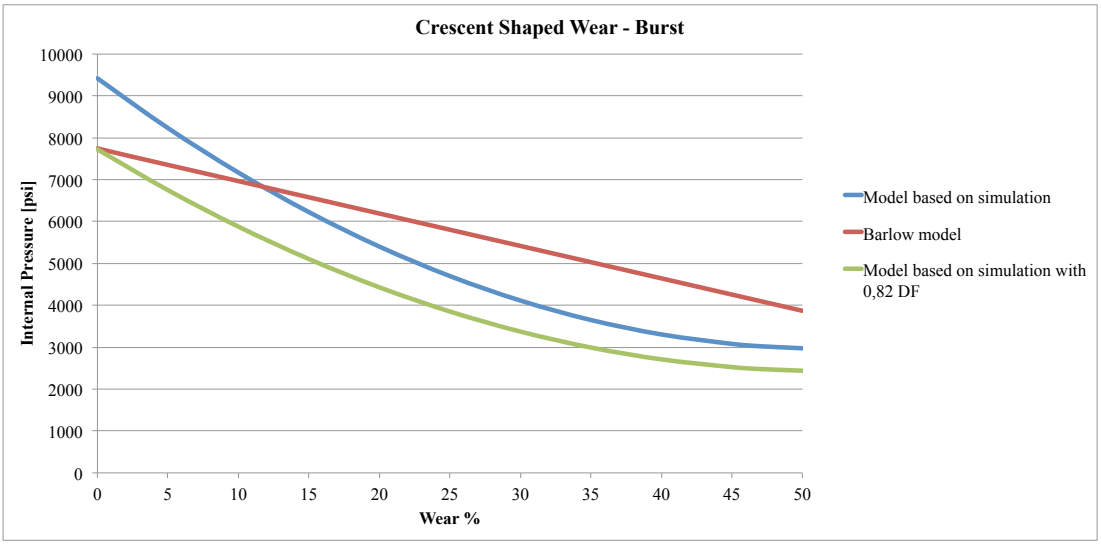

Figure 36: Barlow's model compared with the models based on simulation

As seen in figure 36 there is a significant difference between the linear Barlow's model and the simulated model for the local wear. When including the design factor in the non-linear simulated model the operational window has decreased significantly compared to the Barlow's model. Thus, the Barlow's equation overestimates the damaged tubings ability to withstand internal pressure.

Table 16: Data from the curves in figure 36

Wear %	Simulated results [psi]	Simulated model [psi]	Simulated model with 0,82 DF [psi]	Barlow's model [psi]
0	9641	9413	7719	7738
5	8125	8230	6749	7351
10	7045	7168	5877	6964
15	6061	6224	5104	6577
20	5333	5401	4429	6191
25	4718	4697	3852	5804
30	4227	4113	3373	5417
35	3789	3649	2992	5030
40	3414	3304	2710	4643
45	3104	3079	2525	4256
47	2988	3023	2479	4101
50	2832	2974	2439	3869

5.1.5 Wedge Shaped Wear

The next sections presents the simulated burst results for a single wedge shaped wear. As previously mentioned, the wear width is held constant at 1 inch.

5.1.5.1 Wedge Shaped Wear - 25% Wear Model

For a wedge shaped wear with 25% wear depth the tubing started to yield with an internal pressure of only 4305 psi. Compared to the reference model with no wear this is a reduction of approximately 55%. This is also 4% more than for the crescent shaped wear. Figure 37 illustrates the tubing under an internal loading of 4400 psi. Table 17 shows the simulated data, where the bold text is the pressure that causes the tubing to yield.

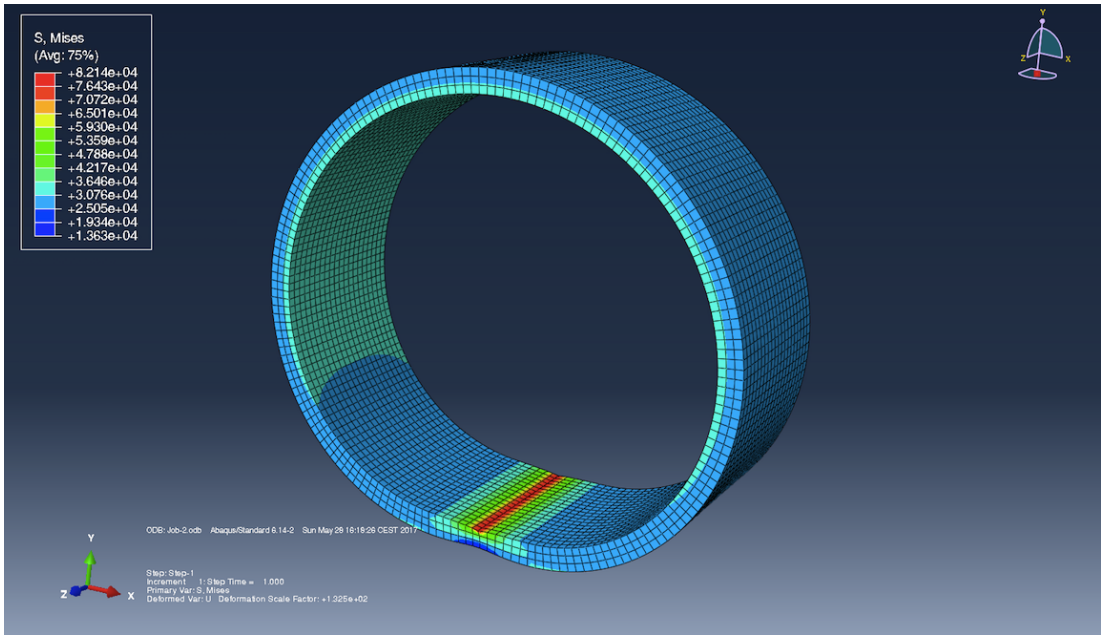

Figure 37: Simulated model with 25% wear and a internal pressure of 4400 psi

Table 17: Internal Pressure and Von Mises Stress for model with 25% wear

Internal Pressure [psi]	Von Mises Stress [psi]
4400	82140
4305	**80000**
4300	79890
4200	77650

5.1.5.2 Wedge Shaped Wear - 47% Wear Model

The results from the simulation of a wedge shaped wear with 47% wear depth show that the tubing started to yield with an internal load of 2317 psi. Compared to the reference model with no wear this is a reduction of approximately 76%. Almost 7% more than for the crescent shaped wear with 47% wear depth. Figure 38 illustrates the tubing under an internal loading of 2400 psi. Table 18 shows the simulated data, where the bold text is the pressure that causes the tubing to yield.

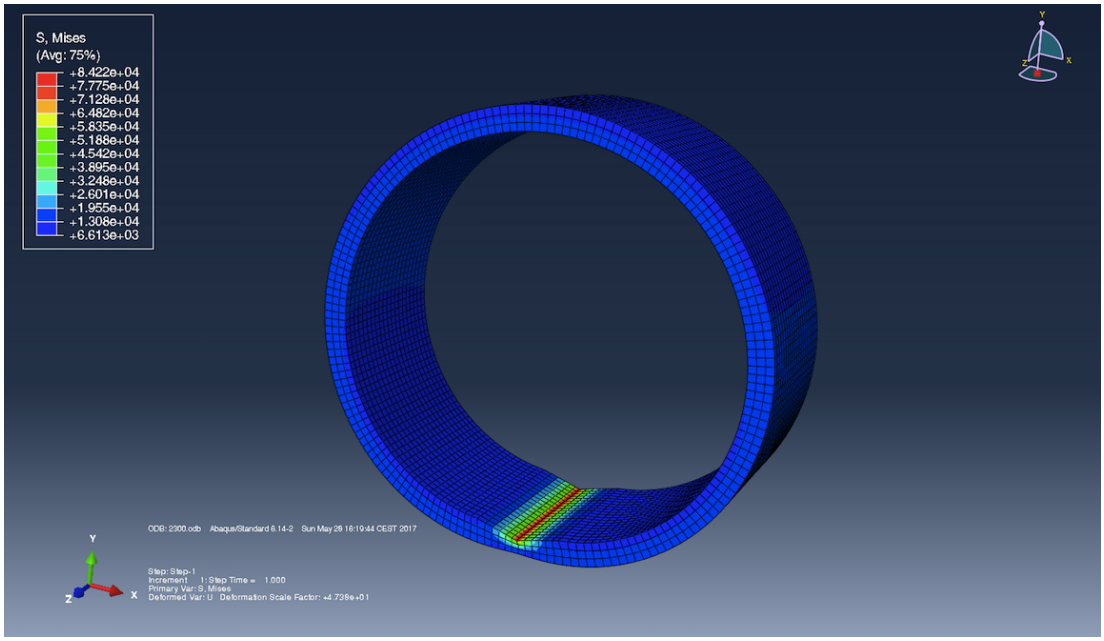

Figure 38: Simulated model with 47% wear and a internal pressure of 2400 psi

Table 18: Internal Pressure and Von Mises Stress for model with 47% wear

Internal Pressure [psi]	Von Mises Stress [psi]
2400	84220
2317	**80000**
2300	79160
2200	74110

5.1.5.3 Wedge Shaped Wear - Final Results - Burst

Figure 39 illustrates the linear slopes of different internal pressures for different wear depths. For a increased wear depth, the internal pressure that causes the material to yield decreases. Table 19 shows the maximum pressure before the material yields for different wear depths. To find the intersection of the yield strength and the internal pressure slopes linear interpolation has been implemented.

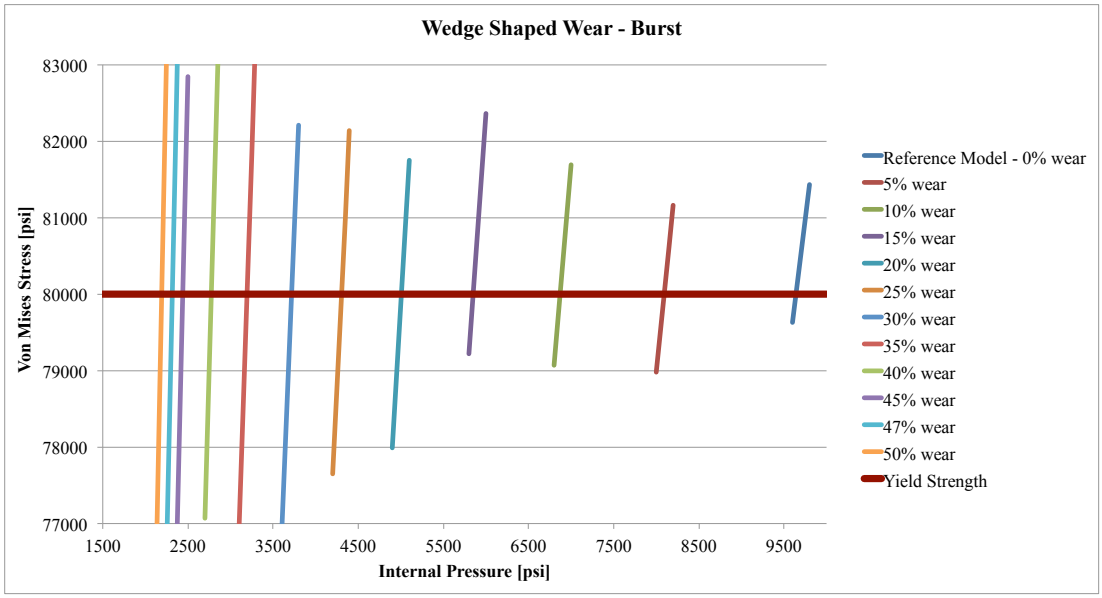

Figure 39: Internal pressure and the respective Von Mises Stress for different wear depths

Table 19: Result from linear interpolation for burst

Burst Pressure [psi]	Wear %
9641	0
8094	5
6870	10
5850	15
5007	20
4305	25
3717	30
3195	35
2775	40
2439	45
2317	47
2192	50

Similarly as for the crescent shaped wear, the safe and failure zones for the operating pressure is illustrated in figure 40. The area under the curve represents the safe operational window, while the area above represent the failure zone. Figure 40 also illustrates a generated simulation curve and model for burst pressure.

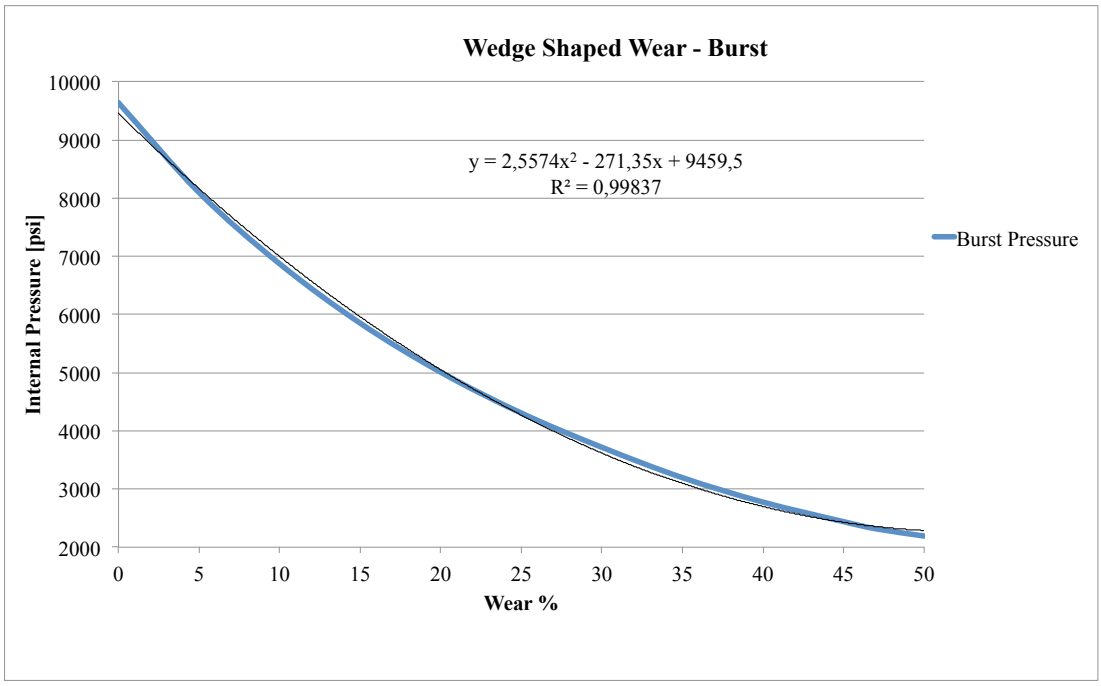

Figure 40: Safe and failure zone for operating internal pressure

Simulated model for burst pressure generated from the curve in figure 40:

$$P_{int} = 2,5574 \times WEAR\%^2 - 271,35 \times WEAR\% + 9459,5 \tag{63}$$

The coefficient of determination value, R^2, is equal to 0,99837, indicating that the simulated data fits the statistical model well. The model is generated in figure 41. A design factor of 0,82 has been included into the model based on the simulation in order to match the Barlow's model for burst pressure for an unworn tubing. The models are illustrated in figure 41.

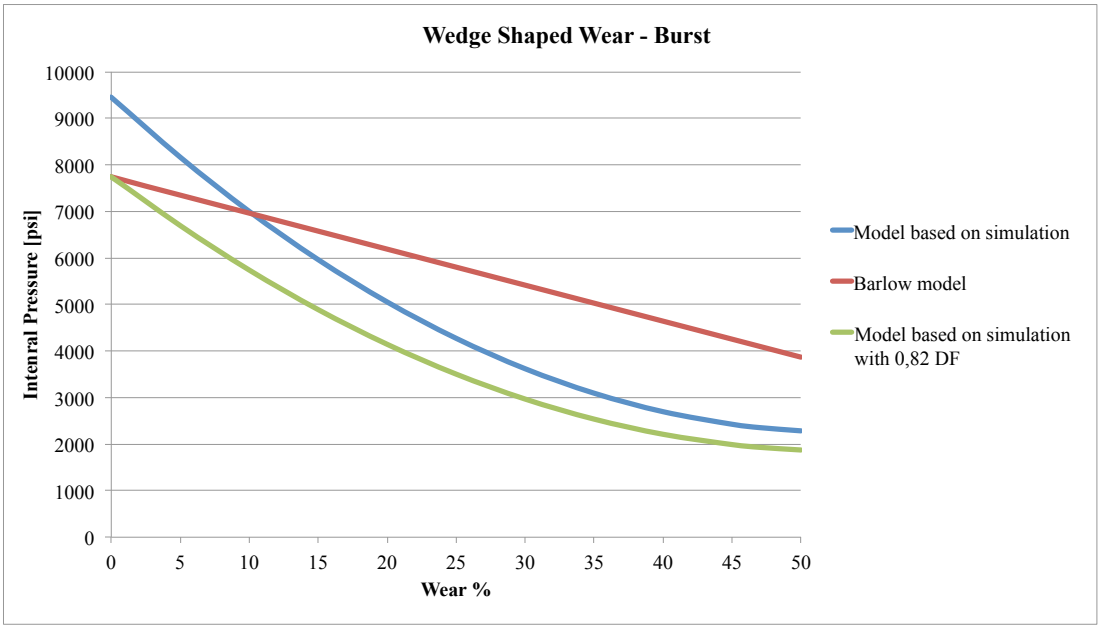

Figure 41: Barlow's model compared with the models based on simulation

The same trend as for the crescent shaped wear is observed in figure 41. Barlow's model is overestimating the tubings ability to withstand pressure for all the different wear depths. When the design factor is included the operational window drastically decreases compared to the Barlow's model.

Table 20: Data from the curves in figure 41

Wear %	Simulated results [psi]	Simulated model [psi]	Simulated model with 0,82 DF [psi]	Barlow's model [psi]
0	9641	9640	7757	7738
5	8094	8167	6697	7351
10	6870	7002	5751	6964
15	5850	5965	4891	6577
20	5007	5055	4145	6191
25	4305	4274	3505	5804
30	3717	3621	2969	5417
35	3195	3095	2538	5030
40	2775	2697	2212	4643
45	2439	2427	1991	4256
47	2317	2355	1931	4101
50	2192	2286	1874	3869

5.1.6 Rectangular Shaped Wear

The following sections presents the simulated burst results for a single rectangular shaped wear. The wear width is held constant at 1 inch.

5.1.6.1 Rectangular Shaped Wear - 25% Wear Model

For the 25% wear depth model of an rectangular shaped wear there is a reduction in the maximum internal pressure before the material yields of 62%, when compared to the reference model (unworn). The tubing started to yield to an internal pressure of 3582 psi. Table 21 shows the simulated data for the 25% wear model.

Table 21: Internal Pressure and Von Mises Stress for model with 25% wear

Internal Pressure [psi]	Von Mises Stress [psi]
3600	80500
3582	**80000**
3500	77680
3400	74560

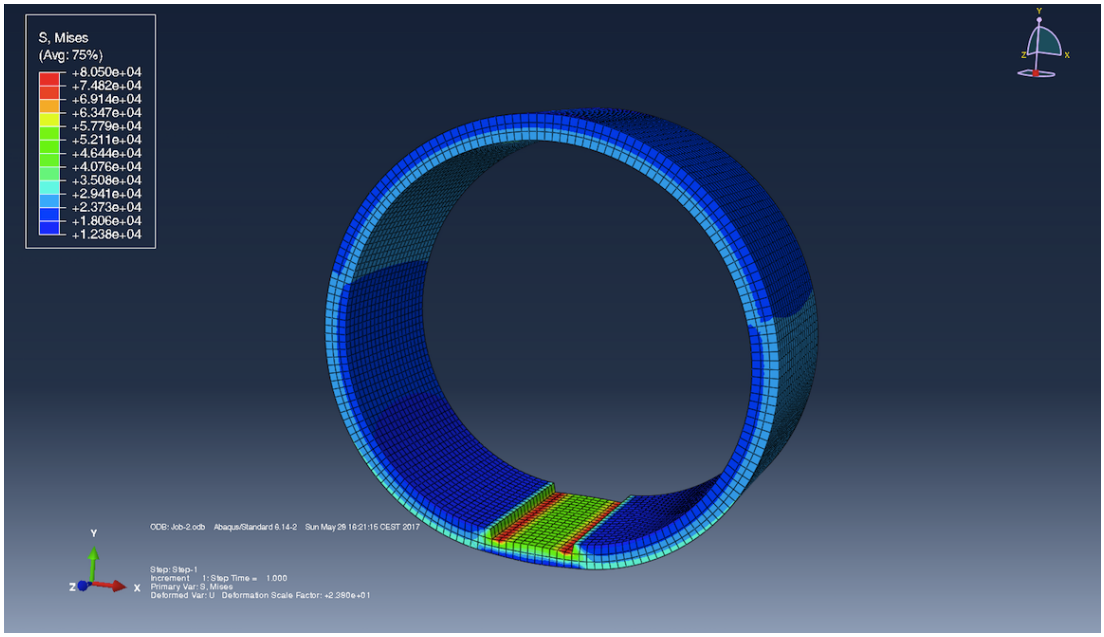

Figure 42: Simulated model with 25% wear and a internal pressure of 3600 psi

5.1.6.2 Rectangular Shaped Wear - 47% Wear Model

The result from the simulation of the 47% wear model shows the internal load to be equal to 2292 psi to onset the yielding of the tubing material. This means a reduction of approximately 76% compared to the reference model with no wear. In table 22 the simulated data for the 47% wear model is given.

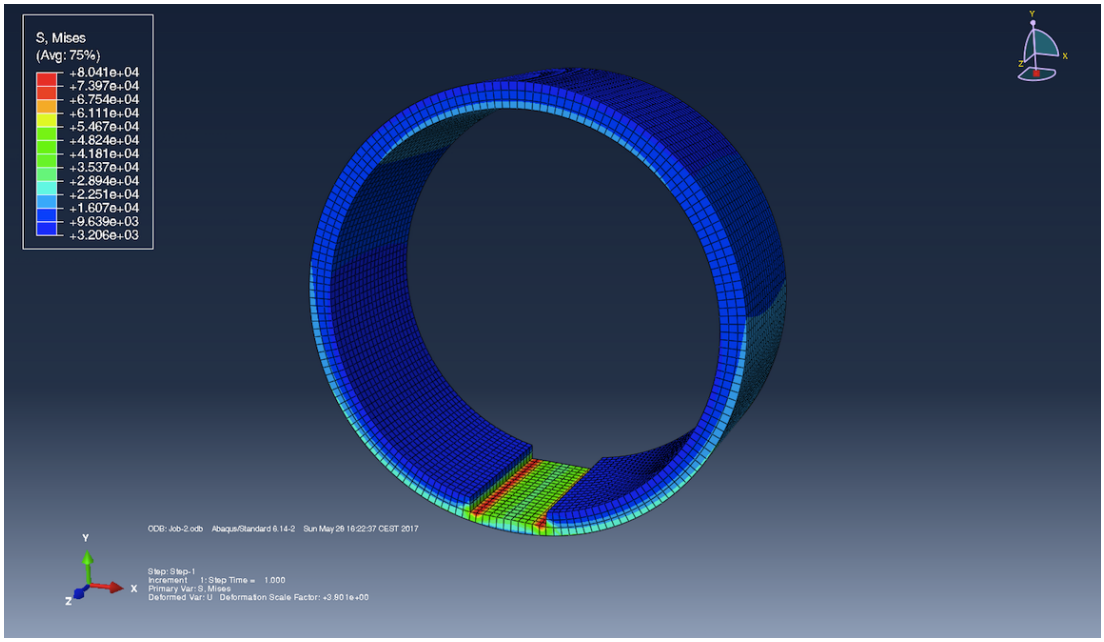

Figure 43: Simulated model with 47% wear and a internal pressure of 2300 psi

Table 22: Internal Pressure and Von Mises Stress for model with 47% wear

Internal Pressure [psi]	Von Mises Stress [psi]
2300	80410
2292	**80000**
2200	75820
2100	70150

5.1.6.3 Rectangular Shaped Wear - Final Results - Burst

Figure 44 shows that the burst pressure reduces significantly when the wear depth increases. The pressure that causes a Von Mises stress equal to σ_y (80000 psi) is calculated by linear interpolation. According to the simulations, at 5% wear

depth, the burst pressure is reduced by 40%. A rectangular shaped wear seems to be decreasing the material strength drastically, even for shallow wear depths.

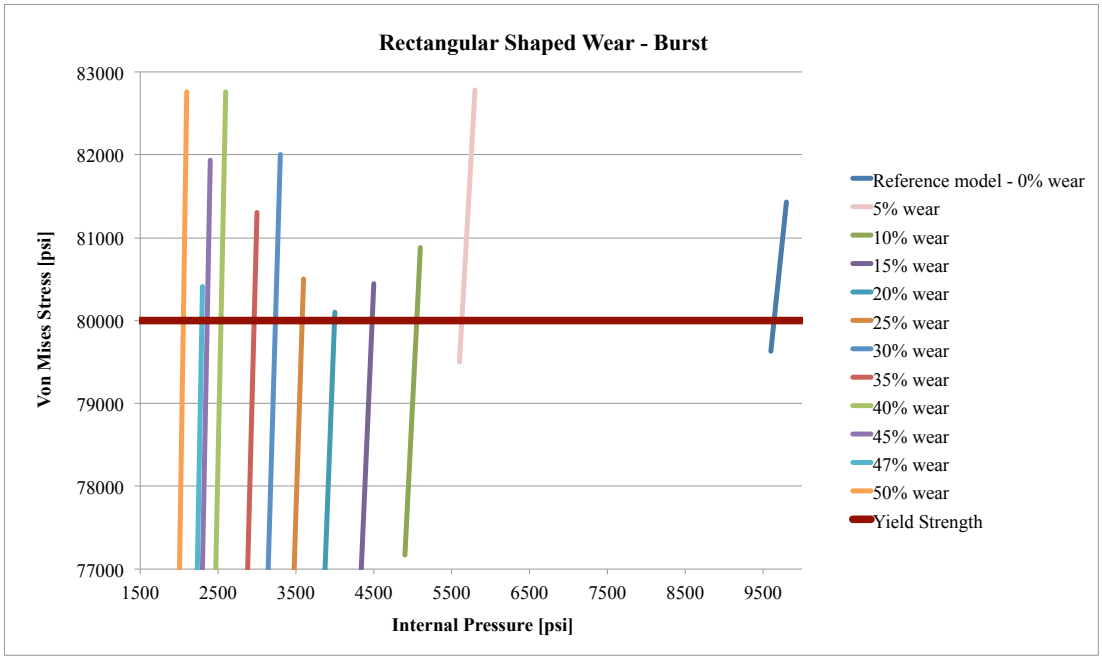

Figure 44: Internal pressure and the respective Von Mises Stress for different wear depths

Table 23: Result from linear interpolation for burst

Burst Pressure [psi]	Wear %
9641	0
5631	5
5052	10
4479	15
3996	20
3582	25
3238	30
2964	35
2538	40
2361	45
2292	47
2054	50

The safe and the failure zones for the operating pressure is shown in figure 45. The area over the curve represent failure zone and the area under represent safe zone. In the figure there is also a generated simulation curve and model for burst pressure. However, for the rectangular shaped wear the original curve is not as smooth as for the other wear types and has a significant slope from 0% wear to 5% wear. Thus, to make a smooth curve a quartic model is generated.

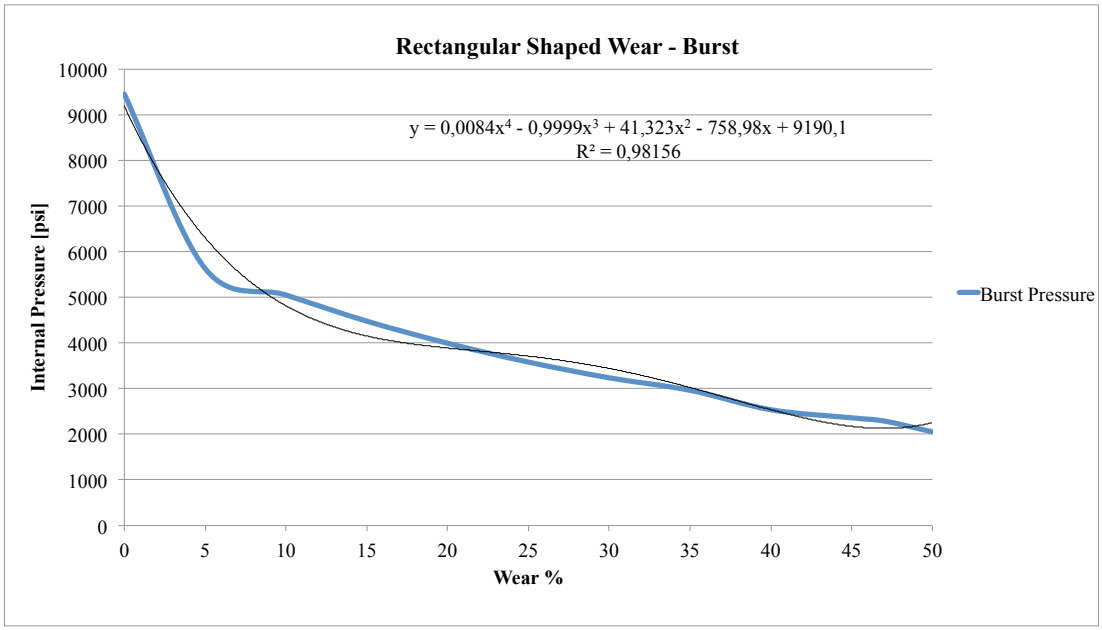

Figure 45: Safe and failure zone for operating internal pressure

Simulated model for burst pressure generated from the curve in figure 45:

$$P_{int} = 0,0084 \times WEAR\%^4 - 0,9999 \times WEAR\%^3 + 41,323 \times WEAR\%^2 - 758,98 \times WEAR\% + 9190,1 \quad (64)$$

The coefficient of determination value, R^2, is equal to 0,98156, thus the simulated data is fitting the statistical model well. The model is illustrated in figure 46, both with and without a design factor. A design factor of 0,84 has been included to match the Barlow's model for burst pressure for a tubing with no wear.

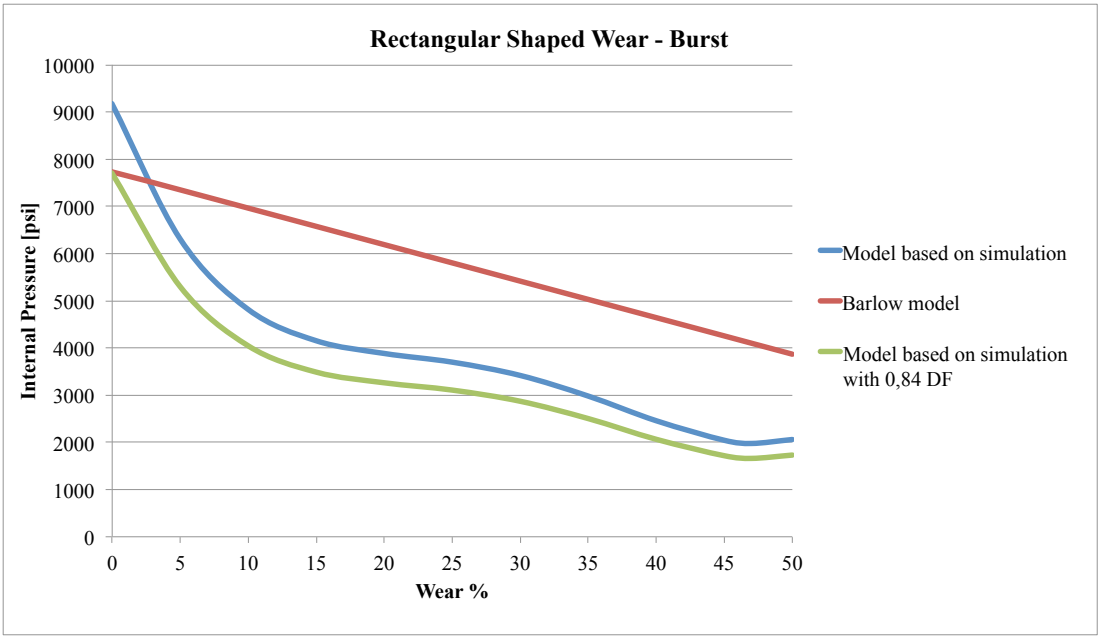

Figure 46: Barlow's model compared with the models based on simulation

The linear Barlow's model for uniform wear allows a safe operational window that is much larger than the non-linear simulated rectangular model, as also observed in the previous sections.

Table 24: Data from the curves in figure 44

Wear %	Simulated results [psi]	Simulated model [psi]	Simulated model with 0,82 DF [psi]	Barlow's model [psi]
0	9641	9190	7720	7738
5	5631	6309	5299	7351
10	5052	4817	4046	6964
15	4479	4154	3489	6577
20	3396	3885	3263	6191
25	3582	3700	3108	5804
30	3238	3418	2871	5417
35	2964	2981	2504	5030
40	2538	2458	2065	4643
45	2361	2044	1717	4256
47	2292	1977	1661	4101
50	2054	2061	1731	3869

5.1.7 Comparing Wear Shapes

In the previous section the different local wear shapes were compared to the Barlow's model. A narrower operational window was observed for all three wear shapes. Figure 47 presents the generated models for the different wear shapes. The effect that the different local wear shapes have on the internal pressure limit for wear depths up to 50% is illustrated.

According to the simulation-based models, the rectangular wear shape has the greatest impact on the burst pressure (see figure 47). The simulations implies that as long as a rectangular shaped wear is present, the pressure limit reduction is rapid up to 5% wear depth, from here the reduction slows down. The wedge shaped wear is the second most critical and the crescent wear shape is the lesser critical. For all wear shapes the Barlow's equation over-predicts the burst pressure limit drastically.

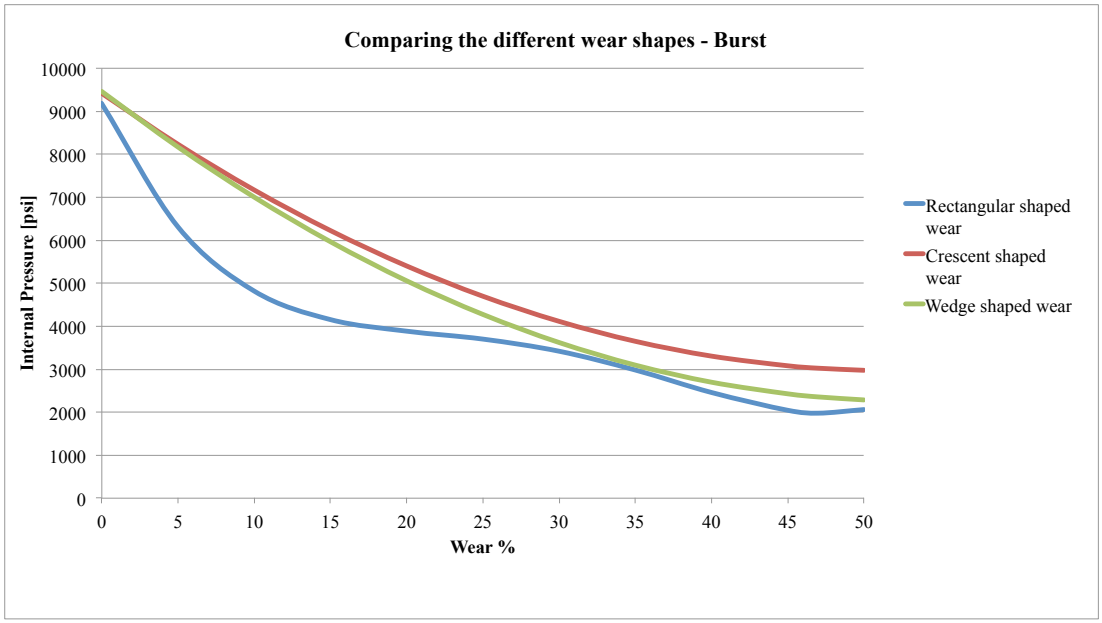

Figure 47: Comparison of burst pressure limit for the different wear shapes

5.2 Collapse Modeling: Single Scar

In this section the simulated results for collapse is presented. There are several events that can cause external pressures in a well. Some examples are gas lift operations, due to the additional pressure from the pump, hydrostatic column of completion fluid in the annulus or tubing leaks. To investigate if the theoretical API collapse equations can be used for local wears, a simulation based model will be created for each wear and compared to the theoretical equations.

Table 25: Collapse Scenario Data

Collapse Scenario	
Well fluid gradient	0,3 psi/ft
Depth of maxium wear (47%)	1626 ft. TVD
Tubing material	L80
Yield Strength	80000 psi

The Ekofisk Field uses gas lift to lower the density of the producing fluids to maintain a desired production rate. Gas is injected in the A-annulus and enters the tubing above the production packer [2]. When pumping the gas down the annulus the external pressure increases dramatically. In worst case scenario this can cause problems related to collapse.

During the simulations the internal pressure is assumed to be hydrostatic since there are no flow in the well due to the low reservoir pressure. Thus, the internal pressure in the well is calculated by the hydrostatic column of oil above the point of interest (1626 ft. TVD):

$$P_{int} = 0,3 psi/ft \times 1626 ft = 488 psi \tag{65}$$

The internal pressure of 488 psi is kept constant during all collapse scenarios.

5.2.1 Collapse Scenario

The upcoming sections presents the results from the simulations of the different types of wear shapes and how they affect the collapse resistance of the tubing.

5.2.2 Reference Model - 0% wear

According to the simulated results from Abaqus, the reference model with no wear can withstand a external pressure of maximum 8900 psi before the material yields. Figure 48 shows the unworn reference model with the applied external pressure of 9000 psi.

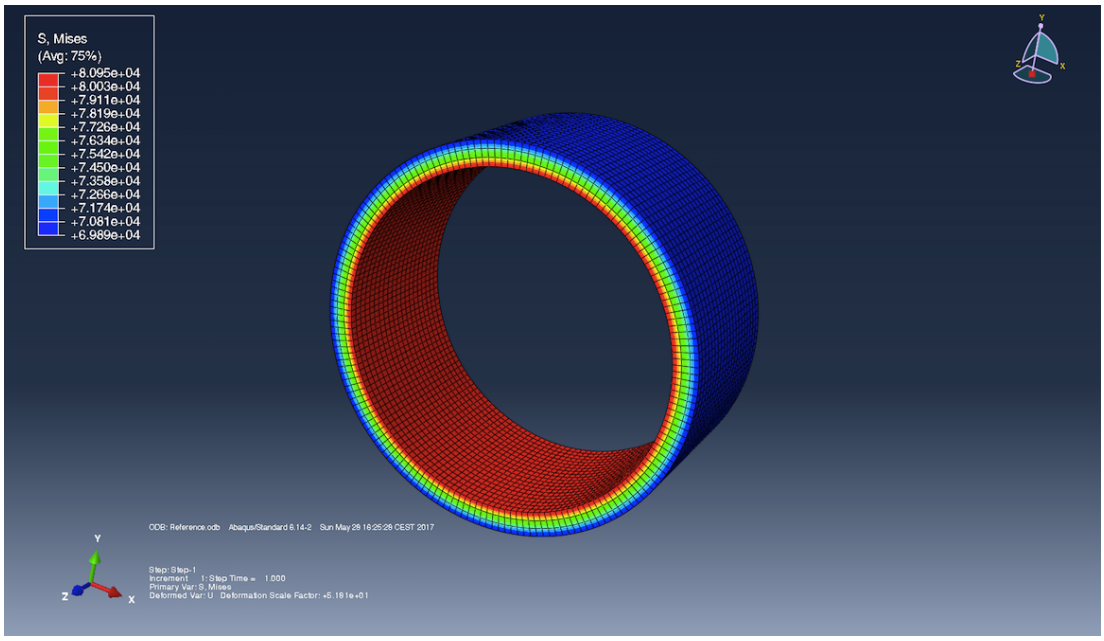

Figure 48: Simulated unworn reference model with a external pressure of 9000 psi

Table 26: Simulated Collapse Pressures and Von Mises Stress for the unworn Reference Model

External Pressure [psi]	Von Mises Stress [psi]
9000	80950
8900	**80000**
8800	79050

5.2.3 Crescent Shaped Wear

The following sections presents the simulated collapse results for a single crescent shaped wear.

5.2.3.1 Crescent Shaped Wear - 25% Wear Model

For a crescent shaped wear of 25% the tubing started to yield to an external pressure between 4300 and 4400 psi. A reduction of approximately 51% compared to the reference model with no wear. Figure 49 shows the tubing under an external loading of 4400 psi. Table 27 shows the simulated data for this model.

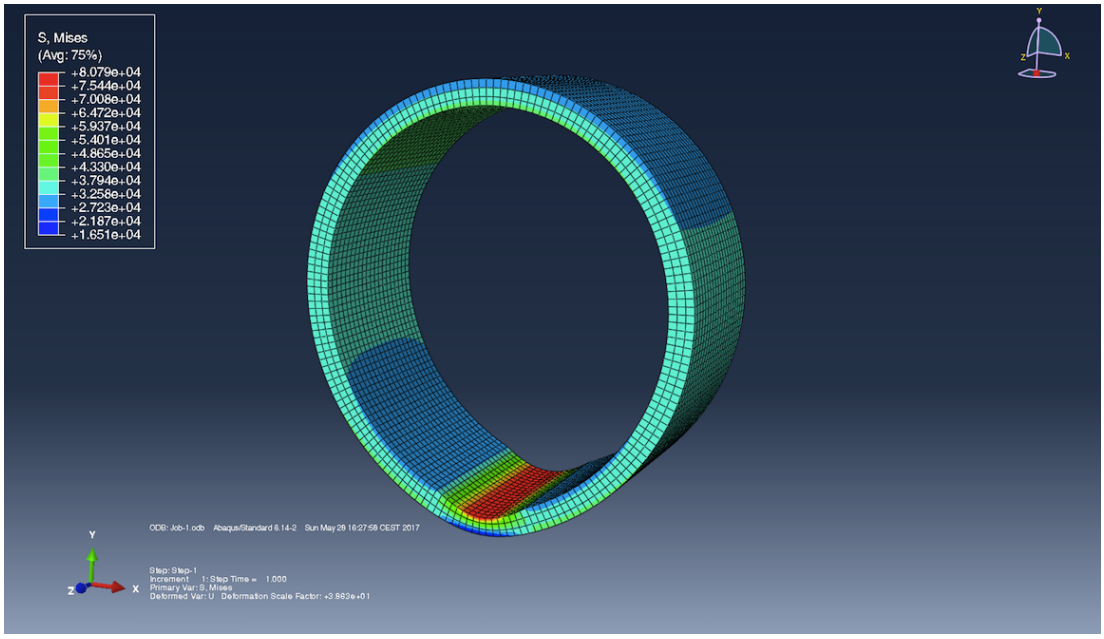

Figure 49: Simulated model with 25% wear depth and a external pressure of 4400 psi

Table 27: External Pressure and Von Mises Stress for model with 25% wear

External Pressure [psi]	Von Mises Stress [psi]
4400	80790
4361	**80000**
4300	78730
4200	76670

5.2.3.2 Crescent Shaped Wear - 47% Wear Model

For a crescent shaped wear of 47%, the maximum external pressure to onset the yielding of the tubing material was calculated to be 2706 psi. Table 28 shows the simulated data for this model.

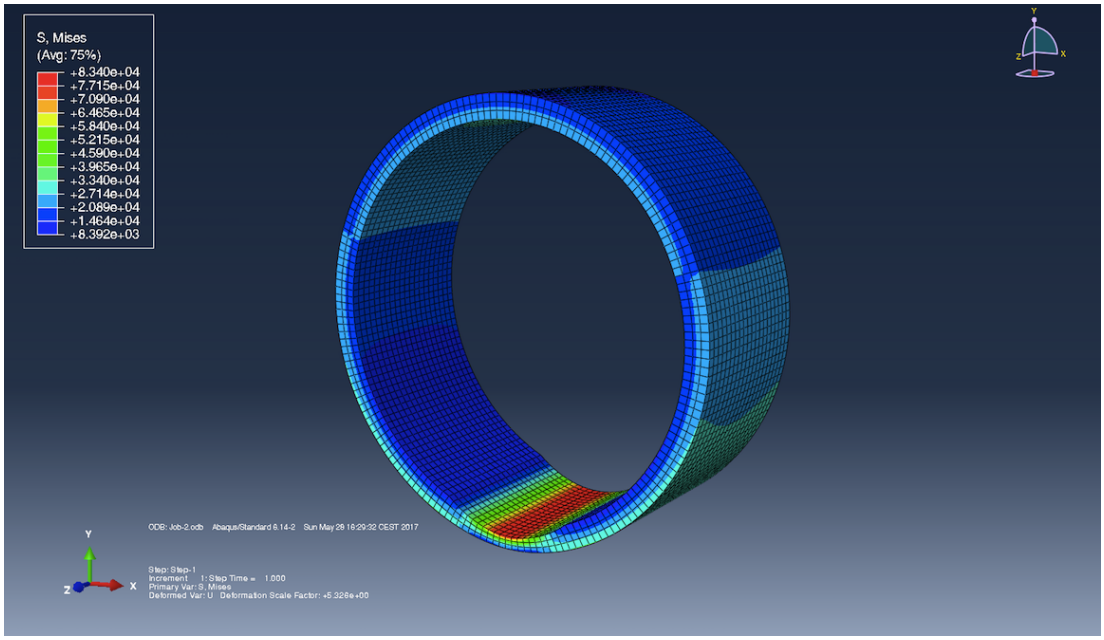

Figure 50: Simulated model with 47% wear depth and a external pressure of 2800 psi

Table 28: External Pressure and Von Mises Stress for model with 47% wear

External Pressure [psi]	Von Mises Stress [psi]
2800	83400
2706	**80000**
2700	79800
2600	76210

5.2.3.3 Crescent Shaped Wear - Final Results - Collapse

As expected, for increased wear depths the collapse resistance of the tubing decreases (see figure 51).

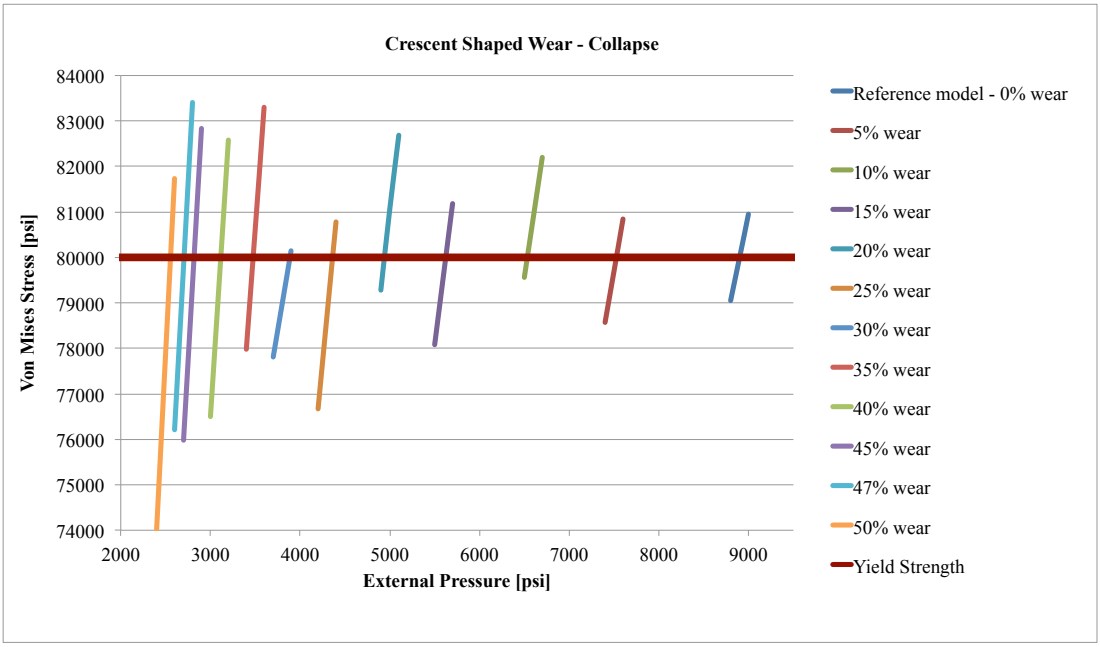

Figure 51: External pressure and the respective Von Mises Stress for different wear depths

Table 29: Result from linear interpolation for collapse

External Pressure [psi]	Wear %
8900	0
7526	5
6533	10
5624	15
4940	20
4361	25
3887	30
3470	35
3116	40
2817	45
2706	47
2555	50

Figure 52 presents the simulated results for the collapse scenario, including a generated model. R^2 is equal to 0,99726 meaning that the correlation between the generated model and the simulated data is satisfying.

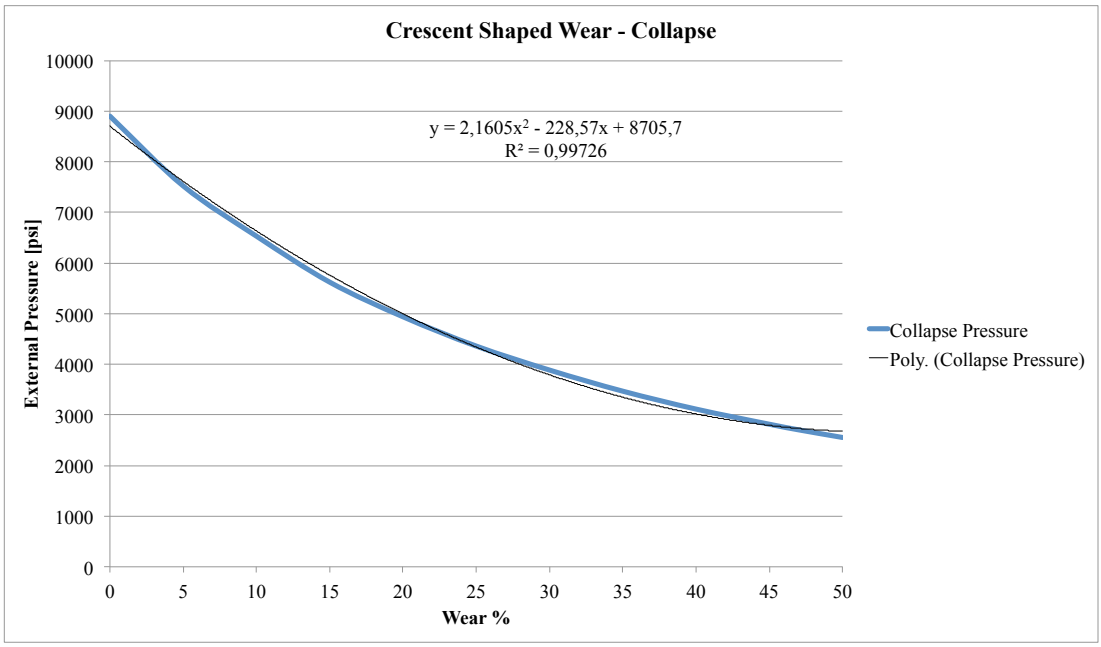

Figure 52: Safe and failure zone for operating external pressure

Generated model from the simulation:

$$P_{ext} = 2,1605 \times WEAR\%^2 - 228,57 \times WEAR\% + 8705,7 \tag{66}$$

In order to match the API collapse models for an unworn tubing a design factor of 0,72 is applied to the simulation-based model. In this case the theoretical API collapse curve is based on a uniform wall thickness. However, as the thickness reduces, the slenderness ratio (D/t) also varies causing the collapse mode to change. The theoretical collapse curve in figure 53 is created based on three different collapse modes, plastic, transitional and elastic.

The simulated based model is compared with the theoretical collapse models (API models) for uniform wear. Figure 53 illustrates that from 0% wear to 30% wear, the simulated based model with a design factor of 0,72 overlaps the theoretical collapse curve very well. From 30% to 50% the theoretical collapse curve seems to have the lowest collapse resistance.

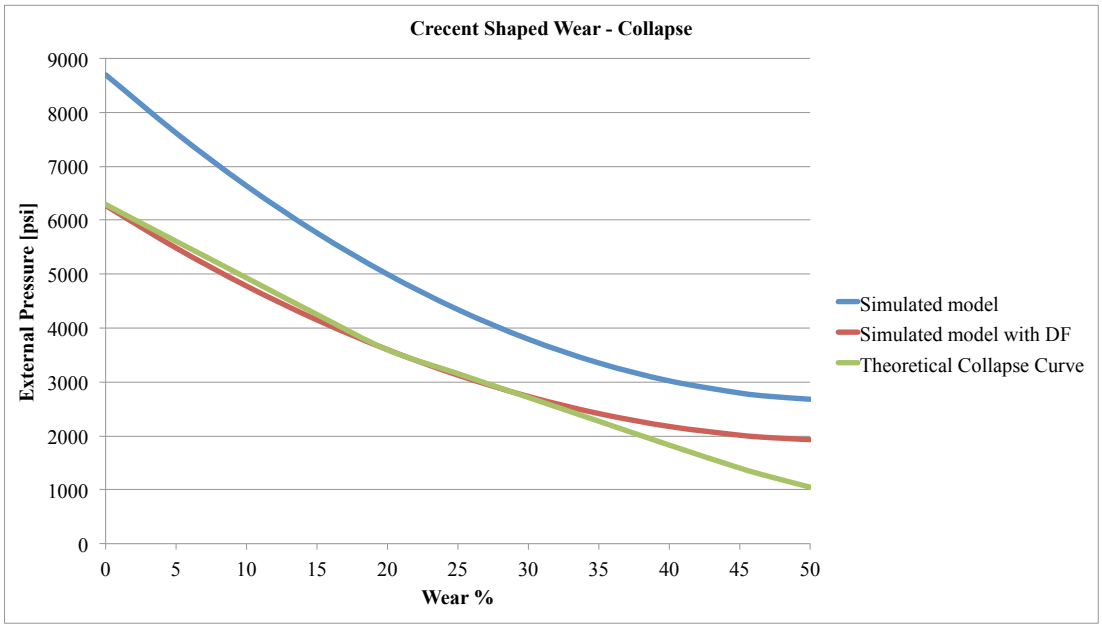

Figure 53: Simulated based models compared with the theoretical collapse models for uniform thickness

Table 30: Data from figure 53

Wear%	Simulated model	Simulated model with DF 0,72	D/t ratio	Collapse mode	Theoretical Collapse
0	8706	6268	18.09	Plastic	6288
5	7617	5484	19.04	Plastic	5609
10	6636	4778	20.10	Plastic	4930
15	5763	4150	21.28	Plastic	4251
20	4999	3599	22.62	Trans. Collapse	3596
25	4342	3126	24.12	Trans. Collapse	3154
30	3793	2731	25.85	Trans. Collapse	2712
35	3352	2414	27.83	Trans. Collapse	2271
40	3020	2174	30.15	Trans. Collapse	1829
45	2795	2012	32.89	Elastic	1403
47	2735	1970	34.14	Elastic	1253
50	2678	1928	36.18	Elastic	1048

5.2.4 Wedge Shaped Wear

The following sections presents the simulated collapse results for a single wedge shaped wear.

5.2.4.1 Wedge Shaped Wear - 25% Wear Model

According to the simulation a wedge shaped wear of 25% the maximum external pressure to onset the yielding of the material is 3963 psi. Table 31 shows the data for the 25% wear model.

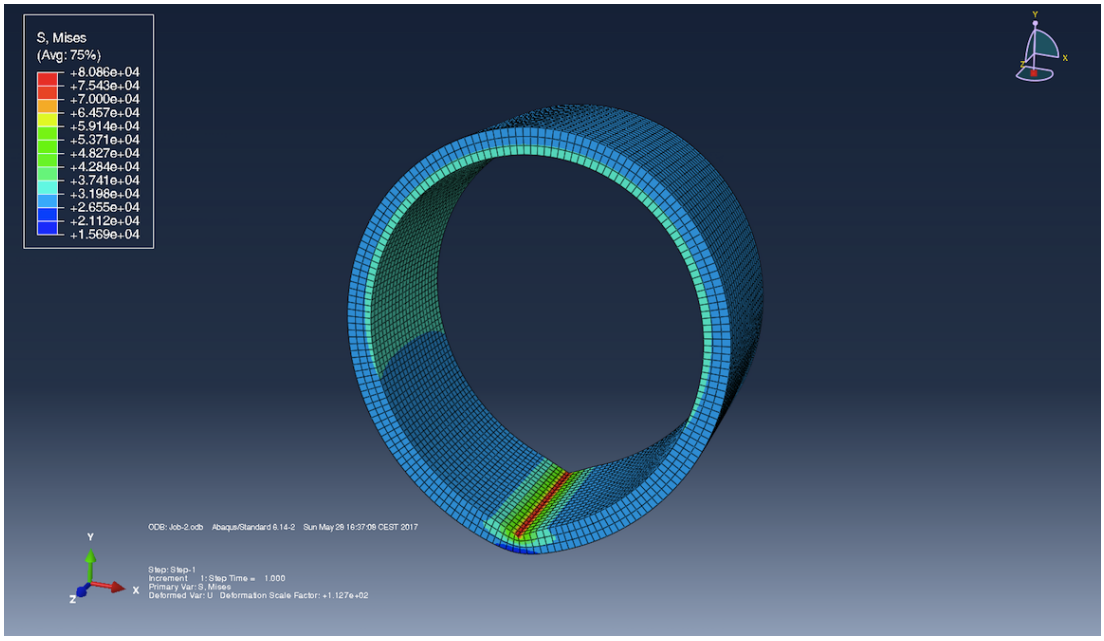

Figure 54: Simulated model with 25% wear depth and a external pressure of 4000 psi

Table 31: External Pressure and Von Mises Stress for model with 25% wear

External Pressure [psi]	Von Mises Stress [psi]
4000	80860
3963	**80000**
3900	78560
3800	76270

5.2.4.2 Wedge Shaped Wear - 47% Wear Model

Simulation shows that for the 47% wear model the maximum external pressure before yielding occurs is 2050 psi. The data from the 47% model is given in table 32.

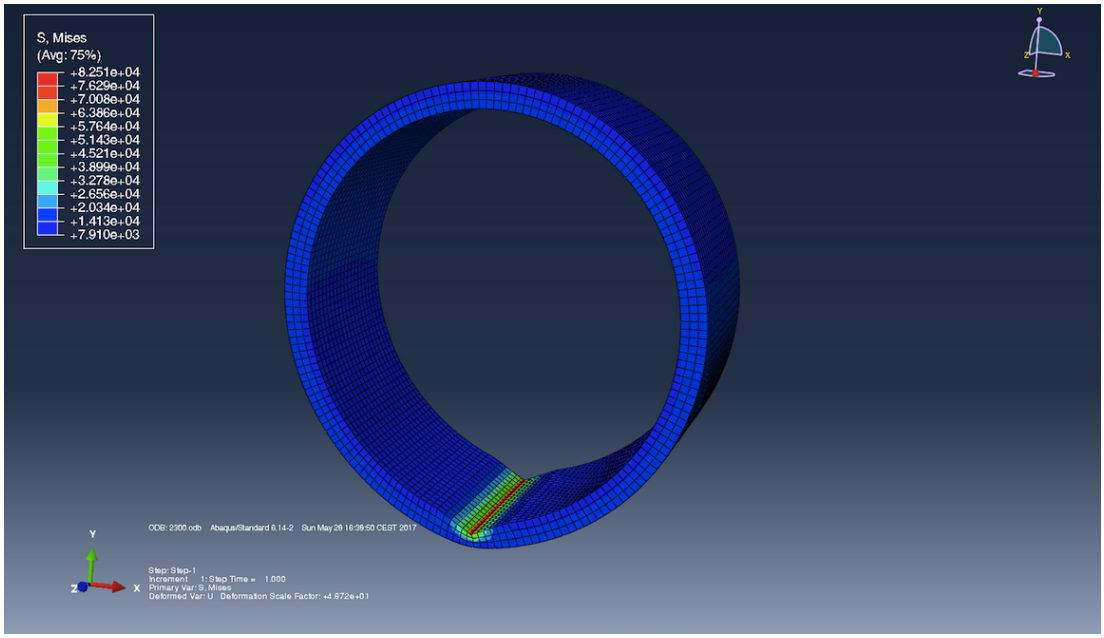

Figure 55: Simulated model with 47% wear depth and a external pressure of 2100 psi

Table 32: External Pressure and Von Mises Stress for model with 47% wear

External Pressure [psi]	Von Mises Stress [psi]
2100	82510
2050	**80000**
2000	77410
1900	72300

5.2.4.3 Wedge Shaped Wear - Final Results - Collapse

Figure 56 shows similarly to the previous simulations that the collapse resistance of the material decreases as the wear depth increases.

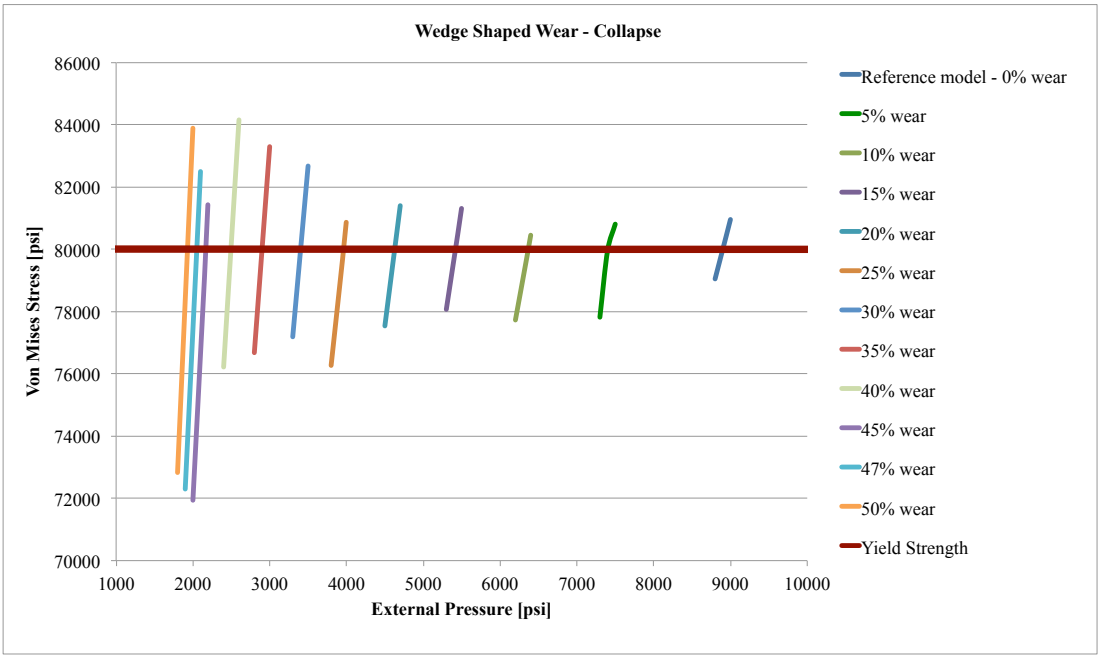

Figure 56: External pressure and the respective Von Mises Stress for different wear depths

Table 33: Result from linear interpolation for collapse

External Pressure [psi]	Wear %
8900	0
7428	5
6367	10
5419	15
4627	20
3963	25
3402	30
2900	35
2495	40
2170	45
2050	47
1929	50

Figure 57 shows a curve for the simulated results and a simulation-based model. R^2 is equal to 0,99851. The area above the curve is not a safe operating pressure while the area under is safe, this is not included a safety factor.

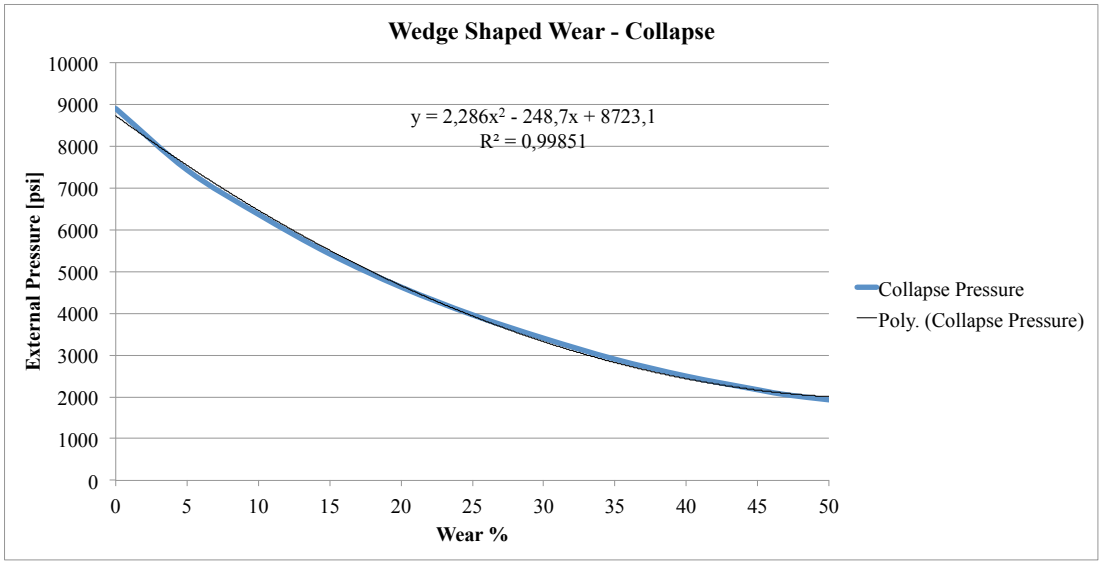

Figure 57: Safe and failure zone for operating external pressure

Generated model from the simulation:

$$P_{ext} = 2,286 \times WEAR\%^2 - 248,7 \times WEAR\% + 8723,1 \tag{67}$$

To match the theoretical collapse curve a design factor of 0,72 is included in the simulation based model. Figure 58 shows a comparison of the theoretical collapse curve and the simulation-based models. In this case the theoretical collapse curve shows a higher collapse resistance up to approximately 42%. From 42% to 50% the simulation based model shows higher collapse resistance.

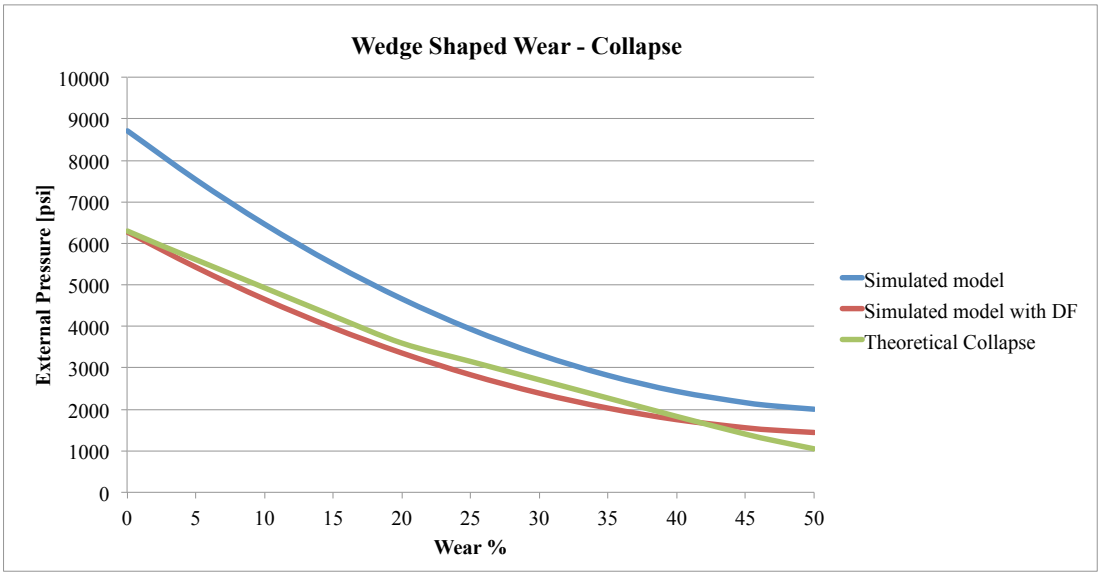

Figure 58: Simulated based models compared with the theoretical collapse models for uniform thickness

Table 34: Data from figure 58

Wear%	Simulated model	Simulated model with DF 0,72	D/t ratio	Collapse mode	Theoretical Collapse
0	8706	6281	18.09	Plastic	6288
5	7537	5426	19.04	Plastic	5609
10	6465	4655	20.10	Plastic	4930
15	5507	3965	21.28	Plastic	4251
20	4664	3358	22.62	Trans. Collapse	3596
25	3934	2833	24.12	Trans. Collapse	3154
30	3320	2390	25.85	Trans. Collapse	2712
35	2810	2030	27.83	Trans. Collapse	2271
40	2433	1752	30.15	Trans. Collapse	1829
45	2161	1556	32.89	Elastic	1403
47	2084	1500	34.14	Elastic	1253
50	2003	1442	36.18	Elastic	1048

5.2.5 Rectangular Shaped Wear

The next sections presents the simulated collapse results for a single rectangular shaped scar.

5.2.5.1 Rectangular Shaped Wear - 25% Wear Model

The 25% wear model with a rectangular shaped wear can withstand a maximum external pressure of 3278 psi according to the simulations. Table 35 shows the data for the model.

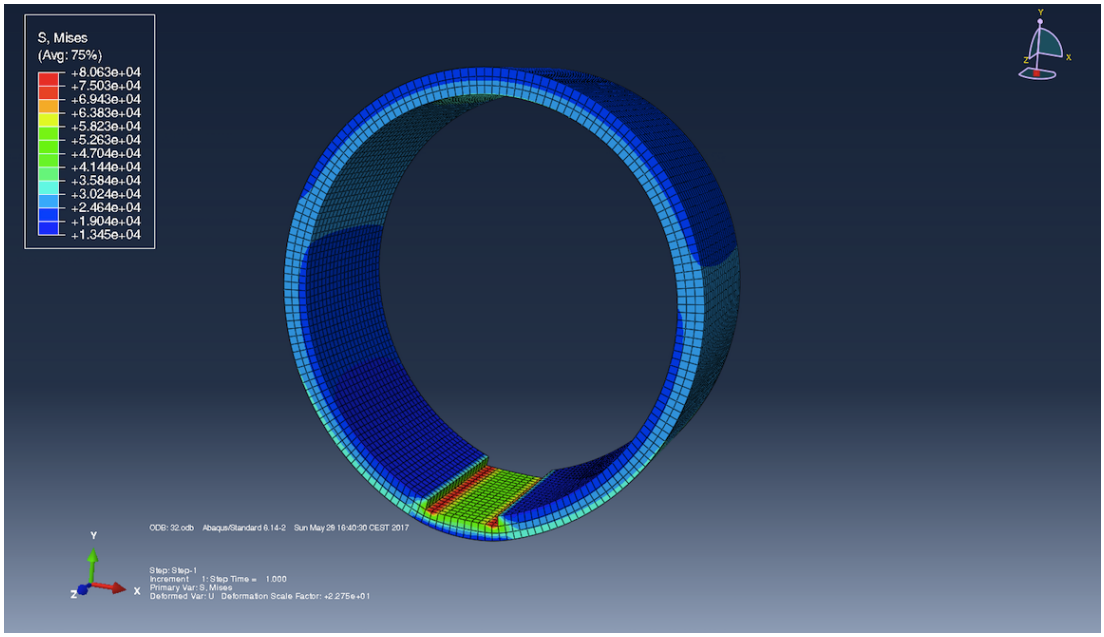

Figure 59: Simulated model with 25% wear depth and a external pressure of 3300 psi

Table 35: External Pressure and Von Mises Stress for model with 25% wear

External Pressure [psi]	Von Mises Stress [psi]
3400	83480
3300	80630
3278	**80000**
3200	77770

5.2.5.2 Rectangular Shaped Wear - 47% Wear Model

For the 47% wear model the maximum external pressure before yielding is simulated to 2031 psi. The data for this model is given in table 36.

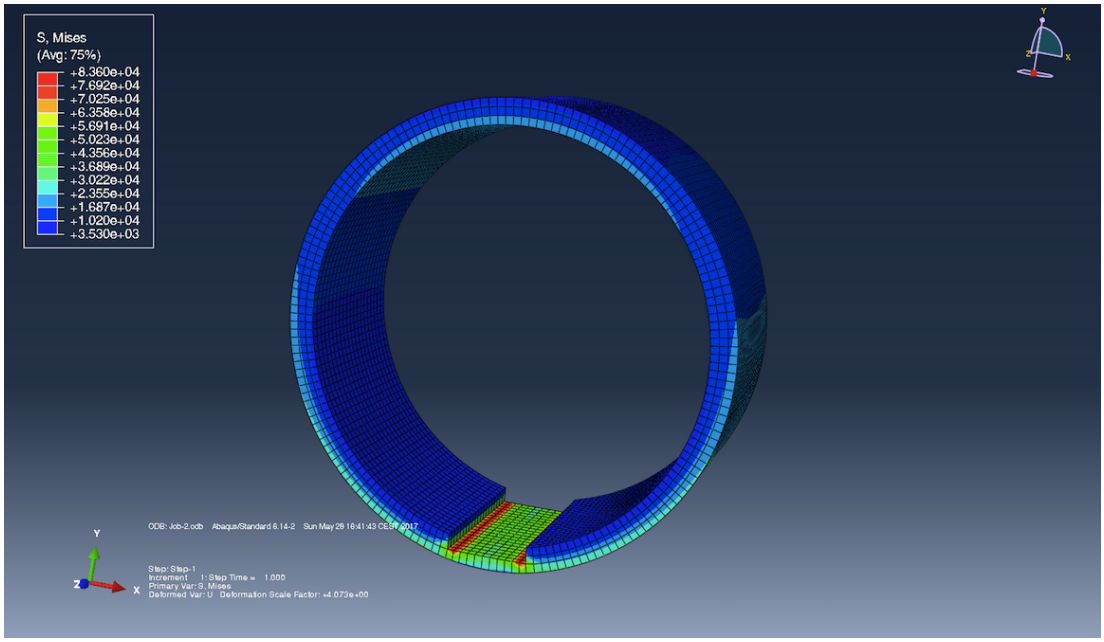

Figure 60: Simulated model with 47% wear depth and a external pressure of 2100 psi

Table 36: External Pressure and Von Mises Stress for model with 47% wear

External Pressure [psi]	Von Mises Stress [psi]
2100	83600
2031	**80000**
2000	78420
1900	73250

5.2.5.3 Rectangular Shaped Wear - Final Results - Collapse

Figure 61 shows external pressure and the respective Von Mises stress for the different wear depths. The trend is the same as for the previous wear shapes, with an increased wear depth there is an decrease in the collapse resistance of the material.

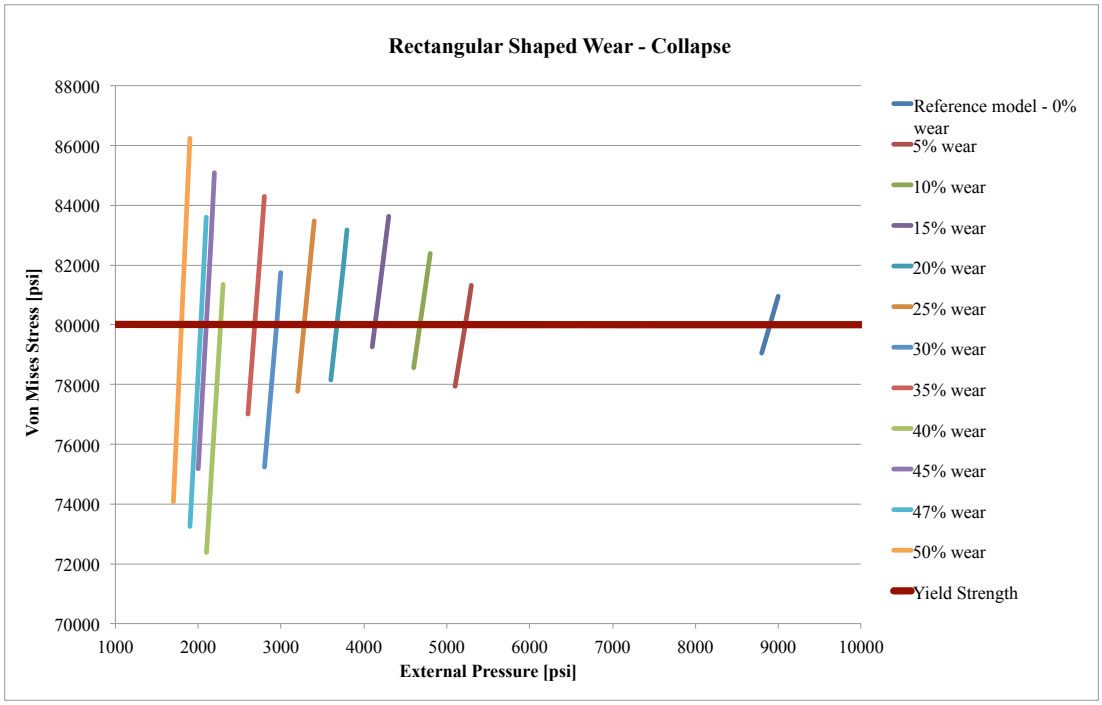

Figure 61: External pressure and the respective Von Mises Stress for different wear depths

Table 37: Result from linear interpolation for collapse

External Pressure [psi]	Wear %
8900	0
5222	5
4676	10
4134	15
3674	20
3278	25
2947	30
2682	35
2270	40
2097	45
2031	47
1797	50

In figure 62 the simulated results curve and a simulation based model curve is illustrated. A rapid decrease in the collapse resistance is observed up to 5% wear depth.

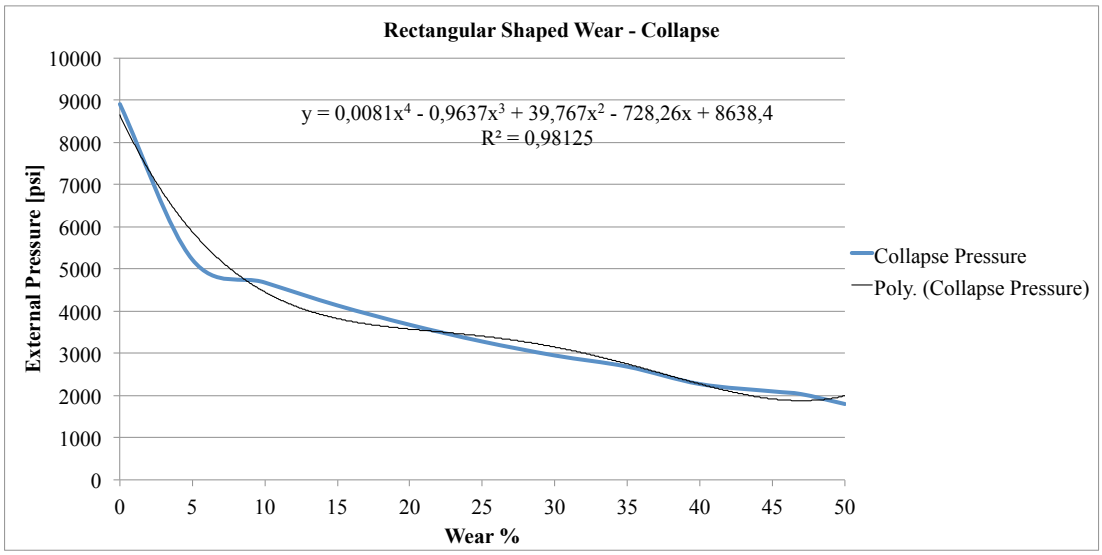

Figure 62: Safe and failure zone for operating external pressure

Due to the irregular shape of the curve a quatric model needs to be generated to have a good correlation between the simulated results and the generated model.

Generated model based on the simulation results:

$$P_{ext} = 0,0081 \times WEAR\%^4 - 0,9637 \times WEAR\%^3 + 39,767 \times WEAR\%^2 - 728,26 \times WEAR\% + 8638,4 \quad (68)$$

In order to match the theoretical collapse curve in this case a design factor of 0,73 is included in the simulation based model. This is illustrated in figure 63. The simulation based model shows a lower collapse resistance up to approximately 47%, from 47% to 50% the API collapse models have the lowest collapse resistance.

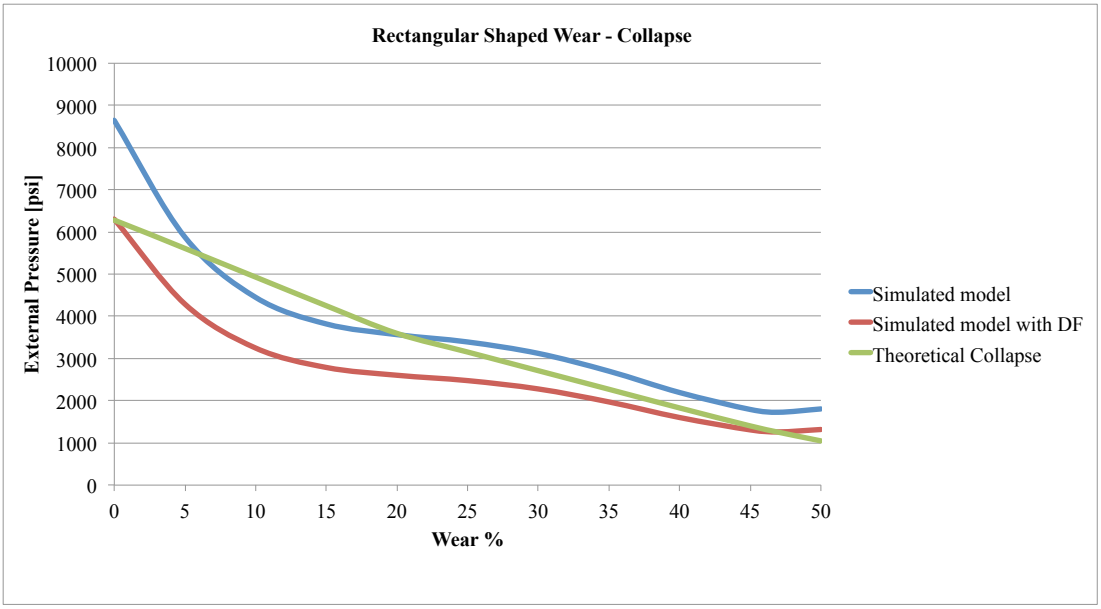

Figure 63: Simulated based models compared with the theoretical collapse models for a uniform thickness

Table 38: Data from figure 63

Wear%	Simulated model	Simulated model with DF 0,72	D/t ratio	Collapse mode	Theoretical Collapse
0	8638	6306	18.09	Plastic	6288
5	5876	4289	19.04	Plastic	5609
10	4450	3248	20.10	Plastic	4930
15	3820	2788	21.28	Plastic	4251
20	3566	2603	22.62	Trans. Collapse	3596
25	3393	2477	24.12	Trans. Collapse	3154
30	3122	2279	25.85	Trans. Collapse	2712
35	2700	1971	27.83	Trans. Collapse	2271
40	2194	1602	30.15	Trans. Collapse	1829
45	1793	1309	32.89	Elastic	1403
47	1727	1260	34.14	Elastic	1253
50	1805	1318	36.18	Elastic	1048

5.2.6 Comparing Wear Shapes

In this section the simulation-based models for the different local wear shapes is compared. Figure 64 shows the external pressure that causes the material to yield for the different wear depths.

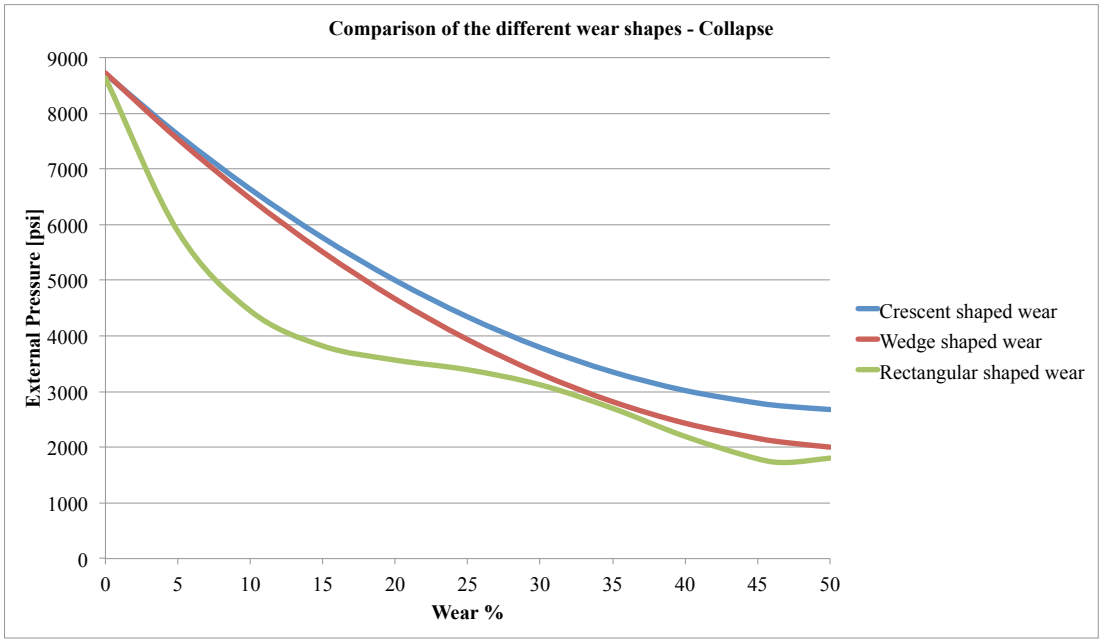

Figure 64: Comparison of collapse resistance limit for the different wear shapes

Similarly to the burst scenario the rectangular wear shape is the most critical. Followed by the wedge shaped wear. The crescent wear shape has the highest collapse rating.

5.3 Burst Modeling: Two Scars

Well intervention often includes tripping in and out of a well multiple times. During the intervention various types of tools and equipment may be used. Tripping into the well may cause compressive forces on the tools, causing a wear that is on the low side of the tubing. Tripping out exert tensile forces, which may contribute to a wear on the upper side of the tubing. When it comes to corrosion or erosion there is also a possibility that the wear occurs on either the topside or the low-side of the tubing. The following results is based on simulations of a tubing with two wear scars.

5.3.1 Crescent Shaped Scars

The next sections presents the simulated burst results for a tubing with two crescent shaped scars.

5.3.1.1 Crescent Shaped Scars - 25% Wear Model

With two crescent shaped scars of 25% wear depth of the wall thickness the material yields under a internal pressure of 4513 psi.

Table 39: Internal Pressure and Von Mises Stress for model with 25% wear

Internal Pressure [psi]	Von Mises Stress [psi]
4600	81840
4513	**80000**
4500	79710
4400	77590

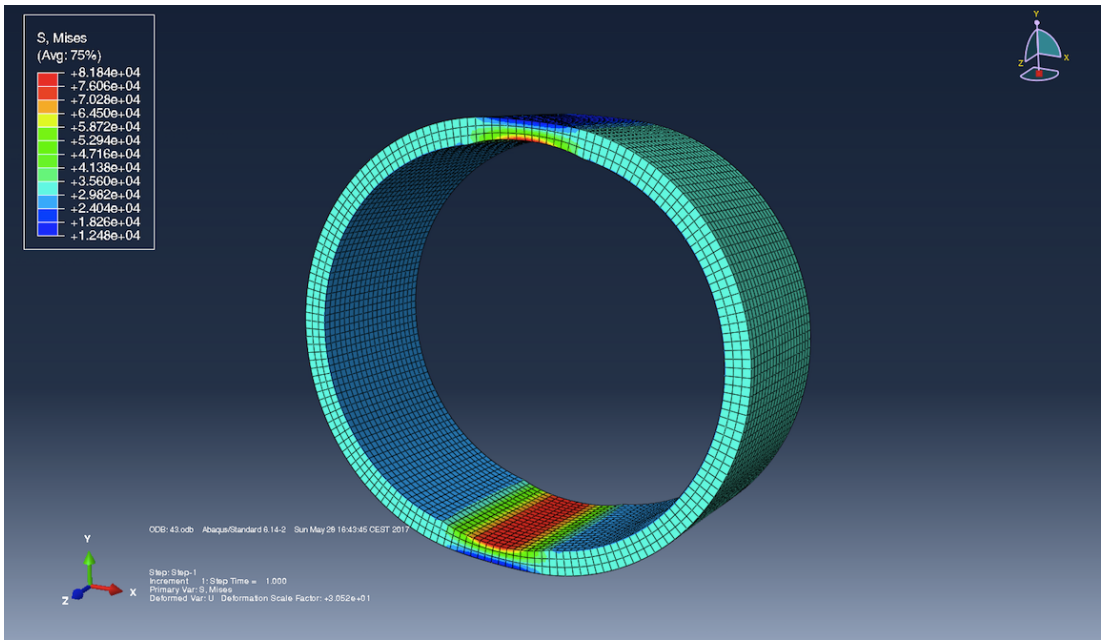

Figure 65: Simulated model with 25% wear and a internal pressure of 4600 psi

5.3.1.2 Crescent Shaped Scars - 47% Wear Model

Simulation shows that for the 47% wear depth model the burst resistance is only 2677 psi.

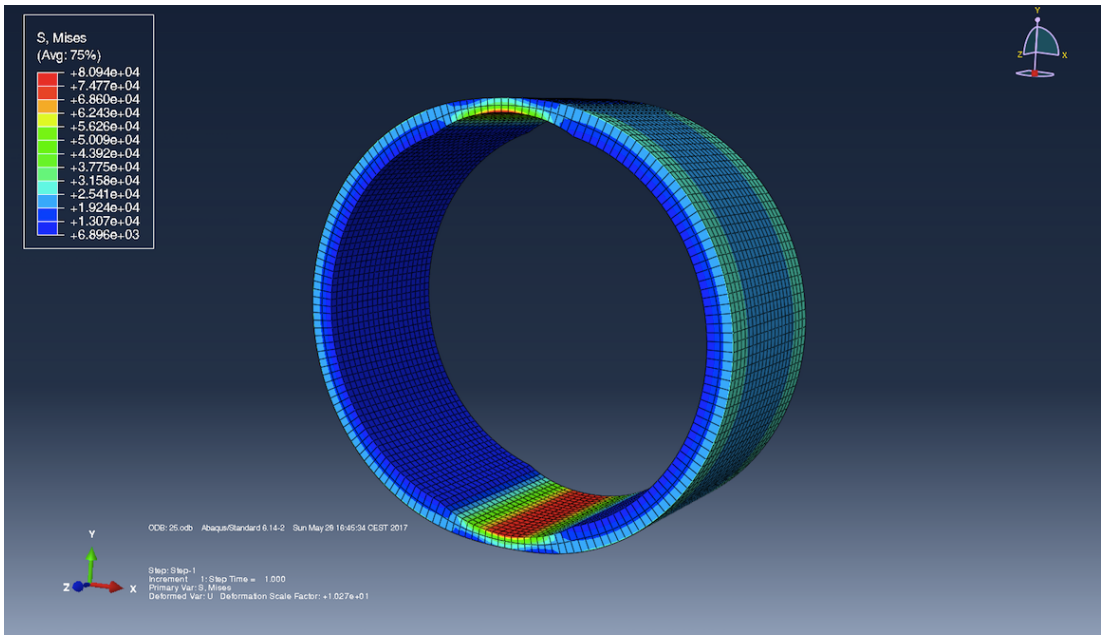

Figure 66: Simulated model with 47% wear and a internal pressure of 2700 psi

Table 40: Internal Pressure and Von Mises Stress for model with 47% wear

Internal Pressure [psi]	Von Mises Stress [psi]
2700	80940
2677	**80000**
2600	76820
2500	72700

5.3.1.3 Two Crescent Shaped Scars - Final Results - Burst

In figure 67 the burst resistance for the tubing with two crescent shaped wears is illustrated. A significant reduction in the burst resistance is observed as the wear depth increases.

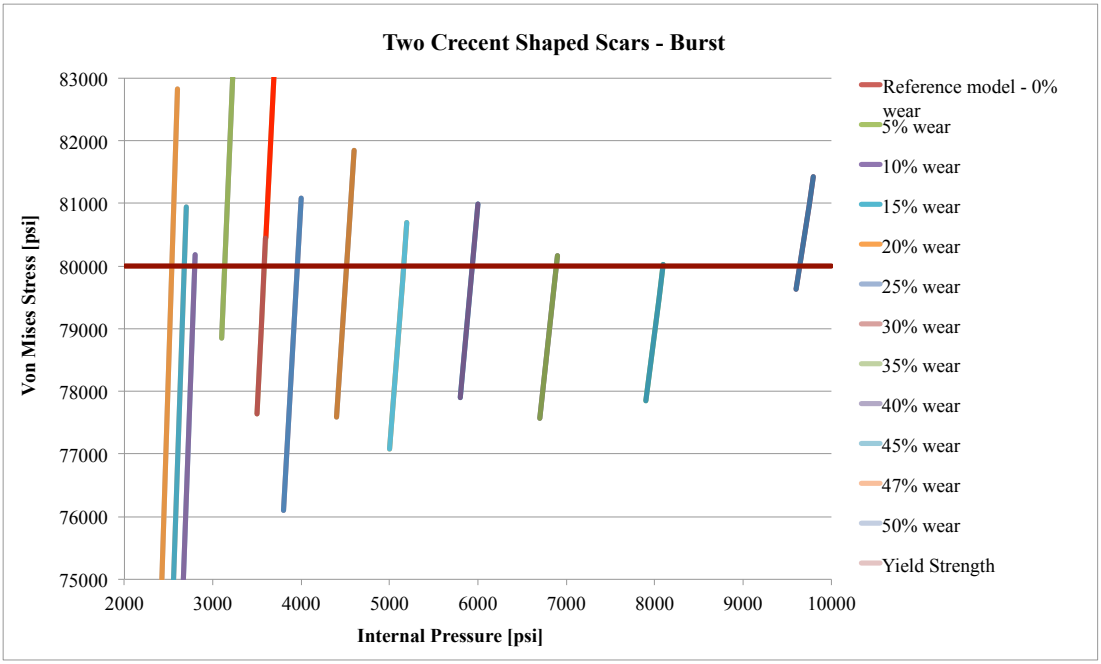

Figure 67: Internal pressure and the respective Von Mises Stress for different wear depths

To find the maximum internal pressure the tubing can handle before yielding occurs linear interpolation is performed (see table 41). This pressure is found at the intersection between linear the pressure slopes for the different wears and the yield strength limit (see figure 67).

Table 41: Result from linear interpolation for burst

Internal Pressure [psi]	Wear %
9641	0
8097	5
6887	10
5936	15
5161	20
4513	25
3957	30
3584	35
3134	40
2795	45
2677	47
2536	50

The data from table 41 is used to generate the curve illustrated in figure 68. The curve for the single scar is also presented. The tubing with two-wear scars show a lower burst resistance from 5% up to 50% compared to the tubing with a single scar. From the two-wear scars curve a model is generated (R = 0,99665).

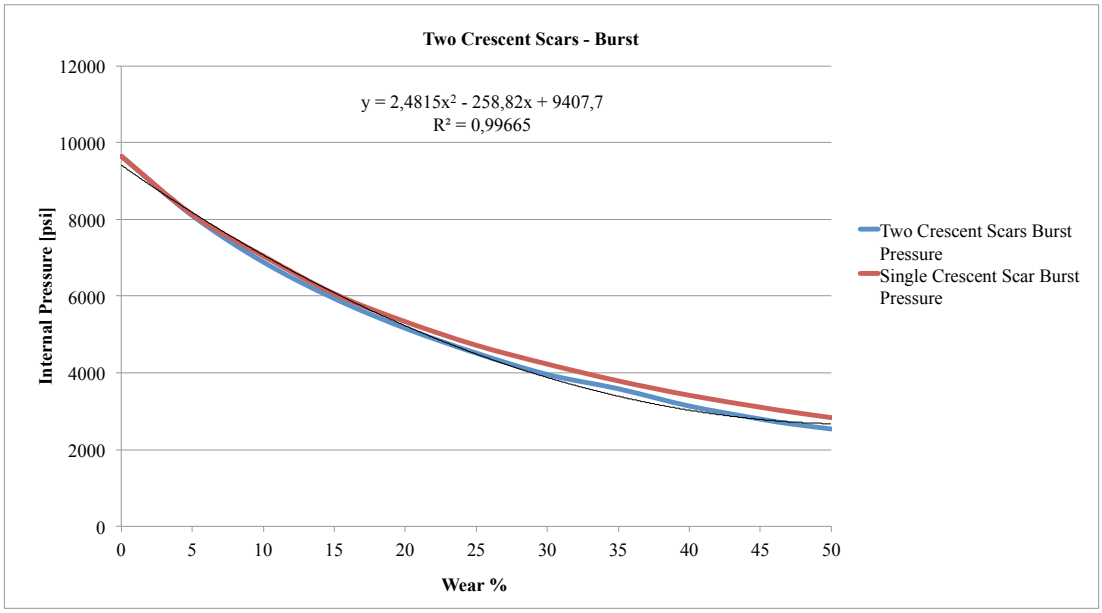

Figure 68: Safe and failure zone for operating internal pressure

Generated model from the curve based on the simulated results:

$$P_{int} = 2,4815 \times WEAR\%^2 - 258,82 \times WEAR\% + 9407,0 \quad (69)$$

5.3.2 Wedge Shaped Scars

The following sections presents the simulated burst results for a tubing with two wedge shaped scars.

5.3.2.1 Wedge Shaped Scars - 25% Wear Model

For the 25% model with two wedge shaped scars the material yields under a internal pressure of 4240 psi.

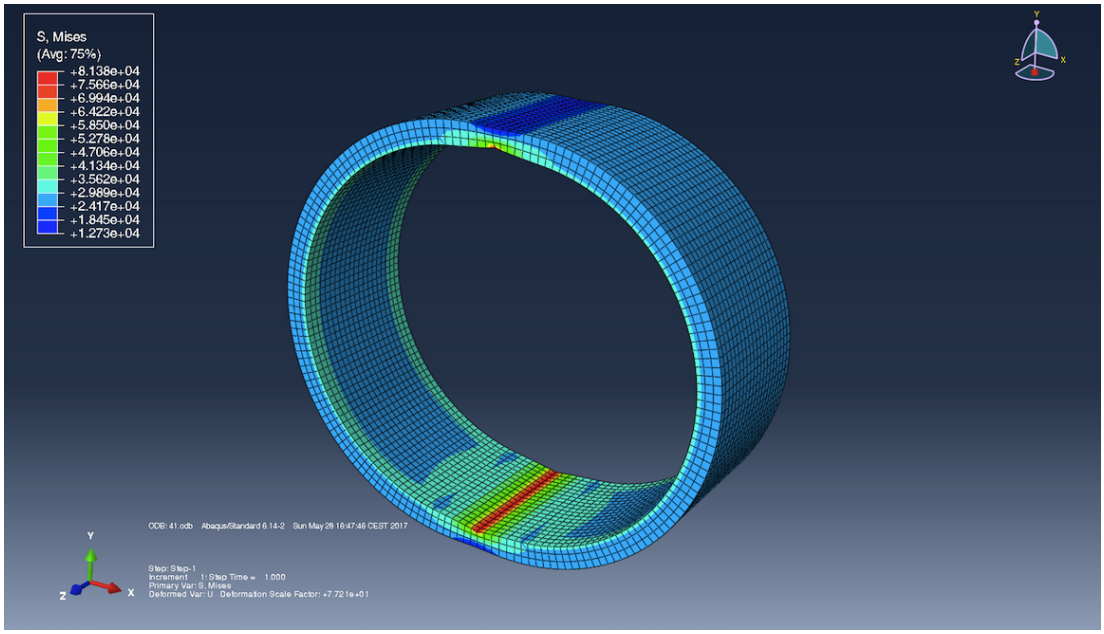

Figure 69: Simulated model with 25% two wear scars and a internal pressure of 4300 psi

Table 42: Internal Pressure and Von Mises Stress for model with 25% wear

Internal Pressure [psi]	Von Mises Stress [psi]
4300	81380
4240	**80000**
4200	79090
4100	76800

5.3.2.2 Wedge Shaped Scars - 47% Wear Model

The model with two wedge shaped scars of 47% wear depth the material yields under a internal pressure of 2251 psi.

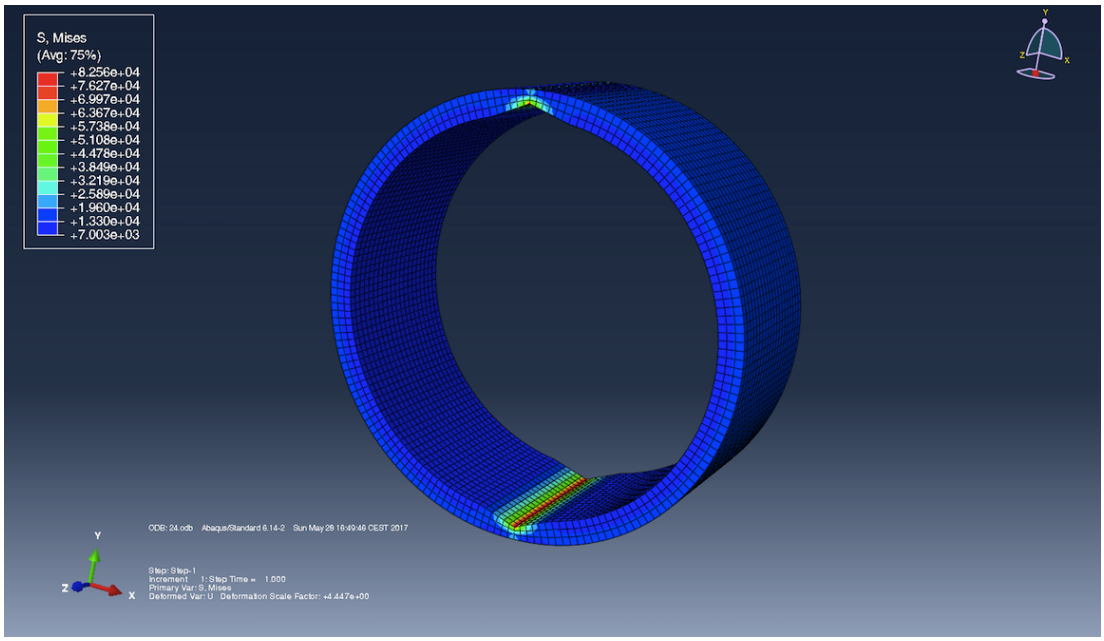

Figure 70: Simulated model with 47% wear scars and a internal pressure of 2300 psi

Table 43: Internal Pressure and Von Mises Stress for model with 47% wear

Internal Pressure [psi]	Von Mises Stress [psi]
2400	87830
2300	82560
2251	**80000**
2200	77290

5.3.2.3 Two Wedge Shaped Scars - Final Results - Burst

Figure 71 illustrates the different burst pressures and the respective Von Mises stress for the tubing with two wedge shaped wears. When the wear depth increases the burst pressure decreases.

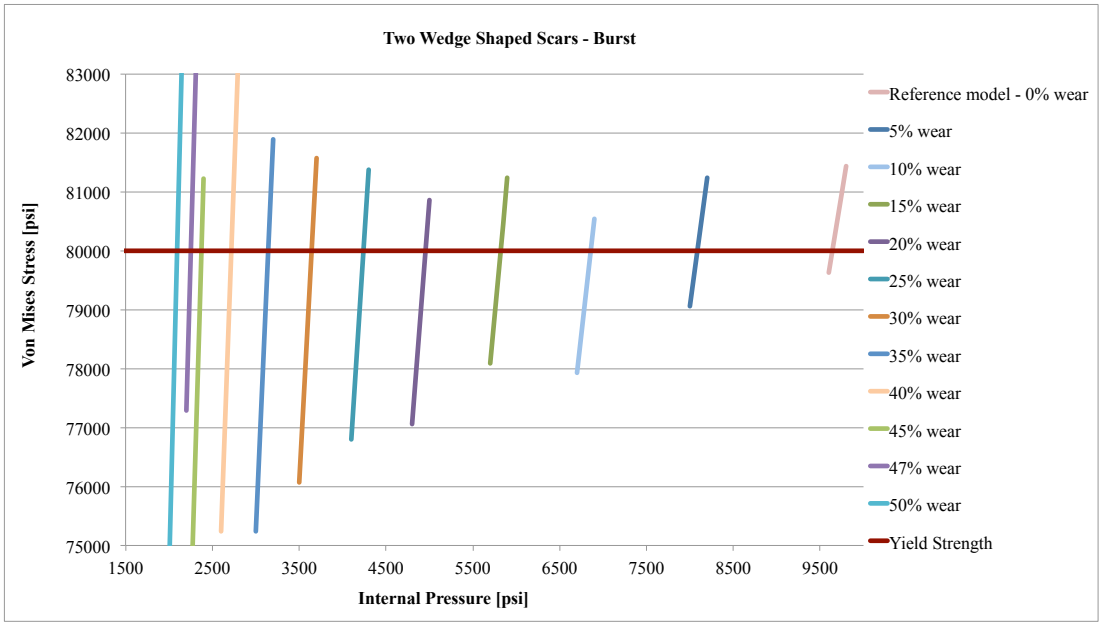

Figure 71: Internal pressure and the respective Von Mises Stress for different wear depths

Linear interpolation is performed to calculate the burst pressure that creates a Von Mises stress equal to the yield stress limit for each wear depth (see table 44).

From the data in table 44 the curve illustrated in figure 72 is generated. The zone above the curve represent the failure zone, and the zone below the curve represents the safe zone. The single wedge shaped wear curve is also illustrated. In this case the single scar curve almost overlap the two scar curve perfectly. A model is generated from the curve based on the simulated results (R = 0,99837).

Generated model from the simulated data curve:

$$P_{int} = 2,5812 \times WEAR\%^2 - 274,15 \times WEAR\% + 9462,9 \quad (70)$$

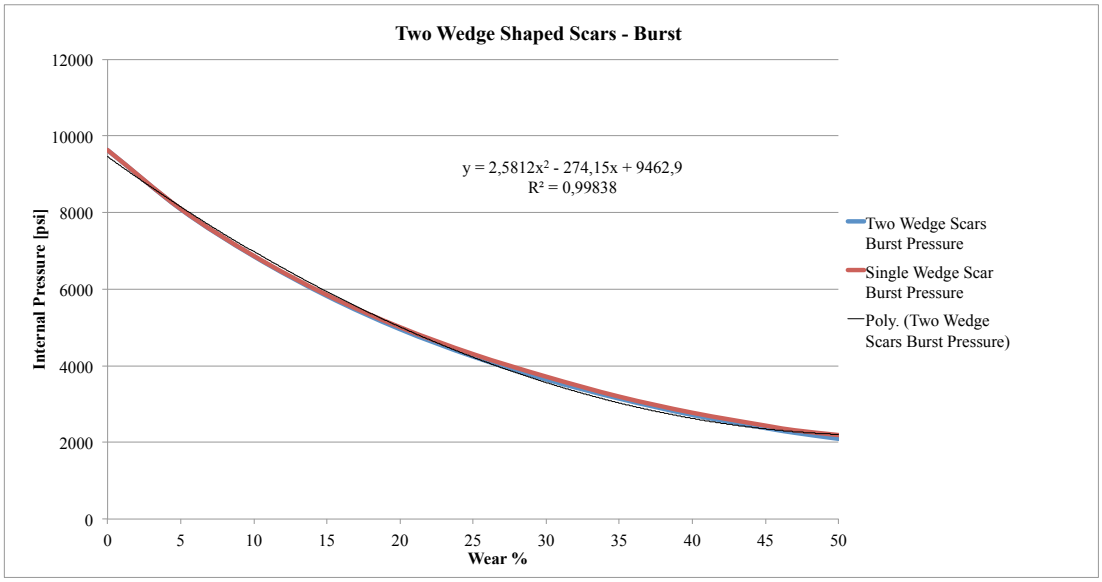

Figure 72: Safe and failure zone for operating internal pressure

Table 44: Result from linear interpolation for burst

Internal Pressure [psi]	Wear %
9641	0
8086	5
6858	10
5821	15
4955	20
4240	25
3643	30
3143	35
2717	40
2375	45
2251	47
2093	50

5.3.3 Mix of Two Scar Shapes

The next sections presents the simulated burst results for a tubing with two scars.

5.3.3.1 Mix of a Crescent Scar and a Wedge Scar - 25% Wear Model

For the 25% wear depth model with a two-wear scars, where one is a crescent shaped scar and the other is a wedge shaped scar, the burst pressure is equal to 4102 psi.

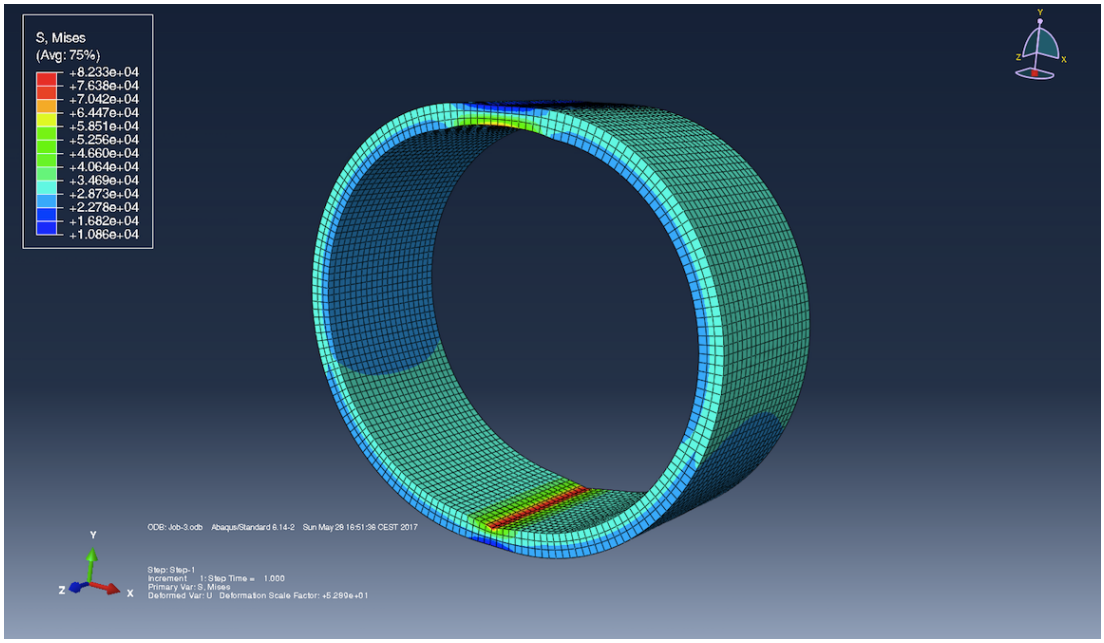

Figure 73: Simulated model with 25% wear scars and a internal pressure of 4200 psi

Table 45: Internal Pressure and Von Mises Stress for model with 25% wear

Internal Pressure [psi]	Von Mises Stress [psi]
4200	82330
4102	**80000**
4100	79950
4200	77570

5.3.3.2 Mix of a Crescent Scar and a Wedge Scar - 47% Wear Model

For the 47% model with a mix of a crescent scar and a wedge scar the burst pressure is simulated to 2131 psi.

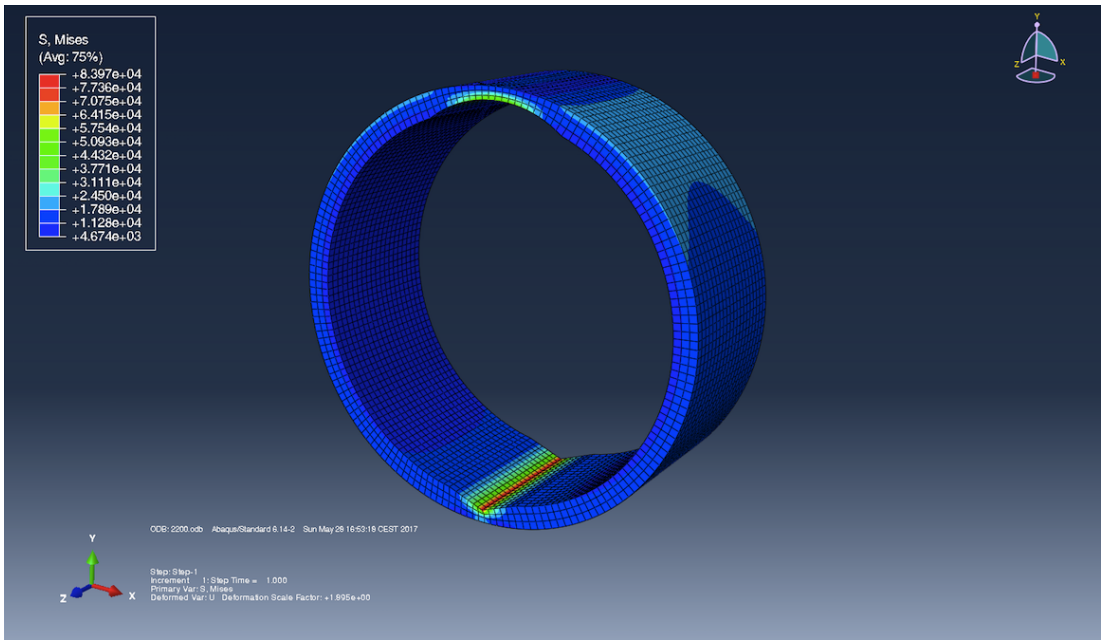

Figure 74: Simulated model with 47% wear scars and a internal pressure of 2200 psi

Table 46: Internal Pressure and Von Mises Stress for model with 47% wear

Internal Pressure [psi]	Von Mises Stress [psi]
2200	83970
2131	**80000**
2100	78250
2000	72520

5.3.3.3 Mix of a Crescent Scar and a Wedge Scar - Final Results - Burst

Figure 75 shows the internal pressure and the respective Von Mises stresses for the different wear depths. From the data in table 47 a curve that represents the safe and failure zone is generated (see figure 76).

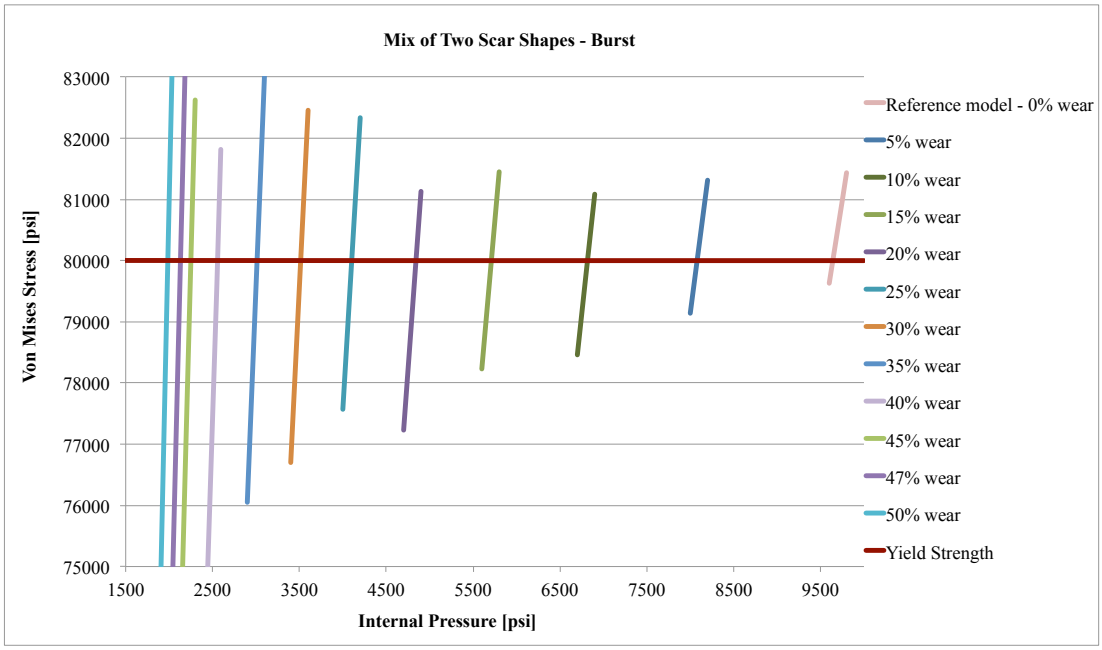

Figure 75: Internal pressure and the respective Von Mises Stress for different wear depths

Table 47: Result from linear interpolation for burst

Internal Pressure [psi]	Wear %
9641	0
8079	5
6816	10
5710	15
4842	20
4102	25
3515	30
3013	35
2559	40
2250	45
2131	47
1985	50

Generated model based on the curve from the simulated results:

$$P_{int} = 2,7118 \times WEAR\%^2 - 283,24 \times WEAR\% + 9479,5 \tag{71}$$

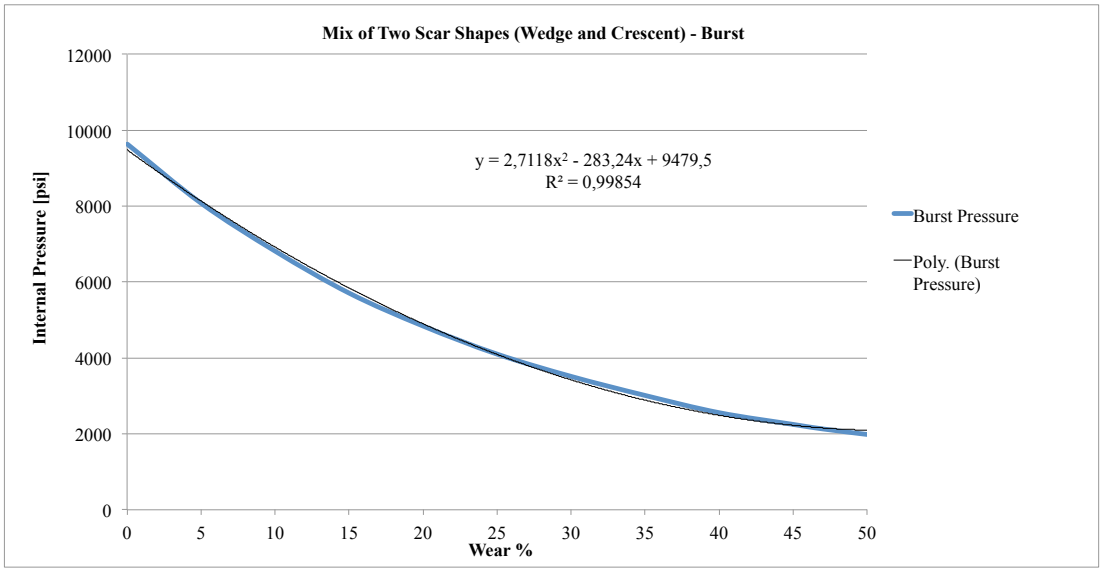

Figure 76: Safe and failure zone for operating internal pressure

5.3.4 Comparing The Two Scars Scenarios

In this section the different scenarios of two scars is compared. All three simulation-based models for each scenario is plotted in figure 77. According to the simulation the mix of a crescent shaped wear and a wedge shaped wear show very similar results as the two wedge shaped wear scenario. The highest burst pressure is observed for the scenario with two crescent shaped scars.

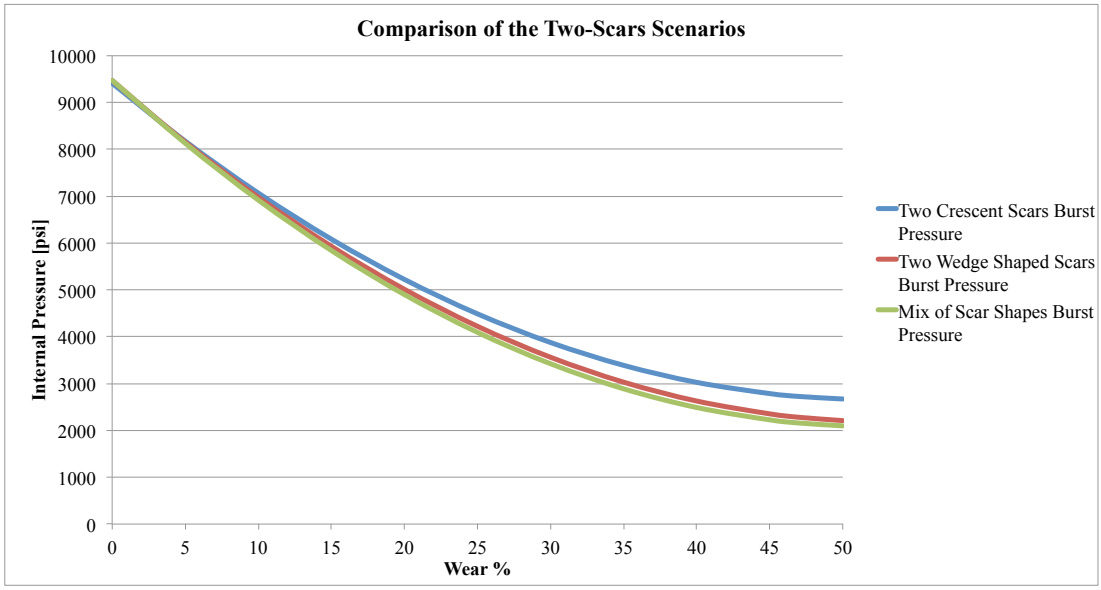

Figure 77: Comparison of the different two-scars scenarios

5.4 Collapse Modeling: Two Scars

5.4.1 Crescent Shaped Scars

The following sections presents the simulated collapse results for a tubing with two crescent shaped scars.

5.4.1.1 Crescent Shaped Scars - 25% Wear Model

The model with two crescent shaped scars with a wear depth of 25% show a collapse resistance of only 4166 psi. Compared to the reference model this is a reduction of 53%.

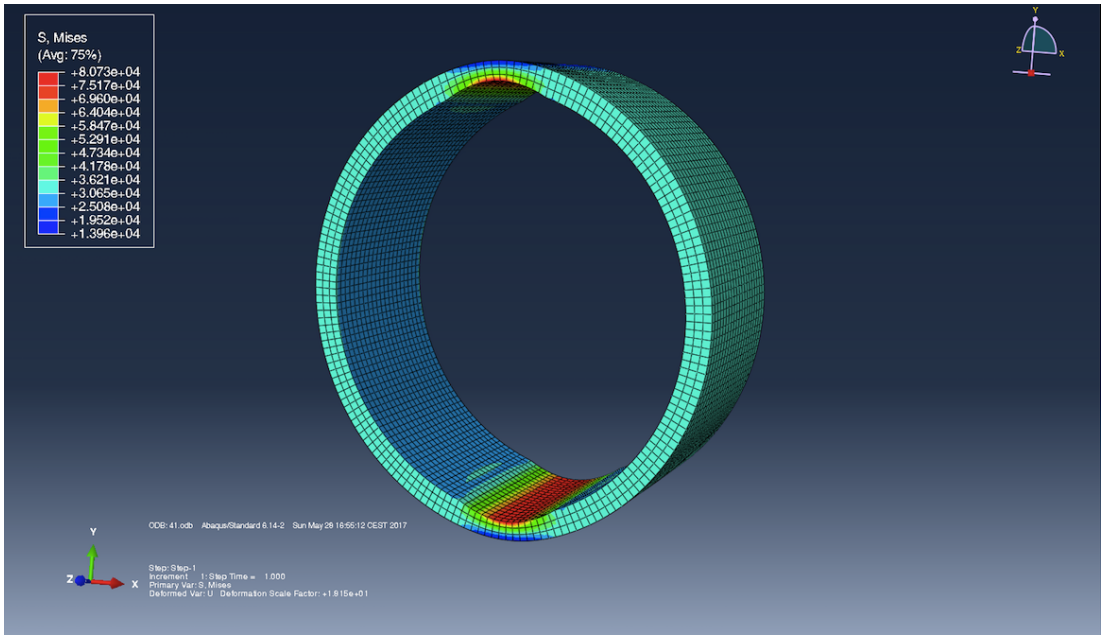

Figure 78: Simulated model with two 25% wear scars and a external pressure of 4200 psi

Table 48: External Pressure and Von Mises Stress for model with 25% wear

External Pressure [psi]	Von Mises Stress [psi]
4300	82900
4200	80730
4166	**80000**
4100	78560

5.4.1.2 Crescent Shaped Scars - 47% Wear Model

For the 47% model the collapse resistance is 2404 psi. A reduction of 73% compared to the reference model.

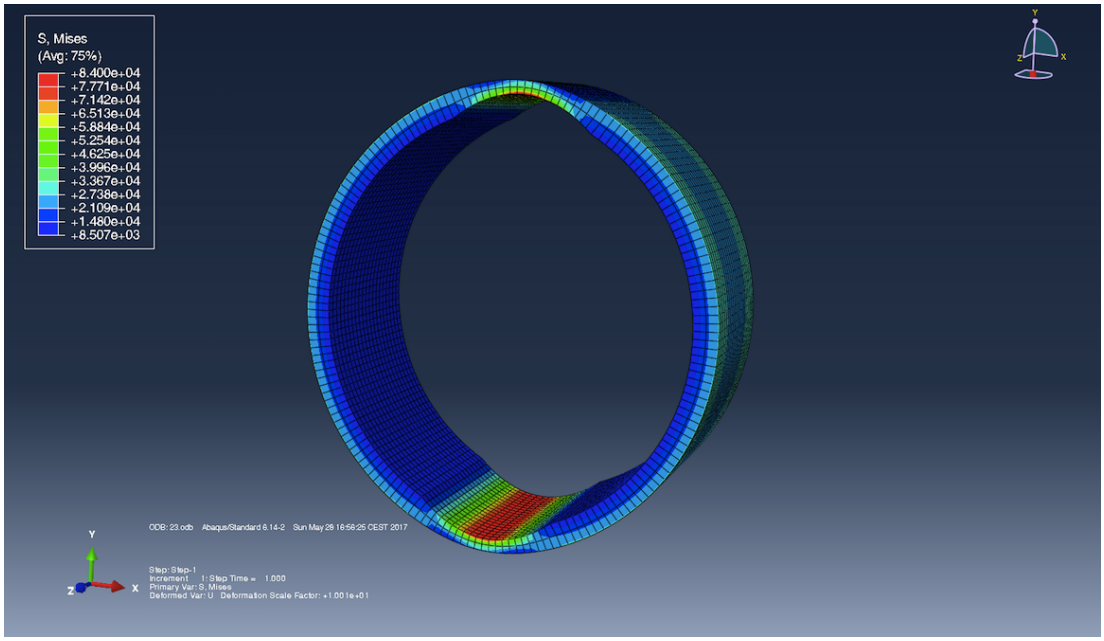

Figure 79: Simulated model with two 47% wear scars and a external pressure of 2500 psi

Table 49: External Pressure and Von Mises Stress for model with 47% wear

External Pressure [psi]	Von Mises Stress [psi]
2500	84000
2404	**80000**
2400	79840
2300	75670

5.4.1.3 Crescent Shaped Scars - Final Results - Collapse

In figure 80 the external pressure and the respective Von Mises stress for the different wear depths is illustrated. Similarly to the previous section the collapse resistance decreases with a increased wear depth.

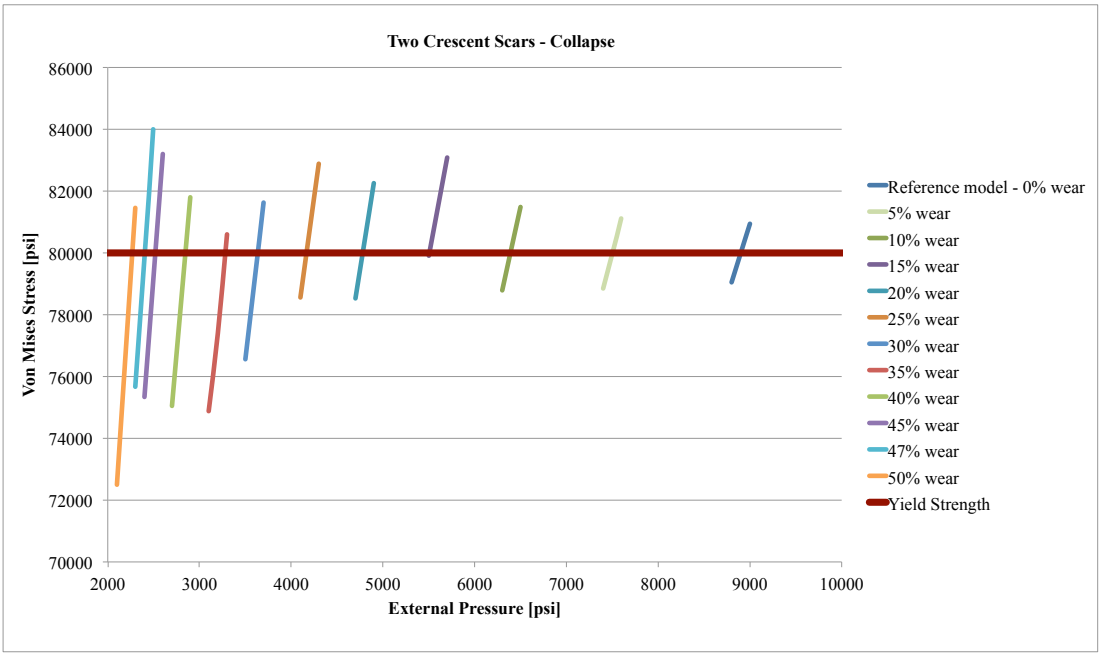

Figure 80: External pressure and the respective Von Mises Stress for different wear depths

Table 50: Result from linear interpolation for burst

External Pressure [psi]	Wear %
8900	0
7502	5
6389	10
5506	15
4779	20
4166	25
3636	30
3281	35
2846	40
2519	45
2404	47
2267	50

Table 50 shows the linear interpolated data which is used to generate the curve in figure 81. From this curve a model is generated. The simulation based model for a single scar is also presented. In this case the two scar model shows a lower collapse resistance than the single scar model.

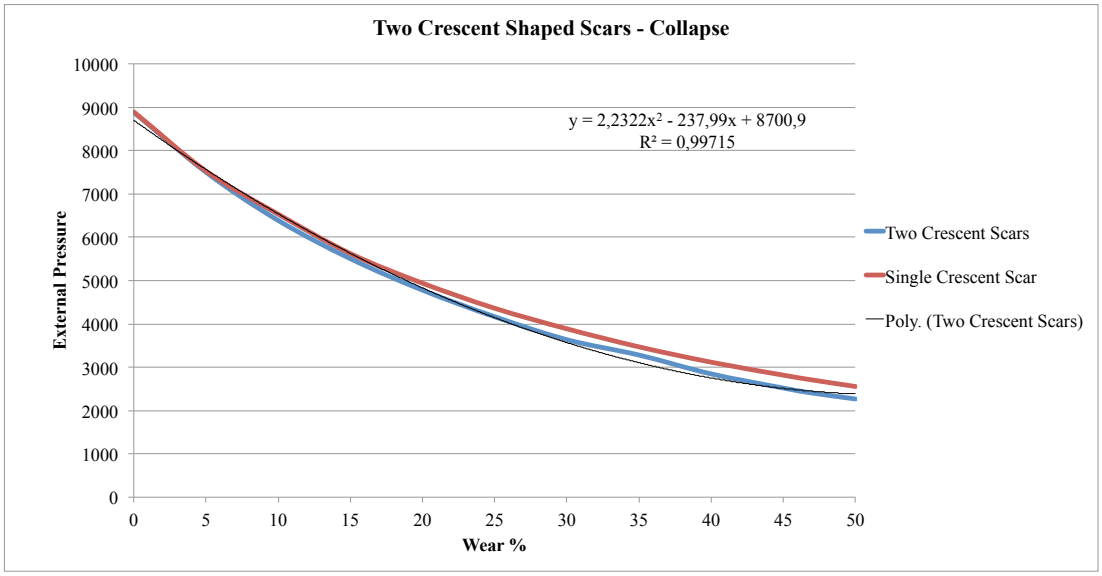

Figure 81: Safe and failure zone for operating external pressure

Model based on the simulated data:

$$P_{ext} = 2,2322 \times WEAR\%^2 - 237,99 \times WEAR\% + 8700,9 \tag{72}$$

5.4.2 Wedge Shaped Scars

The following sections presents the simulated collapse results for a tubing with two wedge shaped scars.

5.4.2.1 Wedge Shaped Scars - 25% Wear Model

The collapse resistance for the model with two wedge shaped scars with a wear depth of 25% is simulated to 3901 psi.

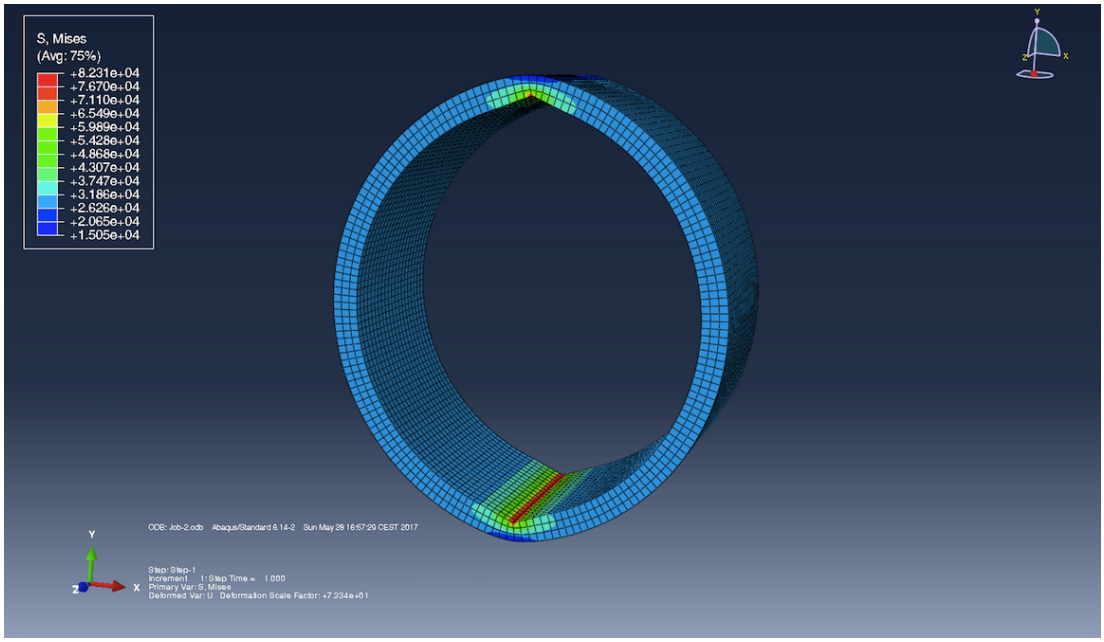

Figure 82: Simulated model with two 25% wear scars and a external pressure of 4000 psi

Table 51: External Pressure and Von Mises Stress for model with 25% wear

External Pressure [psi]	Von Mises Stress [psi]
4000	82310
3901	**80000**
3900	79970
3800	77630

5.4.2.2 Wedge Shaped Scars - 47% Wear Model

For the model of 47% wear depth the collapse resistance is 1987 psi.

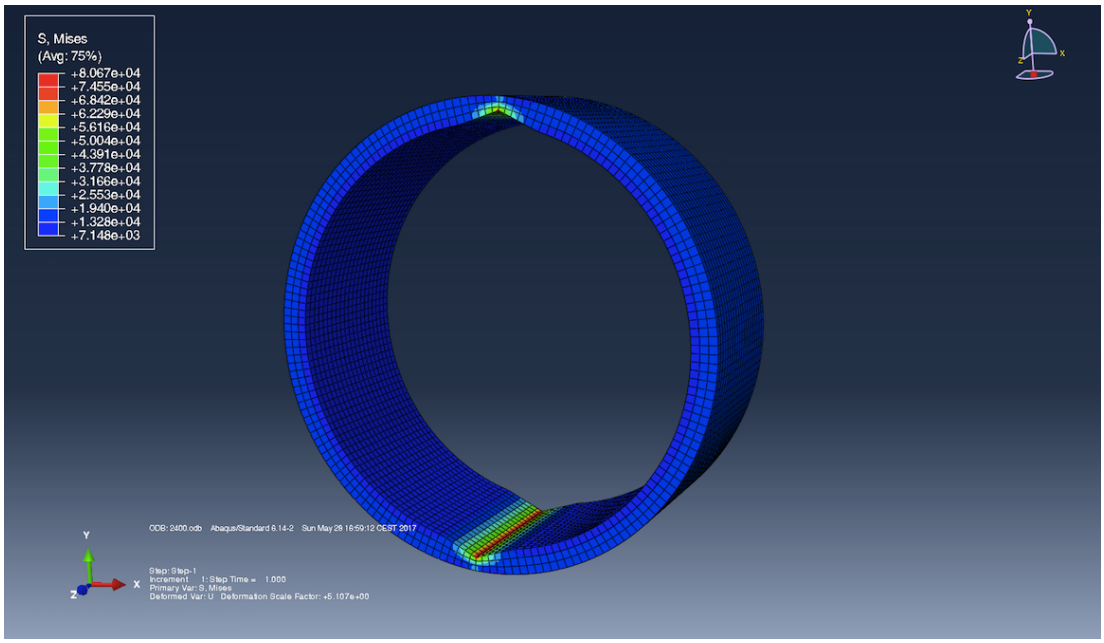

Figure 83: Simulated model with two 47% wear scars and a external pressure of 2000 psi

Table 52: External Pressure and Von Mises Stress for model with 47% wear

External Pressure [psi]	Von Mises Stress [psi]
2000	80670
1987	**80000**
1900	75360
1800	70030

5.4.2.3 Wedge Shaped Scars - Final Results - Collapse

Figure 84 illustrates the external pressure and the respective Von Mises stress for the different wear depths. The collapse resistance decreases with a increased wear depth.

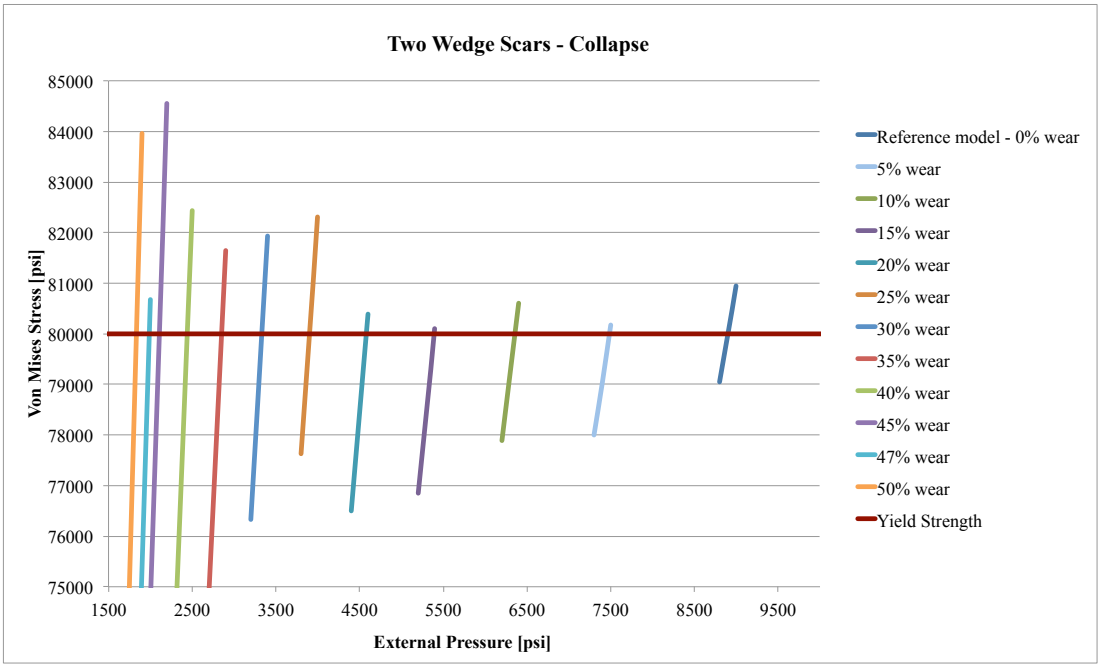

Figure 84: External pressure and the respective Von Mises Stress for different wear depths

Table 53: Result from linear interpolation for burst

External Pressure [psi]	Wear %
8900	0
7484	5
6355	10
5394	15
4580	20
3901	25
3331	30
2851	35
2440	40
2108	45
1987	47
1833	50

Results from the linear interpolation data in table 53 is used to generate the curve in figure 85. A model is generated based on the simulated data curve. The single scar model and the two scars model almost overlaps in this case.

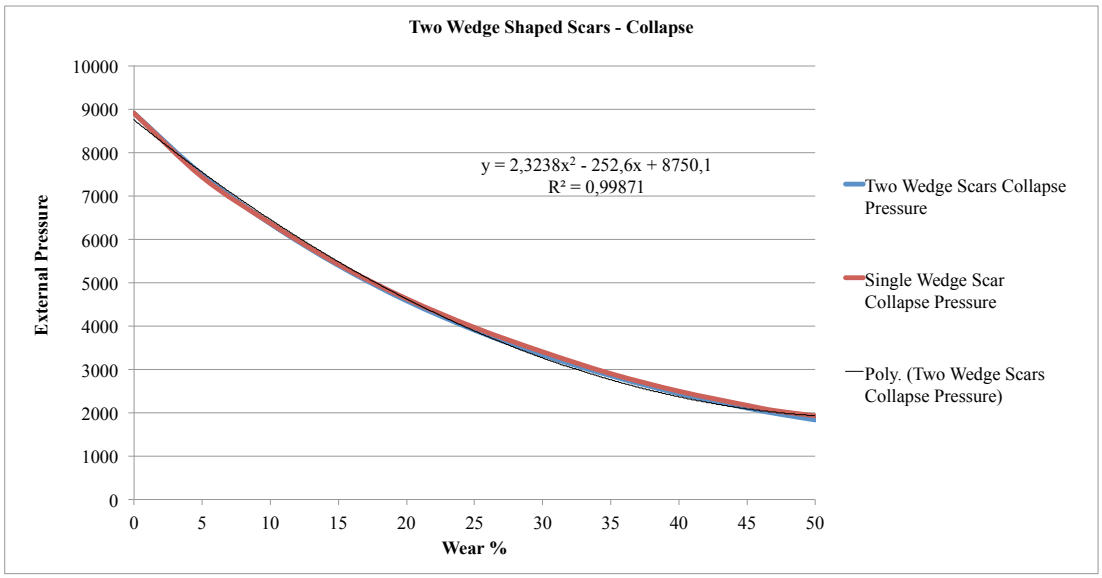

Figure 85: Safe and failure zone for operating external pressure

Model based on the simulated data:

$$P_{ext} = 2,3238 \times WEAR\%^2 - 252,6 \times WEAR\% + 8750,1 \quad (73)$$

5.4.3 Mix of Two Scar Shapes

The next sections presents the simulated collapse results for a tubing with two scars.

5.4.3.1 Mix of a Crescent Scar and a Wedge Scar - 25% Wear Model

For the model with a wear depth of 25% and two different wear scars the external pressure to start yielding is 3772 psi according to the simulation.

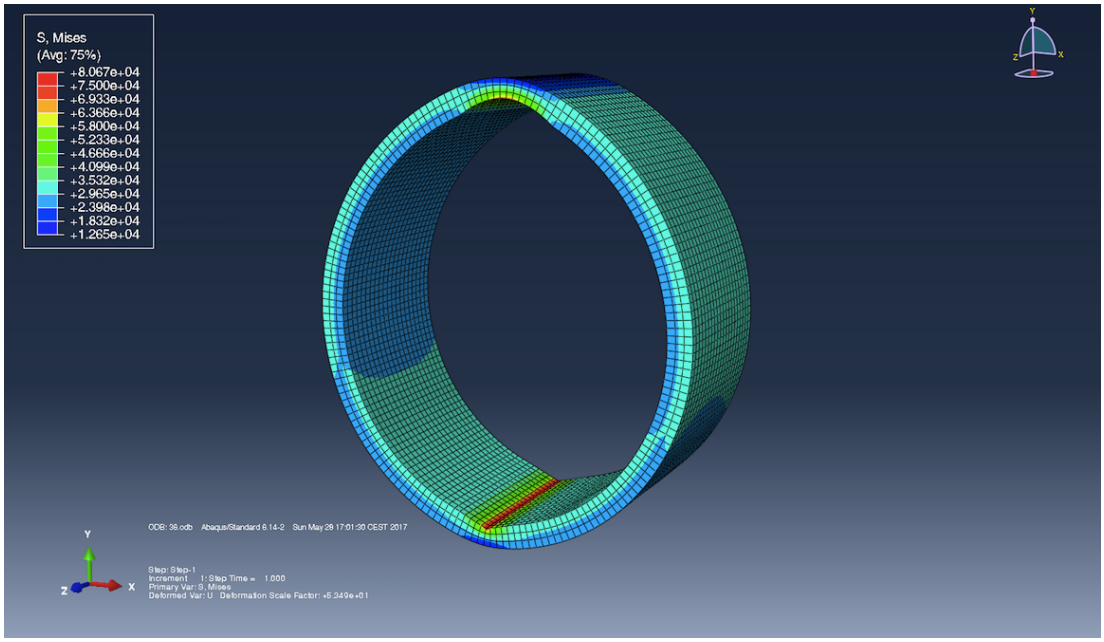

Figure 86: Simulated model with two 25% wear scars and a external pressure of 3800 psi

Table 54: External Pressure and Von Mises Stress for model with 25% wear

External Pressure [psi]	Von Mises Stress [psi]
3800	80670
3772	**80000**
3700	78240
3600	75910

5.4.3.2 Mix of a Crescent Scar and a Wedge Scar - 47% Wear Model

At 47% wear depth the pipe starts to yield when subjected to a external pressure of 1869 psi.

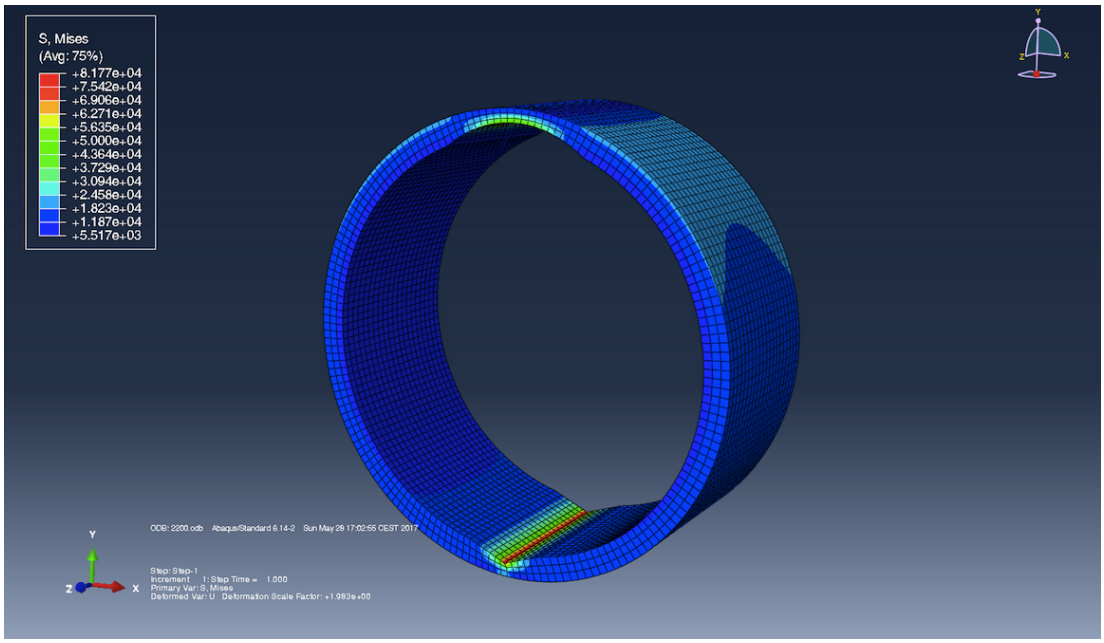

Figure 87: Simulated model with two 47% wear scars and a external pressure of 1900 psi

Table 55: External Pressure and Von Mises Stress for model with 47% wear

External Pressure [psi]	Von Mises Stress [psi]
1900	81770
1869	**80000**
1800	76000
1700	70220

5.4.3.3 Mix of a Crescent Scar and a Wedge Scar - Final Results - Collapse

Figure 88 illustrates how the collapse pressure limit for a tubing with two-wear scars decreases as the wear depth increases.

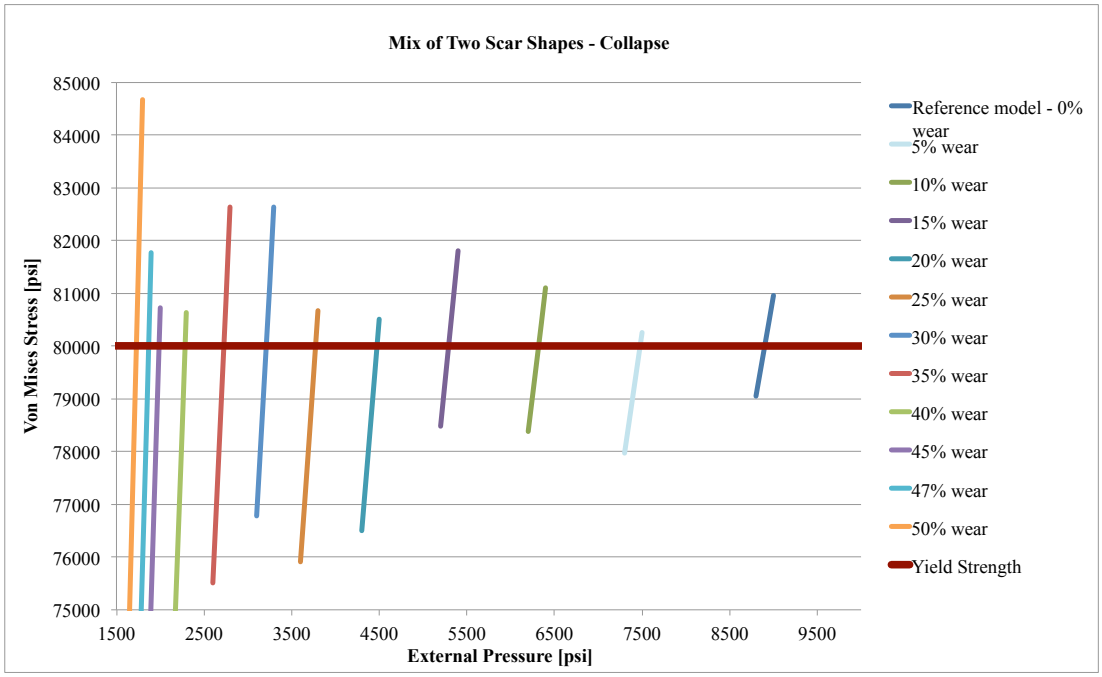

Figure 88: Safe and failure zone for operating external pressure

The linear interpolated values in table 56 is used to generate the safe and failure curve in figure 89.

Table 56: Result from linear interpolation for burst

External Pressure [psi]	Wear %
8900	0
7477	5
6319	10
5292	15
4475	20
3772	25
3210	30
2726	35
2286	40
1986	45
1869	47
1727	50

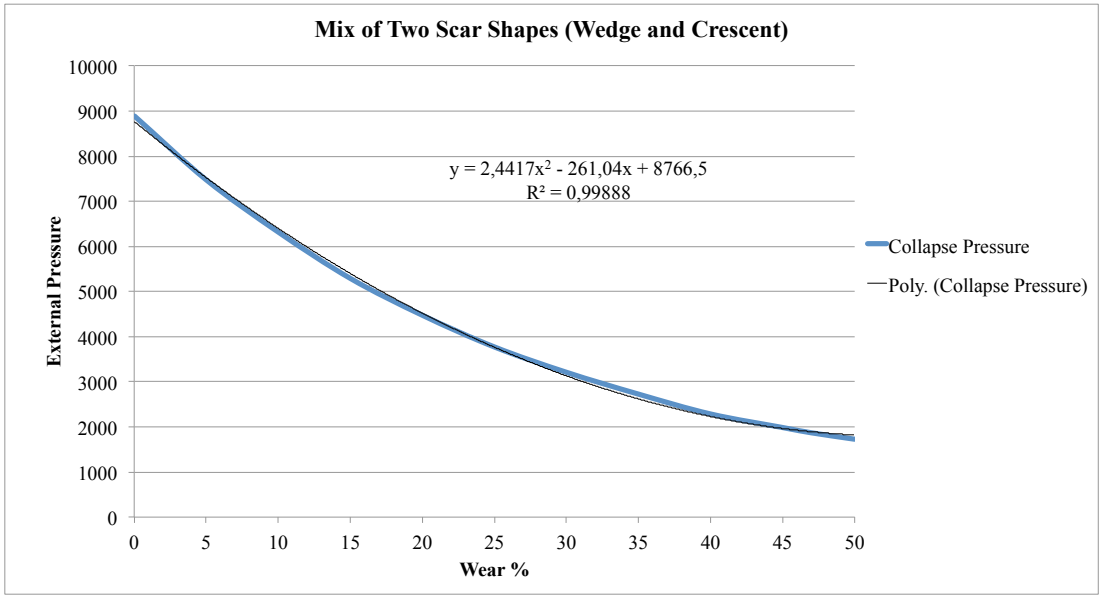

Figure 89: Safe and failure zone for operating external pressure

Generated model from the simulation results:

$$P_{ext} = 2,4417 \times WEAR\%^2 - 261,04 \times WEAR\% + 8766,5 \tag{74}$$

5.4.4 Comparing The Two-Scars Scenarios

Figure 90 shows the plot for all the three two-scars scenarios. The plot shows the simulation-based models for each scenario. Similarly as for the burst pressure comparison of the scenarios the crescent scars shows the highest collapse resistance, followed by nearly overlaped curves of the other scenarios.

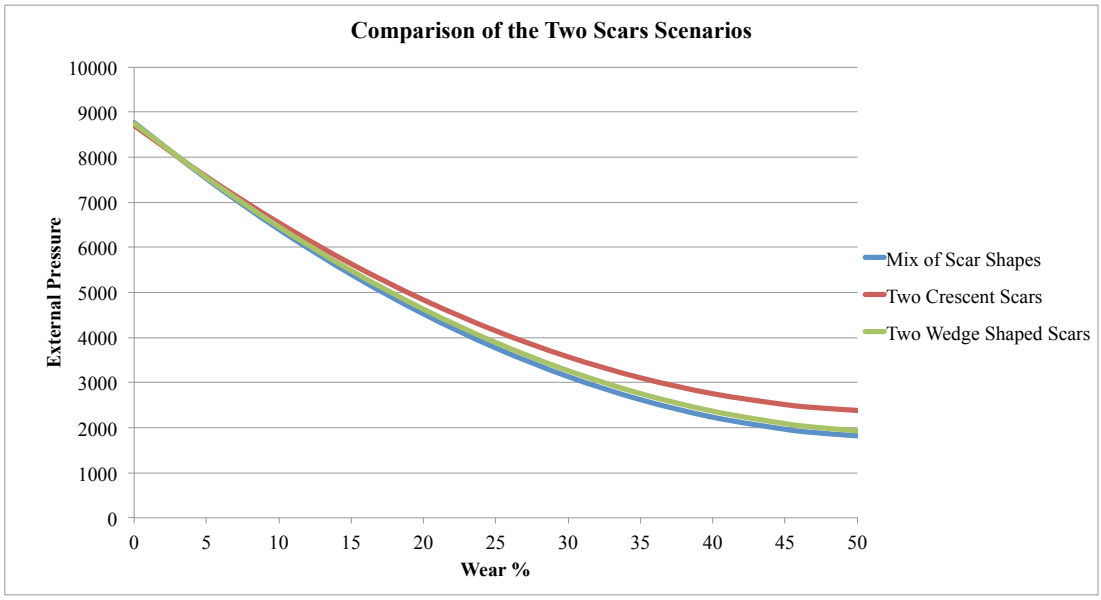

Figure 90: Comparison of the generated models of the different two-scar scenarios

5.5 The Effect of Temperature - Burst

This section presents a theoretical and simulated analysis where stresses caused by temperature changes and pressures have been included. As mention in section 3.1, a differential temperature may cause additionally stresses in a cylindrical pipe. Consider a production well that has been shut in for a period of time. The well temperature has now stabilized and is equal to the surrounding formation temperature, hence the differential temperature is equal to zero. However, when the well start producing, there can be short period of time (before the temperature stabilizes) where the temperature in the well is greater than in the A-annulus, causing a differential temperature, ΔT. In this scenario a geothermal gradient of $1°F$ / 70ft is assumed, hence, at 1626 ft. the temperature in the A-annulus is calculated to be 23° Fahrenheit. According to Puntervold et. al the reservoir temperature at the Ekofisk Field is 266° farenheit [21], this temperature will be used as the well flow temperature. Figure 91 illustrates how the temperature in a well changes as a function of time.

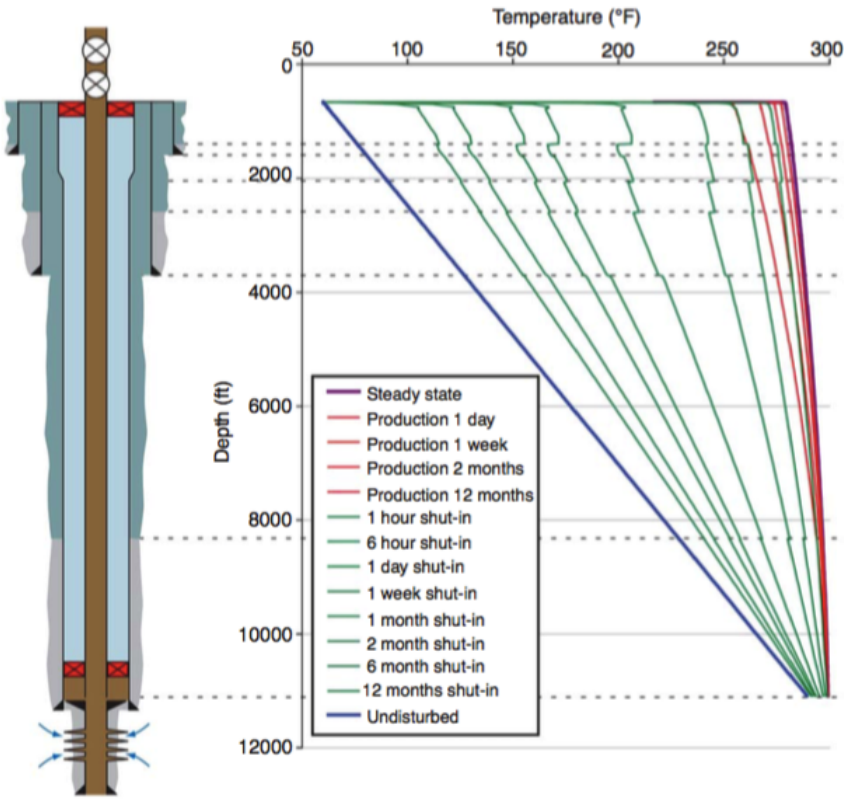

Figure 91: Temperature profiles in a well as a function of time [5]

5.5.1 Theoretical Stresses

In this section the theoretical stresses due to temperature changes and pressures are presented. The equations used are presented in section 3.1. By using these equations the theoretical stresses in a unworn thick-walled cylinder were calculated and plotted in excel. Figure 92 and figure 93 show the radial, hoop and axial stresses in a thick-walled cylinder based on the data given in table 57.

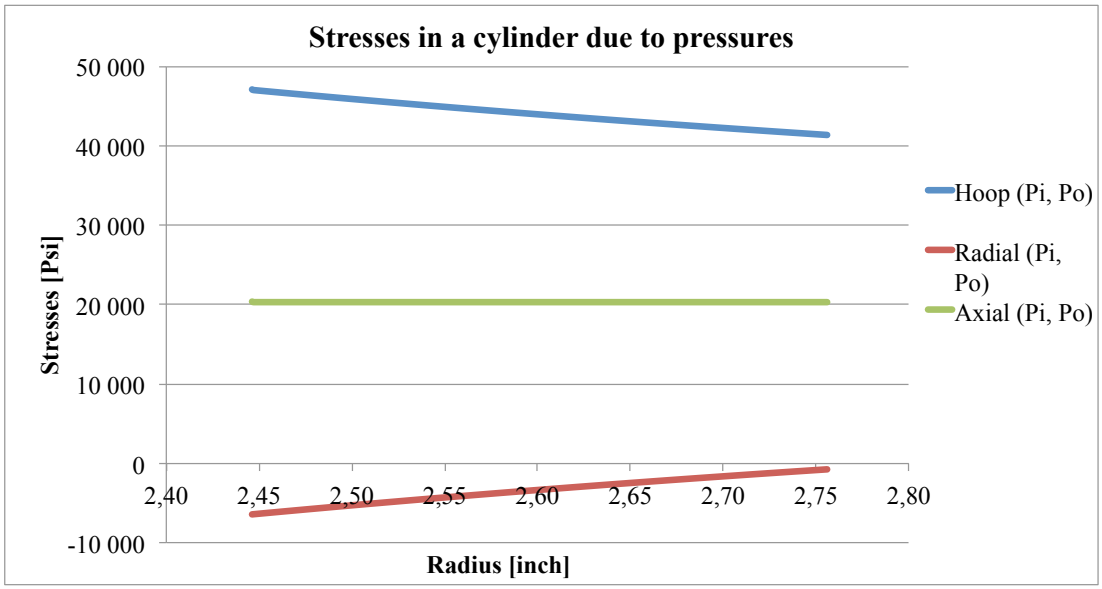

Figure 92: Stresses in a unworn thick-walled cylinder due to pressures

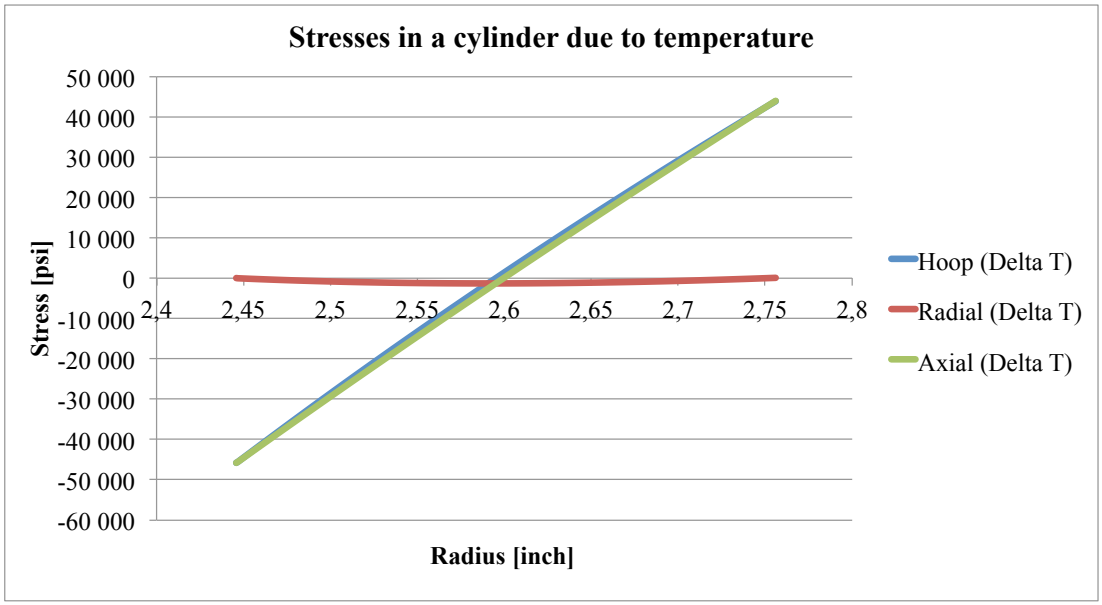

Figure 93: Stresses in a unworn thick-walled cylinder due to temperature changes

Table 57: Input used in the mathematical equations

Input data	
P_i	6200 psi
P_o	727 psi
a	2,446 in.
b	2,75 in.
α	0,00001
E	200 GPa
T_i	266°F
T_o	23°F
ΔT	243°F

The results obtained by inserting the combined radial, hoop and axial stresses (as displayed in the two plots above) into the Von Mises stress equation (eq. 24) is illustrated in figure 94. The plot is based on the mathematical equations and shows that when the hoop stress, radial stress and axial stress caused by temperature and pressure are combined, the Von Mises stress is actually greatest at the outer wall of the cylinder (76315 psi). From the inner wall the Von Mises decreases until it reach a point where the stress starts to increase.

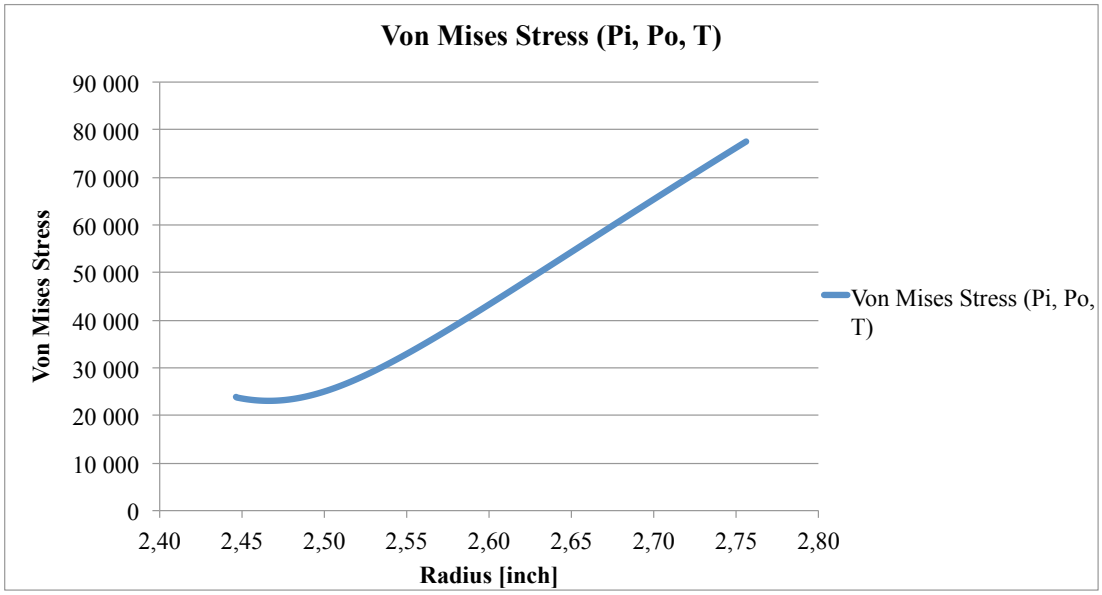

Figure 94: Von Mises Stress in a unworn thick-walled cylinder due to temperature and pressure - Burst

5.5.2 Simulated Results

The upcoming sections presents the results from the Abaqus simulations where the models were subjected to pressures and temperatures. The same burst scenario details as described in section 5.1 is used, with an additional temperature.

5.5.3 Reference Model - Pressure and Temperature Loadings

In order to simulate the stresses caused by temperature and pressure a 2D model was built (see figure 95). The input data in table 57 have been used in the simulations.

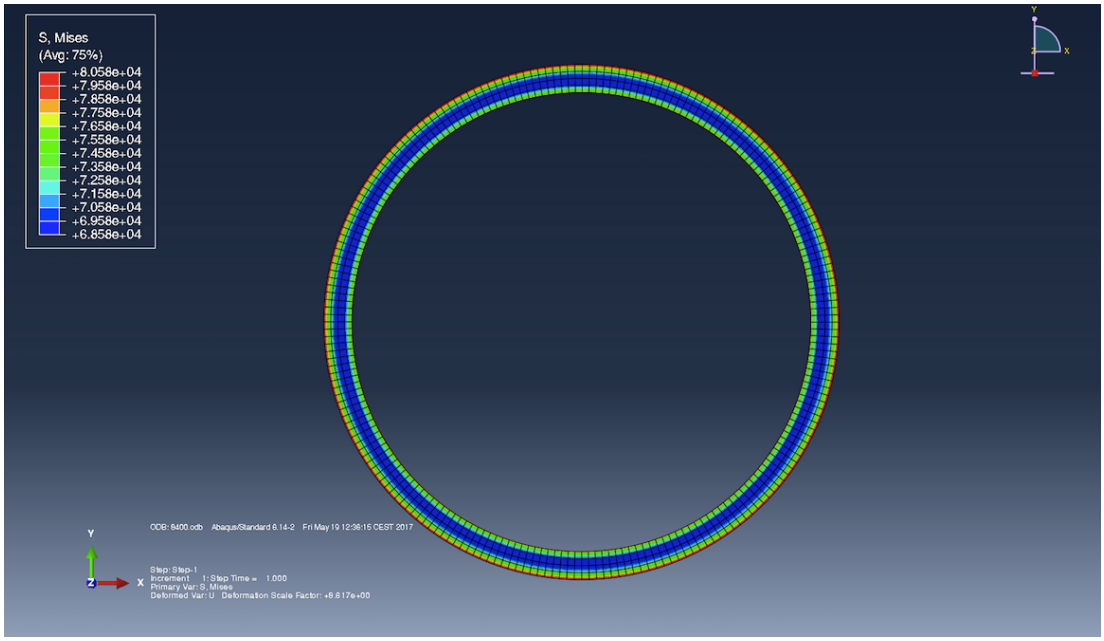

Figure 95: Reference model with a internal pressure of 6200 psi. ΔT is equal to 243°F

Table 58: Internal Pressure and Von Mises Stress for model with 0% wear

Internal Pressure [psi]	Von Mises Stress [psi]
6200	80580
6115	**80000**
6100	79890
6000	79200
ΔT	243°F

According to the simulation (see figure 95) the Von Mises stress starts to decrease from the inner wall until it reach a point where the stress starts to increase. The highest Von Mises stress is observed at the outer wall. The red color indicates the maximum, and the blue color indicates the minimum stress. The simulated stress distribution in the cylinder wall is supported by the results from the theoretical section (section 5.5.1). Figure 96 shows the Von Mises stress across the wall of the tubing. In this case, the burst pressure of the unworn tubing is 6115 psi.

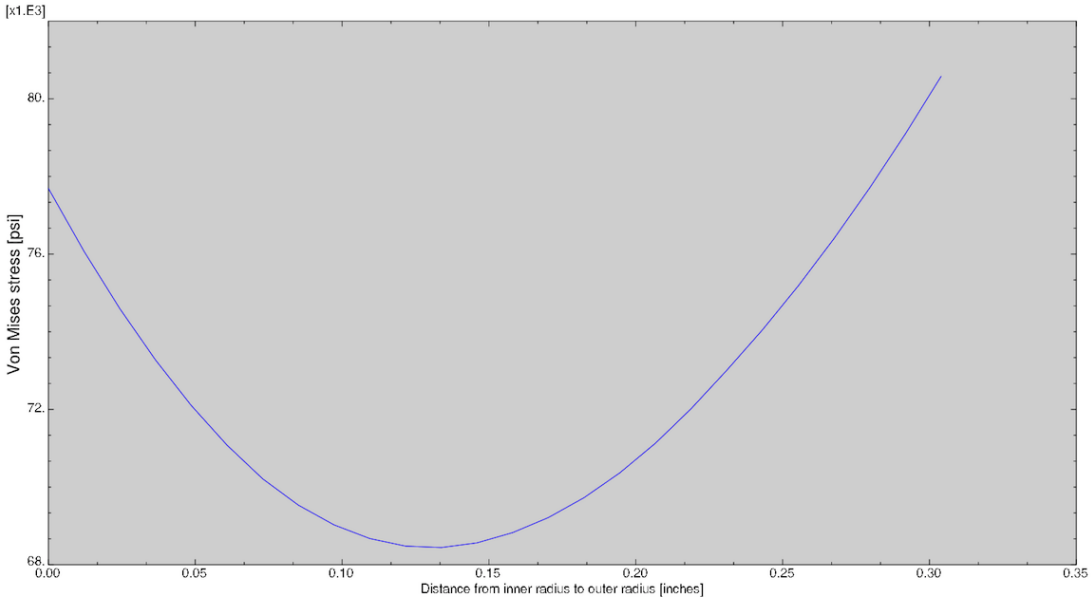

Figure 96: Simulated Von Mises stress across the wall of the tubing (plot from Abaqus)

5.5.4 Reference Model - Only Pressure Loadings

A 2D model subjected to pressure loadings only was built in order to have a comparison to the 2D model exposed to temperature and pressure loadings. When only pressure loadings is present, the Von Mises stress is highest at the inner wall, as seen in figure 97. The unworn reference model has a burst resistance of 9760 psi.

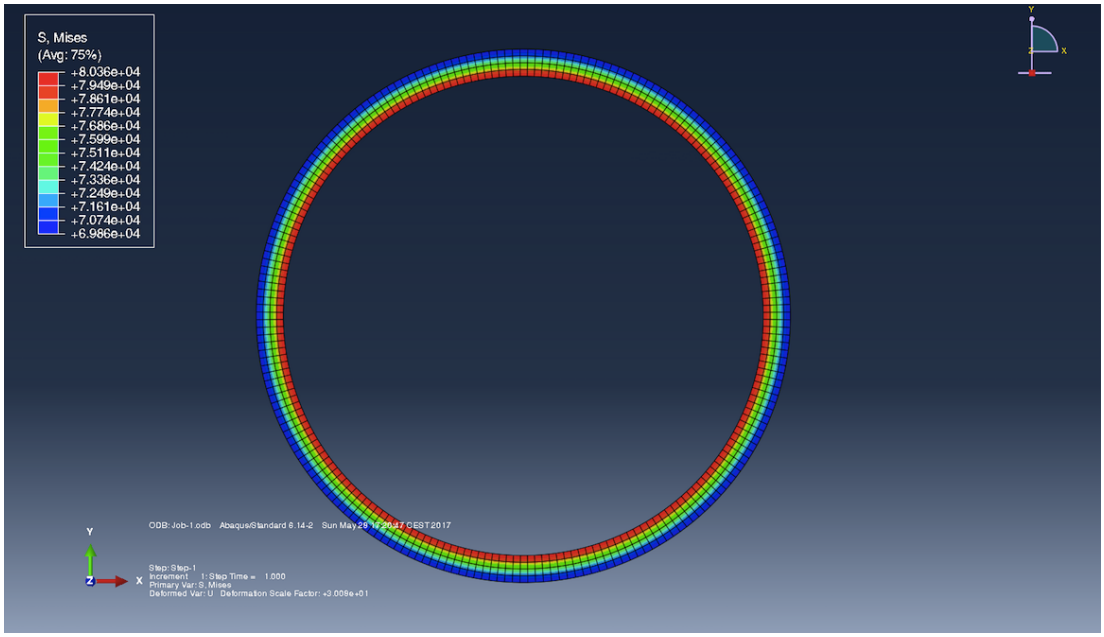

Figure 97: Reference model with a internal pressure of 9800 psi. ΔT is set to 0

Table 59: Internal Pressure and Von Mises Stress for model with 0% wear

Internal Pressure [psi]	Von Mises Stress [psi]
9800	80360
9760	**80000**
9700	79470
9600	78580
ΔT	0°F

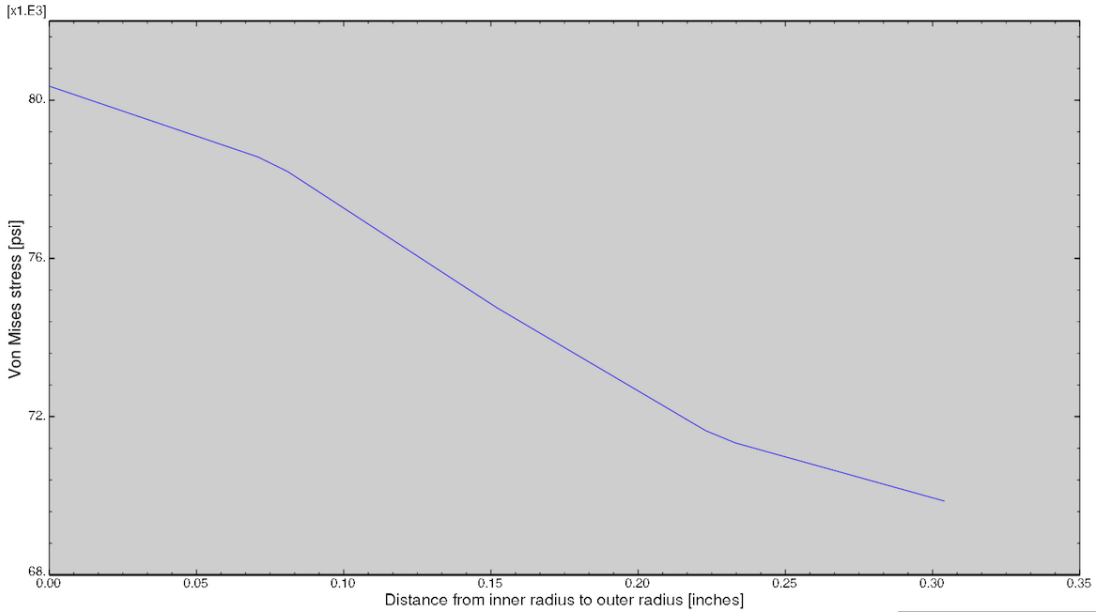

Figure 98: Simulated Von Mises stress across the wall of the tubing (plot from Abaqus)

5.5.5 Comparison Of The Loadings

According to the simulated results presented in section 5.5.3 and 5.5.4, the high temperature causes a reduction in the burst pressure of 3730 psi. The model subjected to pressure and temperature loadings shows a burst pressure of 6115 psi, while the model subjected to pressure loadings shows a burst resistance of 9760 psi. In the next sections the simulated results of a tubing with a crescent shaped wear and a wedge shaped wear subjected to the different loadings are presented.

5.5.6 Crescent Shaped Wear

The simulated results are based on a tubing with a crescent shaped wear for different wear depths. Figure 99 shows the burst pressure when the tubing subjected to temperature and pressure loadings in the red curve, and the burst pressure when the tubing is subjected only to pressure loadings in the blue curve. When the temperature loading is included, there is a immediately reduction in burst pressure of 38% (unworn tubing). As the wear depth increases, the burst pressure decreases, for both loading scenarios. At approximately 40% wear depth the curves intersect and the pressure curve (where the tubing is only subjected to pressure loadings) has the lowest burst pressure limit.

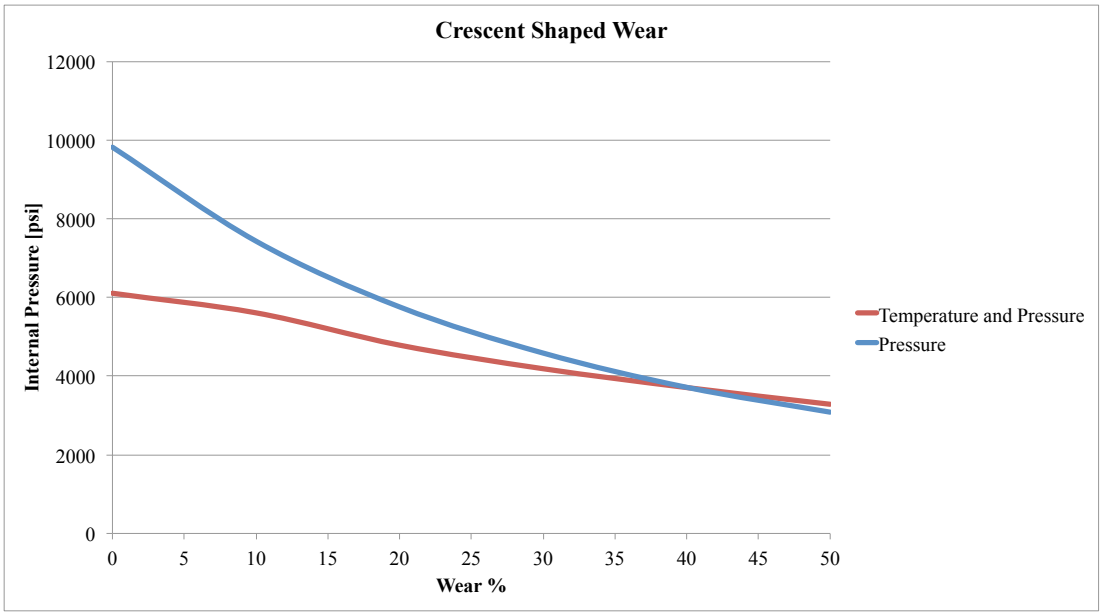

Figure 99: Burst pressure as a function of wear depths

5.5.7 Wedge Shaped Wear

In this section the burst pressure for a wedge shaped wear under the different loadings is presented. The width of the wear is held constant at 1 inch. As expected, the burst pressure reduces as the wear depth increases. When a high temperature loading is included, the burst pressure reduces significantly. Similar to the crescent shaped wear, the curves intersects at 40% wear depth. From this point the pressure curve has the lowest burst limit. Figure 100 illustrates the loading scenarios.

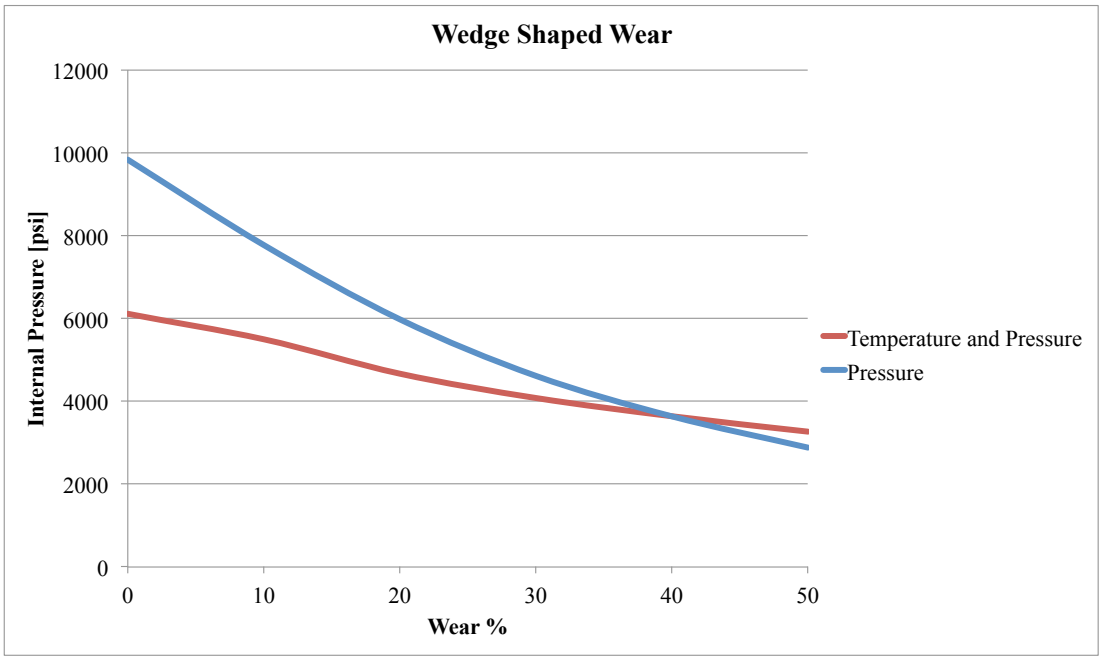

Figure 100: Burst pressure for different wear depths for the various loadings

5.5.8 Comparison of The Wear Shapes

Figure 101 illustrates the simulation-based models for the two wear shapes when they are subjected to temperature and pressure loadings. The models are also compared to the Barlow's model. Safety factor is not included. According to the simulations, there are not much difference between the wear shapes regarding burst pressure when temperature is included, however, as previously observed, the wedge shaped wear is still the most critical. The Barlow's equation once again over-predicts the burst pressure significantly for all wear depths. The simulations show that when a high differential temperature is present, the burst pressure reduces dramatically, even for a unworn tubing.

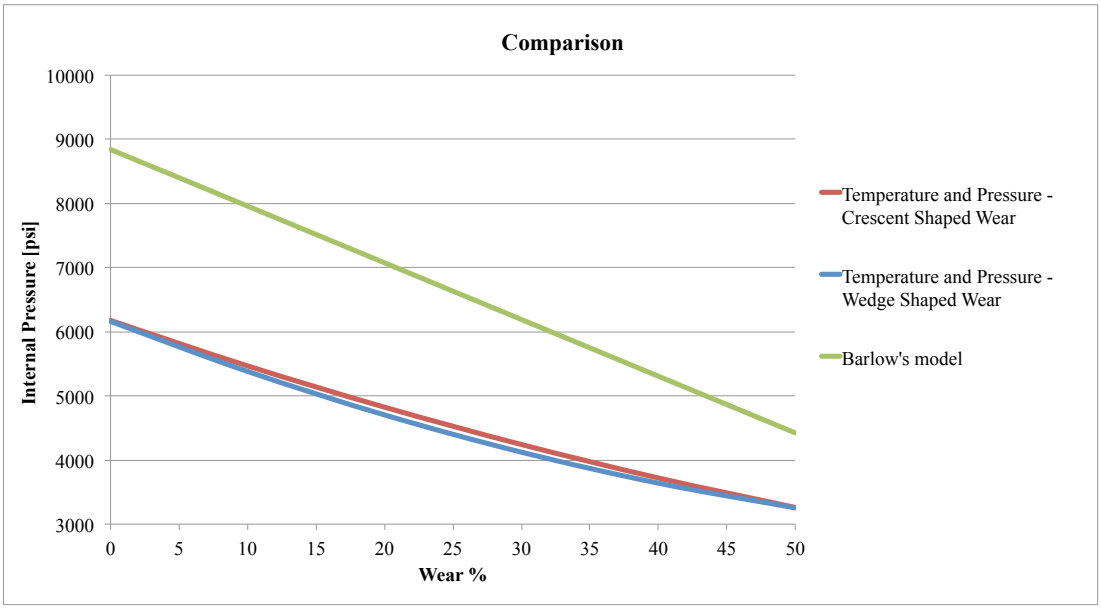

Figure 101: Simulation based model for burst pressure for different wear depths under temperature and pressure loadings - Safety factor not included

6 Summary And Discussion

Petroleum wells needs to be designed and constructed with the objective of maintaining a sufficient well integrity to eliminate the risk of uncontrolled release of formation fluids during the production period. The NORSOK D-10 standard requires that the casing and tubing shall carry all realistic loads during the life time of the well and that appropriate materials needs to be selected in order to resist and tolerate corrosive environment. This section summarizes the main results obtained from the burst and collapse analysis.

In order to investigate if the current API models that is used as a company standard [5] are applicable for a local wear, numerous FEM analyses were performed. A test model with uniform wear was compared to three different shapes of local scars. The simulation showed that the stress concentration was highest within the scar area, and not uniformly distributed, which is assumed by the API models. In addition, the simulation showed that if the uniform-wear method was used for a local wear the prediction of the de-rated tubing strength, stress distribution and magnitude probably would be incorrect. All simulations showed that the highest stress concentration was found within the damaged area. This was observed for all three local wear shapes, for both the burst and collapse scenarios. The stress magnitude within the local wears was found to be significantly higher than for the uniform wear. In worst case scenario the de-rated burst and collapse resistance of the tubing could be over-predicted, and thus lead to yielding of the pipe. To get a clearer overview of the results presented in section 5 a analysis in terms of % deviation between the API models and the FEM simulation results are discussed in the upcoming sections.

6.1 Burst Analysis

The following analysis is based on the results presented in section 5.1 and 5.3. The percent deviation between the Barlow's equation (eq. 44) for burst and the generated FEM models for single wears is presented in figure 102. The crescent shaped wear shows a maximum deviation of 71% when compared to the Barlow's equa-

tion. The wedge shaped wear and the rectangular wear show a deviation of 114% and 147%, respectively. This means that the Barlow's equation over-predicts the maximum internal pressure for a locally damaged tubing.

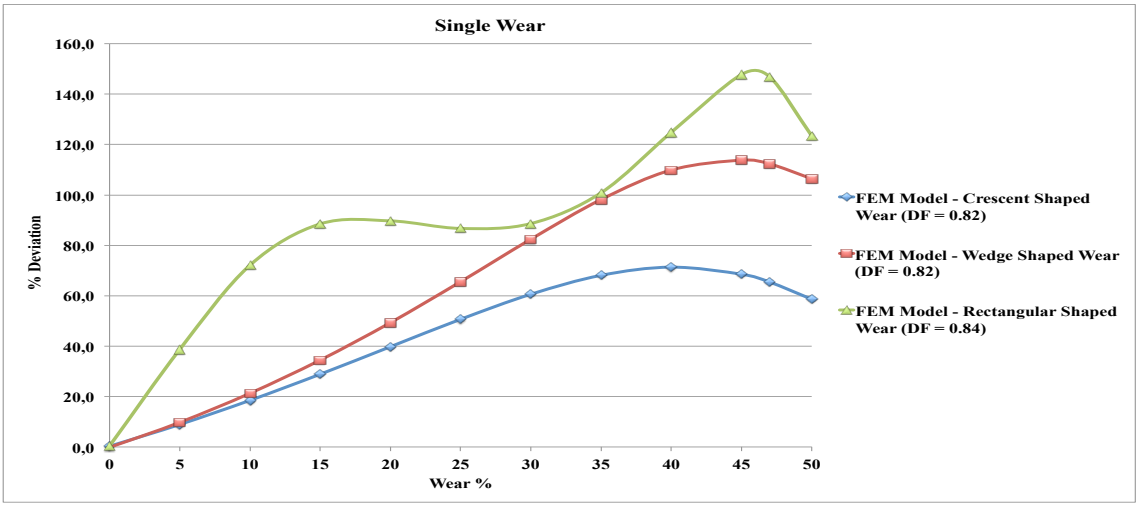

Figure 102: Percent Deviation between Barlow's model and the simulation based models for the different single wear shapes

Similarly, the percent deviation between the simulation-based models for two scars and the Barlow's equation is presented in figure 103. As the wear depth increases from 0% to 50%, the deviation between the Barlow's prediction and the FEM models increases significantly. For the crescent shaped scars a maximum deviation of 87% is observed. The wedge shaped scars and the mix of two wear shapes shows a deviation of 121% and 133%, respectively.

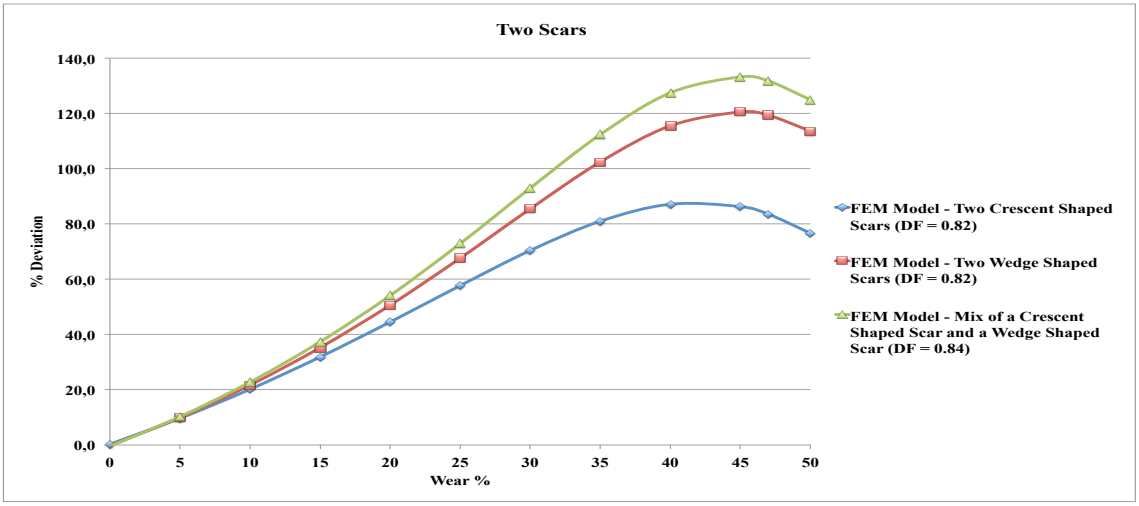

Figure 103: Percent Deviation between Barlow's model and the simulation based models for two scars

For the scenario where temperature is included, a deviation up to 46% is observed for the crescent shaped wear. The wedge shaped wear shows a deviation up to 51%. Figure 104 illustrates the difference between the Barlow's equation and the FEM models where temperature and pressure loadings are included. Once again, the Barlow's equation over-estimates the burst pressure limits. When a high differential temperature is included, the burst limit reduces drastically, even for a unworn tubing. The effect of temperature should therefore always be included in de-rating burst simulations of a cylindrical pipe.

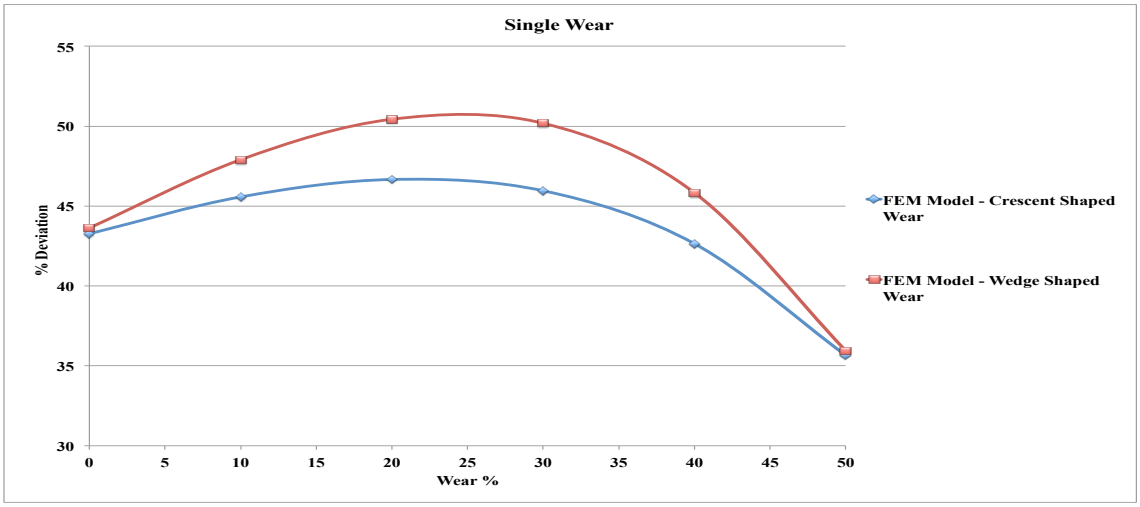

Figure 104: Percent Deviation between the Barlow's equation and the simulation based models when the effect of temperature is included

6.2 Collapse Analysis

This section is based on the results presented in section 5.2 and 5.4. Figure 105 shows the deviation between the simulation-based models for a single wear and the API collapse models (see section 3.8). The positive deviation means that the theoretical API collapse equations estimates a higher external pressure than the pipe actually can withstand. Up to 30%, the crescent wear nearly capture the API models for collapse. The wedge shaped and rectangular shaped wear have a deviation of 12% and 53%, respectively. The transition from positive to negative value represents the intersection between the FEM models and the API models. The negative value means that the simulated models estimates a higher value of the collapse resistance than the API collapse equations. The crescent shaped wear

shows a maximum deviation of 46% (negative). The wedge shaped and rectangular shaped show a deviation of 27% and 21%, repectively (negative).

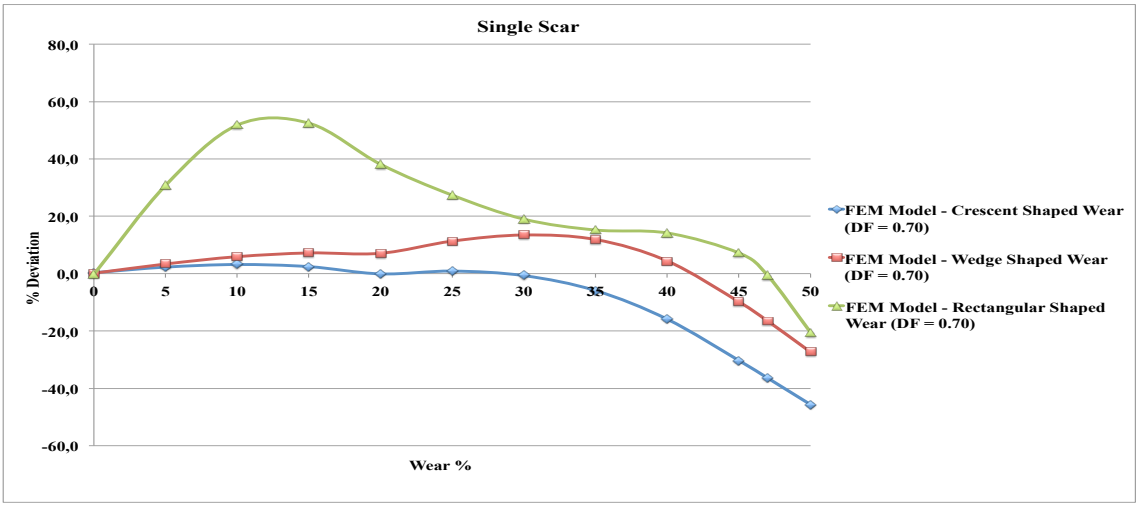

Figure 105: Percent Deviation between the theoretical collapse equations and the simulation based models for single scars

The deviation between the FEM models for two scars and the theoretical collapse equations is showed in figure 106. Similarly, the positive deviation means that the theoretical formulas over-predict the collapse resistance, while the negative value means that the FEM models over-predict the collapse resistance of the tubing. The crescent shaped wear show a positive deviation of 6%, and a negative deviation of 39%. The wedge shaped and rectangular shaped shows a positive deviation of 14% and 20%, and negative deviation of 25% and 20%, respectively.

Figure 106: Percent Deviation between the theoretical collapse equations and the simulation based models for two scars

The models were built under the assumption of symmetrical shaped wears. The Finite Element Method modeling and analysis was done for several different scenarios. The target was to investigate how the stress was affected when a tubing is locally worn and subjected to different types of loading. The FEM modeling calculates the Von Mises stress based on the radial-, hoop- and axial stresses that is created in the pipe wall. The data used in the simulations is gathered from the well located at the Ekofisk Field, as mentioned in section 1.1.2. The results from the simulations does not include stresses due to bending.

It is important to notice that the simulated results and models generated in this thesis is only valid for these particularly cases with these well parameters, loadings and material properties. The method of analysis that is developed in this thesis can only be used for other cases with different circumstances if the corresponding input parameters is changed.

7 Conclusion

The commercial softwares and models adapted by the industry today analyze a damaged tubular as a uniform circular cylinder. However, investigations performed with a caliper log revealed that tubular damages actually are non-uniform. Due to this observations, this thesis analyzes a damaged tubing by using the Finite Element Method and compare the results with the API models.

Based on the results from the FEM simulations, the conclusions for this thesis are:

- The shape of the wear is found to have a great impact on the reduced burst and collapse limits for a tubing. The most critical local wear shape, for both the burst and collapse scenarios, is the rectangular shaped wear, followed by the wedge shaped wear and the crescent shaped wear. Since corrosion can create various wear shapes, extra attention should be paid when estimating the de-rated burst and collapse pressure of a locally corroded tubing.

- The Barlow's equation is found to predict a significantly higher burst pressure limit than the FEM simulations for a locally worn production tubing, for both the single and double scar scenarios. The safe operational window for the Barlow's formula was found to be considerably higher than for the local wears. Thus, the Barlow's equation is found to not be applicable for a locally worn tubing.

- The collapse models for uniform wear was found to over-predict the collapse resistance for all the simulated single scar and double scar scenarios, thus, the API collapse models should not be used for a locally worn tubing. However, depending on the wear shape, at a certain wear depth the FEM results actually showed a higher collapse resistance than the collapse models.

- When the combination of high pressure and a high differential temperature is included in the simulations the yielding pressure is found to be significantly lower than if only pressure loadings is present, even for a unworn tubing. Thus, the effect of temperature should be included during de-rated burst and collapse simulations of tubulars, for both local and uniform wear.

References

[1] B Vignes, J Andreassen, and SA Tonning. Psa well integrity survey, phase 1 summary report. *Petroleum Safety Authority http://www. ptil. no/getfile. php/z% 20Konvertert/Helse% 20miljø% 20og% 20sikkerhet/Sikkerhet% 20og% 20arbeidsmiljø/Dokumenter/nettpsawellintegritysurveyphase1reportrevision3006. pdf*, 2006.

[2] Therese Vu. Finite element method simulation and modeling of tubing wear. Master's thesis, University of Stavanger, Norway, 2015.

[3] Standard Norge. Norsok standard : Well integrity in drilling and well operations. volume Rev. 4. ed. Vol. D-010. Society of Petroleum Engineers, 2013.

[4] Birgit Vignes, Bernt Sigve Aadnoy, et al. Well-integrity issues offshore norway. In *IADC/SPE Drilling Conference*. Society of Petroleum Engineers, 2008.

[5] Jonathan Bellarby. *Well Completion Design*, volume 56. Elsevier, 2009.

[6] Deli Gao, Lianzhong Sun, and Jihong Lian. Prediction of casing wear in extended-reach drilling. *Petroleum Science*, 7(4):494–501, 2010.

[7] JS Song, Jerry Bowen, Frank Klementich, et al. The internal pressure capacity of crescent-shaped wear casing. In *SPE/IADC Drilling Conference*. Society of Petroleum Engineers, 1992.

[8] Jerry P White, Rapier Dawson, et al. Casing wear: laboratory measurements and field predictions. *SPE Drilling Engineering*, 2(01):56–62, 1987.

[9] Jiang Wu, Mei Zhang, et al. Casing burst strength after casing wear. In *SPE Production Operations Symposium*. Society of Petroleum Engineers, 2005.

[10] JE Fontenot and JW McEver. The experimental measurement of casing wear due to tripping—part 1: Drill pipe wear. *Journal of Engineering for industry*, 97(2):445–455, 1975.

[11] S Sangesland, M Rausand, H Torbergsen, H Haga, B Aadnøy, J Sæby, S Johnsen, and M Lundeteigen. An introduction to well integrity. *Rev 0, December*, 2012.

[12] Arthur Peter Boresi, Richard Joseph Schmidt, and Omar M Sidebottom. *Advanced mechanics of materials*, volume 6. Wiley New York, 1993.

[13] N.E Dowling. Mechanical behaviour of materials: Engineering methods for deformation, fracture, and fatigue. 4th, 2012.

[14] Benjamin Cole Craft. *Well design: drilling and production*. Prentice Hall, 1962.

[15] Jan A. Aasen and Bernt S. Aadnoy. Three-dimensional well tubular design improves margins in critical wells, 2007. ISSN 0920-4105.

[16] David Roylance. Introduction to fracture mechanics. *Massachusetts Institute of Technology, Cambridge*, 2001.

[17] Anders Ekberg. Fracture mechanics. *Department of Solid Mechanics, Chalmers Univesity of Technology*, 1997.

[18] Daryl L. Logan. *A First Course in the Finite Element Method*. Cengage Learning, 5 edition, 2011. ISBN 0495668257,9780495668251.

[19] C. A Felippa. Chapter 6 - finite element modeling: Introduction., 2014 A. http://www.colorado.edu/engineering/CAS/courses.d/IFEM.d/IFEM.Ch06.d/IFEM.Ch06.pdf.

[20] Gui-Rong Liu and Siu Sin Quek. The finite element method: a practical course, 2013.

[21] Tina Puntervold, Skule Strand, Raed Ellouz, Tor Austad, et al. Why is it possible to produce oil from the ekofisk field for another 40 years? In *International Petroleum Technology Conference*. International Petroleum Technology Conference, 2014.

A Appendix: Effect of Seed Size

The simulation of both the crescent shaped wear and the wedge shaped wear showed a more or less "smooth curve", hence, the curve representing the simulated results for a rectangular shaped scar were at first thought be similar. However, since this was not the case, further investigations were performed. To check if the meshing could cause the unexpected shaped of the curve and the drastically decreased burst strength from 0% wear to 5%, the seed size was reduced from 0.1 to 0.05. The results is presented in figure A.1.

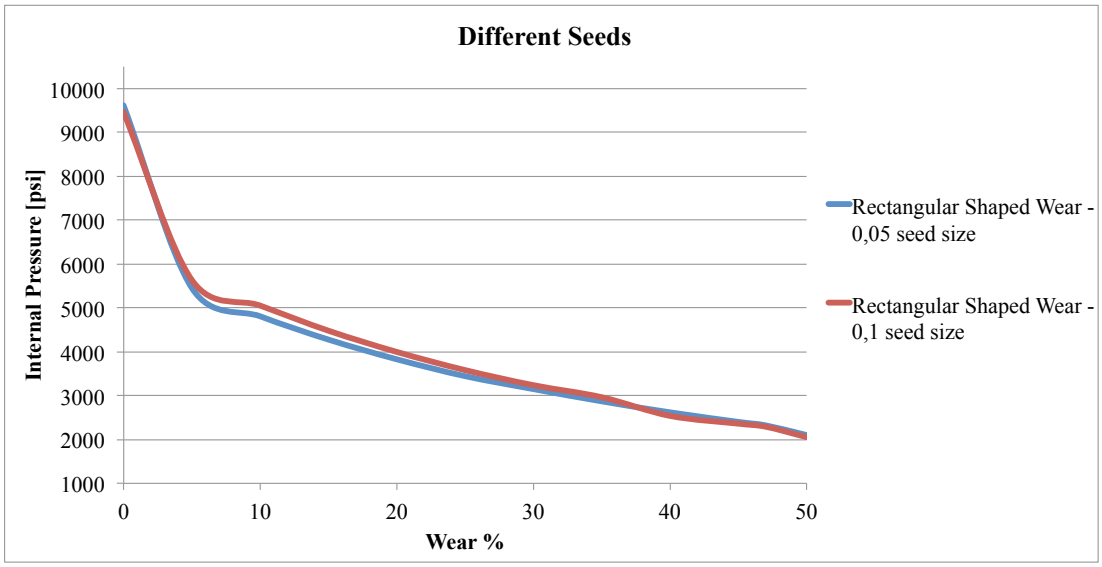

Figure A.1: Comparison of the rectangular wear shape for different seeds

According to the simulation, reducing the seed size to 0.05 does not eliminate the significant reduction in burst pressure that is observed for the case with the seed size of 0.1. The curves follows the same trend both seed sizes. Thus, in this specific scenario, it seems that the rectangular wear shape, even for small wear depths, has a significant impact on the material strength of the tubing.

B Appendix: Effect Of Wear Width

During this thesis several additional simulations were performed to study the effect of a wedge shaped wear. For a crescent shaped scar the wear width becomes wider as the indentation depth increases. The following section presents results from simulations where a wedge shaped wear follows the same width variations as a crescent scar when the wear depth increases.

In figure B.1 a crescent shaped wear is compared to the wedge shaped wear with increased width. A wedge shaped wear of 1.5 inches and 1.75 inches is also presented. According to the simulations the width of the wedge shaped wear seems to have little effect on the burst pressure resistance of the tubing. A similar burst pressure resistance is observed for the wedge shaped wear of 1 inch, 1,5 inch and 1,75 inch, and for the wedge shaped wear with increased width.

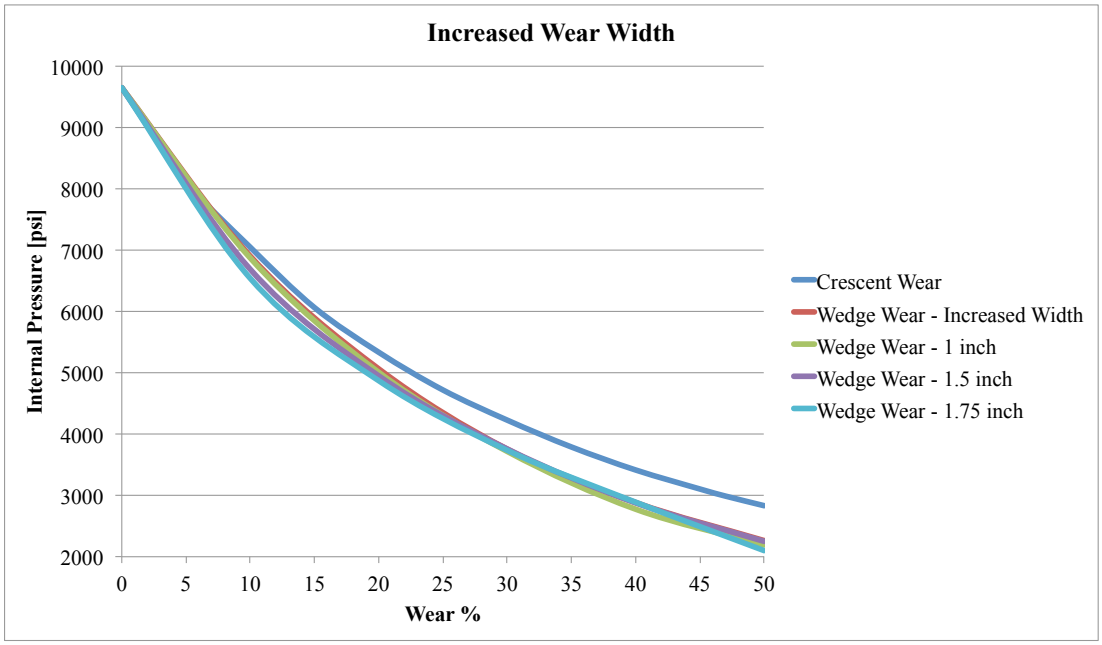

Figure B.1: Different Local Wear Width